ASPECTS IN BREAK-UP REACTIONS

Ph.D. THESIS

by

NEELAM

DEPARTMENT OF PHYSICS
INDIAN INSTITUTE OF TECHNOLOGY ROORKEE
ROORKEE – 247667 (INDIA)
JUNE, 2017

ASPECTS IN BREAK-UP REACTIONS

A THESIS

*Submitted in partial fulfilment of the
requirements for the award of the degree*

of

DOCTOR OF PHILOSOPHY

in

PHYSICS

by

NEELAM

**DEPARTMENT OF PHYSICS
INDIAN INSTITUTE OF TECHNOLOGY ROORKEE
ROORKEE–247667 (INDIA)
JUNE, 2017**

INDIAN INSTITUTE OF TECHNOLOGY ROORKEE
ROORKEE

CANDIDATE'S DECLARATION

I hereby certify that the work which is being presented in this thesis entitled, **"ASPECTS IN BREAK-UP REACTIONS"** in partial fulfilment of the requirements for the award of the Degree of Doctor of Philosophy and submitted in the Department of Physics of the Indian Institute of Technology Roorkee, Roorkee is an authentic record of my own work carried out during a period from July, 2010 to June, 2017 under the supervision of Dr. Rajdeep Chatterjee, Associate Professor, Department of Physics, Indian Institute of Technology Roorkee, Roorkee.

The matter presented in this thesis has not been submitted by me for the award of any other degree of this or any other Institute.

(NEELAM)

This is to certify that the above statement made by the candidate is correct to the best of my knowledge.

(Rajdeep Chatterjee)
Supervisor

Date _____

ABSTRACT

Break-up reactions offer many opportunities to study the structure and reactions of exotic nuclei. In this thesis we use the theoretical formalism of elastic Coulomb break-up reactions to study medium mass exotic nuclei and also applications in nuclear astrophysics. This work is divided into two parts consisting of five chapters and two appendices. The first three chapters, which form the part I, contain the introduction, a brief theoretical formalism of break-up reactions leading to the distorted wave Born approximation and applications of our theory to ^{37}Mg. The last two chapters contain the application of our theory as an indirect method to calculate radiative capture reaction cross-sections in nuclear astrophysics and the summary and future outlook of our work. Along with two appendices this forms the part II of the thesis.

In chapter 1 we give an introduction to the field of exotic nuclei elaborating on their general characteristics and also the fact the field has moved to the medium mass region of the nuclear chart, where nuclei can also be deformed. We also briefly discuss the experimental facilities where experiments with exotic nuclei are being performed. The role of radiative capture reactions in nuclear astrophysics is also discussed here.

In chapter 2 we describe the basic theoretical formalism of break-up reactions

leading to the post and prior forms of the transition matrix. We then focus on the distorted wave Born approximation for the elastic break-up of a two-body projectile in the field of a target. Specializing to pure Coulomb break-up and more specifically to the case where we have an uncharged fragment in the final channel, we show that the transition matrix can be split into two parts - a dynamics part which can be evaluated analytically and a structure part where the ground state wavefunction of the projectile is an input. This theory is further developed in the next chapter when the break-up of a deformed projectile is studied in a semi-analytic way.

In chapter 3 we study the elastic Coulomb break-up of ^{37}Mg on a Pb target at 244 MeV/nucleon beam energy. By calculating several reaction observables like the total one-neutron removal cross-section, the neutron-core relative energy spectrum, the parallel momentum distribution of the core fragment, the valence neutron angular, and energy-angular distributions, we try to set limits on the ground state spin-parity and one neutron separation energy of ^{37}Mg.

In chapter 4 we study the ^{15}N$(n, \gamma)^{16}$N radiative capture cross-section and its subsequent reaction rate by an indirect method and in that process investigate the effects of spectroscopic factors of different levels of ^{16}N to the cross-section. We calculate the Coulomb break-up of ^{16}N on Pb at 100 MeV/nucleon and relate this to the photodisintegration cross-section of ^{16}N$(\gamma, n)^{15}$N. Subsequently invoking the principle of detailed balance, the ^{15}N$(n, \gamma)^{16}$N capture cross-section is calculated. The calculated reaction rate is also compared with various other charged particle rates and consequences of the same as a function of temperature in stellar environments are discussed.

The summary and future directions of our work are presented in chapter 5. Some mathematical details of the formalism and of the approximations are also given in various appendices.

ACKNOWLEDGMENTS

With completion of this thesis, I want to express my sincere gratitude to my supervisor *Prof. Rajdeep Chatterjee* for his guidance, support, encouragement and suggestions. During this period there were very difficult situations. I sincerely appreciate your help during the time.

I thank the faculty of the Department of Physics *Prof. K. L. Yadav, Prof. A. K. Jain, Prof. P. Arumugam, Prof. G. D. Verma, Prof. Veer Singh, Prof. R. Balasubramanian* (Department of Computer Science and Engineering, I.I.T. Roorkee) for their valuable questions/comments and remarks on earlier presentations of this research work. Further, I extend my sincere thanks to all the faculty members of the Department of Physics, I.I.T. Roorkee.

I am also grateful to *Prof. R. Shyam* for important discussions during conferences and workshop-schools.

I feel great pleasure in mentioning friends *Dr. Navjot Kaur, Dr. Manisha Dharwan, Dr.Bhoomika Maheshwari, Mahima Khokhar, Dr. Monika Patial, Dr. Monika Dhariwal, Dr. Swati Verma, Dr. Meera Rawat*, and all other research scholars of physics department for their company and for the quality time that I spent with them. A special thanks to my senior *Dr. Shubhchintak*, for his useful disscussions and invaluable research guidance. Thanks to my research group *Gagandeep, Manju*

Yadav, and Munna for their help.

Thanks to *Simranjeet Lall, Vandana Rani, Seema Gautam* for being my best friends. I can't forget the love and care you people have for me and every chapter of my life completes with you people.

Thanks *Maa* for everything you did for me. I owe my whole life to you. Thanks to my brother *Praveen* and my sister *Rinki* for being my support through out the life. You people are reason for me to live.
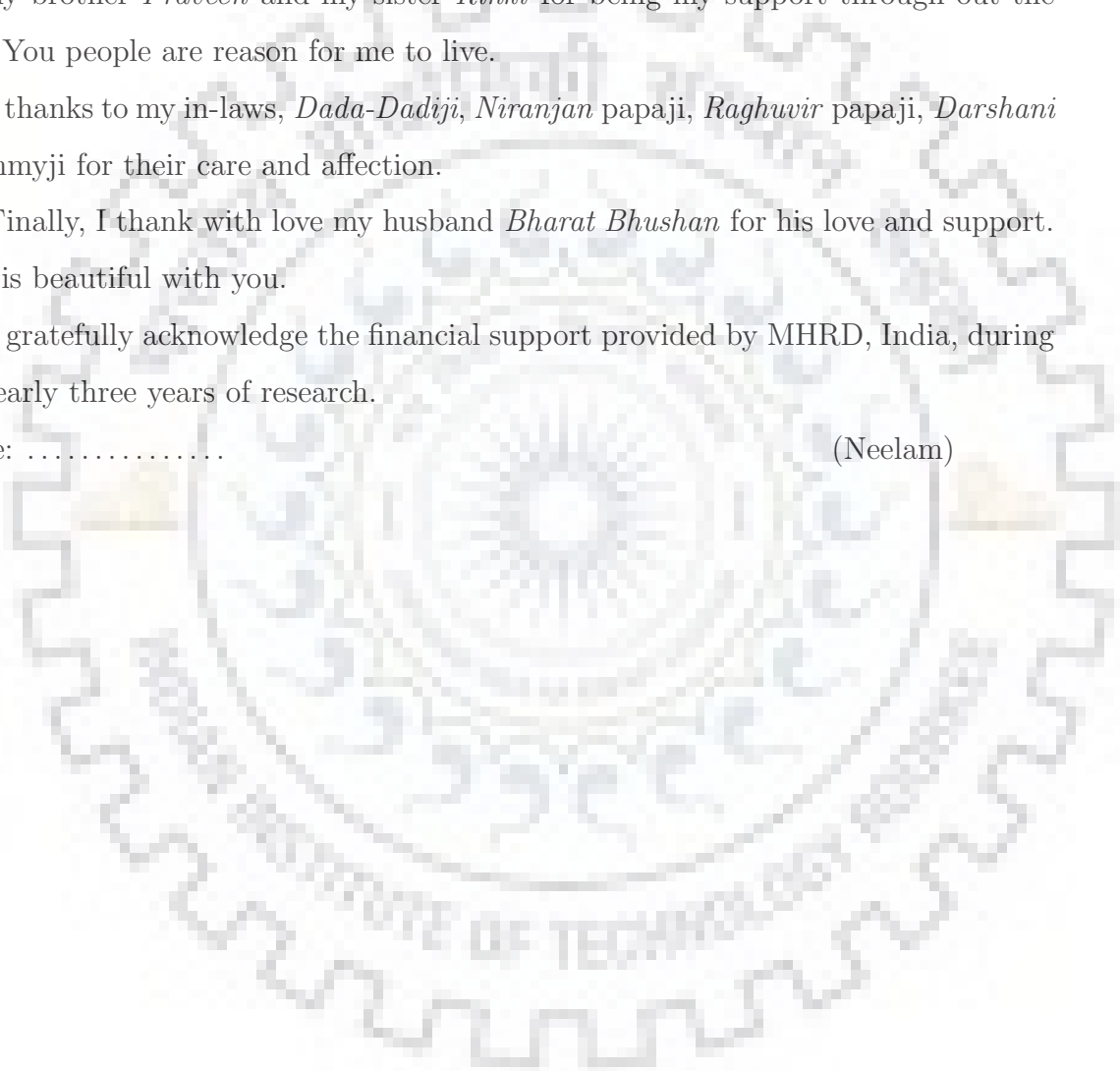
I thanks to my in-laws, *Dada-Dadiji, Niranjan* papaji, *Raghuvir* papaji, *Darshani* mummyji for their care and affection.

Finally, I thank with love my husband *Bharat Bhushan* for his love and support. Life is beautiful with you.

Date: ....   (Neelam)

Dedicated to My Parents

Smt. Maya Devi and Late Sh. Balia Ram

List of Publications

Publications in Referred Journals

1. *Structure effects in the $^{15}N(n,\gamma)^{16}N$ radiative capture reaction from the Coulomb dissociation of ^{16}N*, **Neelam**, Shubhchintak and R. Chatterjee, **Phys. Rev. C 92**, 044615 (2015).

2. *Coulomb breakup of ^{37}Mg and its ground state structure*, Shubhchintak, **Neelam**, R. Chatterjee, R. Shyam, and K Tsushima, **Nucl. Phys. A 939**, 101 (2015).

Under Preparation

1. *Capture cross-section and rate of $^{11}B(n,\gamma)^{12}B$ from Coulomb dissociation calculations*, **Neelam**, Shubhchintak and R. Chatterjee (Under Preparation).

Papers in Conferences/Symposium:

1. *Photodisintegration cross-section of ^{9}Be*, **Neelam**, Shubhchintak Proceedings of DAE Symposium on Nuclear Physics, Vol. 57, pg. 628 (2012).

2. *Semi-Analytical approach to Coulomb breakup reactions*, Shubhchintak, **Neelam** and R. Chatterjee, Proceedings of DAE Symposium on Nuclear Physics, Vol. 56, pg. 682 (2011).

CONTENTS

LIST OF FIGURES

LIST OF TABLES

PART - I

CHAPTER 1

INTRODUCTION

1.1   The prelude

Mankind always has quest for origin of matter that can be answered with nuclear physics as nucleus is the heart of matter [1]. Only few nuclei (near about 300) are stable otherwise most of them are unstable. The stable nuclei nuclei lies on the valley of stability line and unstable nuclei are spread on both side of stability line as shown in Fig. 1.1 (also called as Segré chart after the name of the physicist Emilio Segré), on the x-axis the neutron number (N) and along y-axis the proton number(Z) is plotted. Farther we go away from stability valley, nuclei became more unstable until we reach at a point where nuclei become so unstable that leads particle emission to gain stability.

The black square represents stable nuclei. Above of stability valley are unstable nuclei which are deficient in neutrons (shown with pink color) and this region is limited by the proton drip line (dashed red) which is reached when binding energy for last proton, B_p become zero. Below the valley of stability are those unstable nuclei which has excess of neutrons (shown with blue color) and this region is limited by
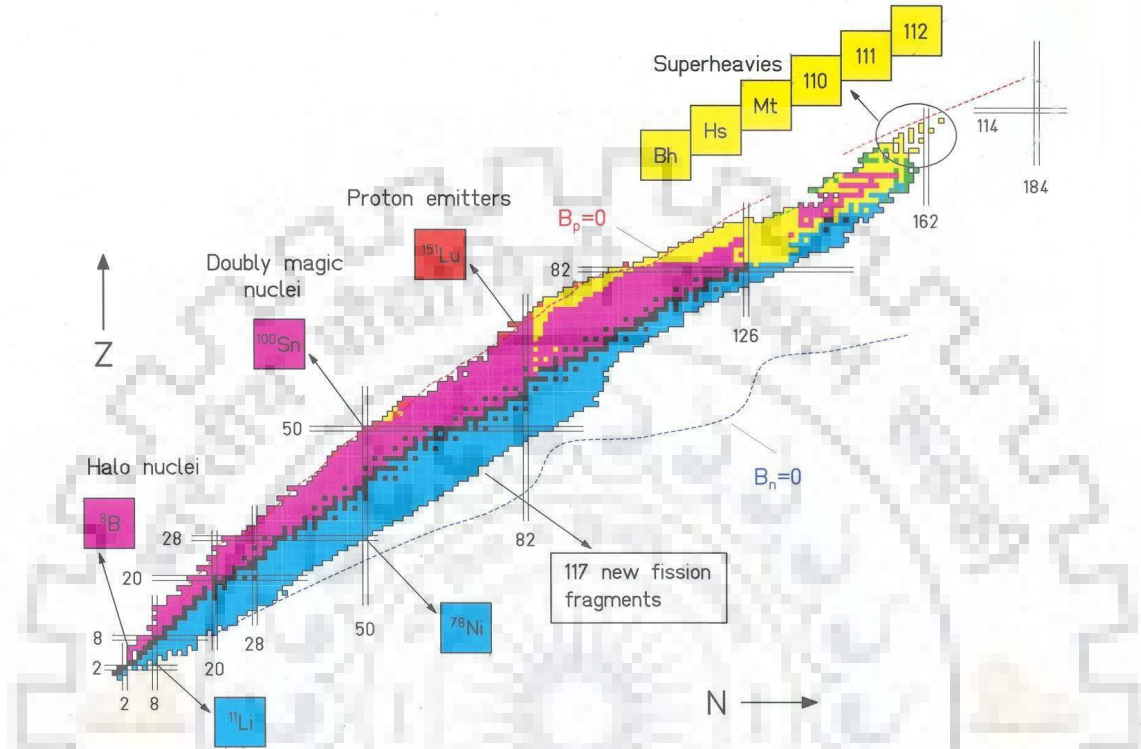
Figure 1.1: The Segré chart

the neutron drip line (dashed blue) which is reached when valence neutron binding energy, B_n become zero. In Shell model, the closed shells are given by N(or Z) $2, 8, 20, 28, 50, 82, 126$ which are called magic numbers as they give extra stability than nearby nuclei. These magic number are shown by horizontal and vertical bars in Fig. 1.1. To understand the entire regime in N-Z plane, we require information of nuclei on the valley of stability and away from stability. It is estimated that around 5000 to 7000 bound nuclei should exist, out of which only 2000 nuclei are observed. Lots of theoretical and experimental work have been done on nuclei on valley of stability but region away from stability valley which is made up of short-lived, radioactive and loosely bound nuclei (called exotic nuclei) [2-15] the knowledge is still meagre. This is therefore a vastly unexplored area.

From theoretical point of view, stable nuclei are well studied and are mostly well explained but for exotic nuclei while constructing theoretical models we must emphasize on few interesting properties of exotic nuclei.

1.) Exotic nuclei are spatially extended system. Halo structure exists.

2.) Exotic nuclei can be deformed.

3.) Exotic nuclei exhibit new types of shell evolution. New magic numbers can occur.

4.) Exotic nuclei exhibit clusterization.

5.) In exotic nuclei continuum states are very close to ground state so reaction mechanism will be affected.

6.) Exotic nuclei, in principle, are open quantum systems.

On the experimental side, the problem with exotic nuclei is that because of short-lived and unstable nature, there is very little time between the production and experiment and so they can't be used as target. In last two decades, with advanced Radioactive Ion Beams (RIB) facilities, we are able to produce these exotic nuclei in laboratory. In the next section we will discuss various experimental facilities to produce beam of exotic nuclei to be studied.

1.2 Experimental facilities

With the advances made in the technology of producing nuclear species with relatively large neutron (N) to proton (Z) number ratios, it is now possible to extensively study nuclei near the neutron-drip line with $Z > 8$. During the last three decades measurements performed on mass, radius and spectroscopy of such nuclei have shown that they have structures that are at variance with those of their "near the line of stability" counterparts. With the advent of new generation of radioactive ion beam facilities, it has now become possible not only to produce medium mass neutron rich nuclei in the vicinity of the magic numbers but also employ them

as projectiles to initiate reactions (e.g., break-up) on nuclear targets [16, 17]. This provides excellent opportunity to perform quantitative study of the single-particle structure and the shell evolution in this region. To study exotic nuclei, firstly we have to produce the nuclei of interest and then separate it to study. Fission [18], target spallation [19], projectile fragmentation [20], nucleon transfer [21, 22] and fusion evaporation [23] are various techniques that are used to produce exotic nuclei. To separate produced nuclei, techniques that are used can be divided into two categories, isotope separation on-line (ISOL) and in flight separation (fragmentation)(IFS). The schematic diagram is shown in Fig. 1.2 and is taken from [24]
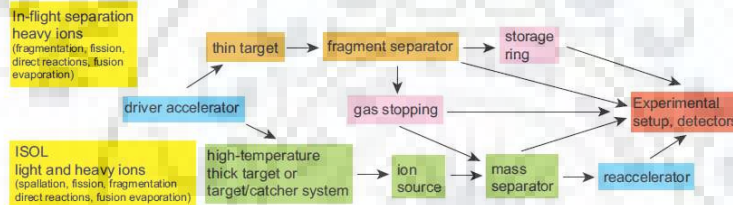
Figure 1.2: ISOL and IFS facility shown diagramatically.

In ISOL , a beam of particles which is consist of protons, neutrons , light or heavy ions are projected on a thick target as a result radioactive nuclei is produced. It is then passed through a ion source which ionize it which makes process of extraction and acceleration possible. These ion then can be used for experiment at low energy or can be further accelerated to induce nuclear reactions. Advantage of this technique is that beam of particles has high energy and high quality. The ISOL techniques was first used at CERN under the guidance of Prof. V. F. Weisskopf [25]. In 1987 Radioactive Ion Beam Project, LISOL started in Louvain-la-Neuve, Belgium [26] and ^{13}N beam was accelerated. Another ISOL techniques based facilities are Holified Radioactive Ion Beam Facility (FRIB) at Oak Ridge [27], SPIRAL project at GANIL in France [28], REX-ISOLDE at CERN [29], ISAC at TRIUMF in Canada [30], EXCYT at the INFN - LNS laboratory at Catania [31], TRIAC facility at Tokai, Japan [32].

Intermediate-generation based ISOL facilities are present in HIE-ISOLDE at CERN, [33, 34], SPES in Legnaro, Italy [35], SPIRAL2 at GANIL, Caen, France and upcoming European ISOL facility, EURISOL

In in-flight separation (IFS), an energetic beam of particles is projected on thin target and as a result radioactive nuclei are produced. The nuclei of interest is separated using a fragment separator and sent for experimental use. This technique is useful in producing short-lived beam of nuclei with high energy. This facility was used for the first time at Lawrence Berkeley Labaratory [36]. Then it was used in LISE spectrometer GANIL [37] and after that this technique was widely used in many facilities such as A1200 separator at the NSCL in USA [38], in RIPS separator at RIKEN in Japan [39], the FRS device at GSI in Germany [40], the COMBAS separator at Dubna [41], in Russia and LISE-3 at Ganil [42], A1900 separator at NSCL [43], Big- RIPS in Japan [44] and Super FRS in Germany [45].

1.3   Coulomb dissociation method

In Coulomb dissociation method [46], when a projectile, a is projected towards heavy target t, experiencing Coulomb field of the target the projectile breaks-up in to two substructures b and c. (see Fig. 1.3).

$$a + t \rightarrow b + c + t, \tag{1.1}$$

b is the core nuclei and c is the valence nucleon which can be charged or uncharged.

The electromagnetic field of target is replaced by a beam of equivalent virtual photons. where virtual photon number can be calculated using proper kinematics [46]. The idea of equivalent photon number was given by Fermi in his classic paper [47, 48]. Thus Coulomb break-up becomes equivalent to photodisintegration. The Coulomb break-up process, is then related to the photodisintegration reaction. Further using principle of detailed balance radiative capture process can be stud-
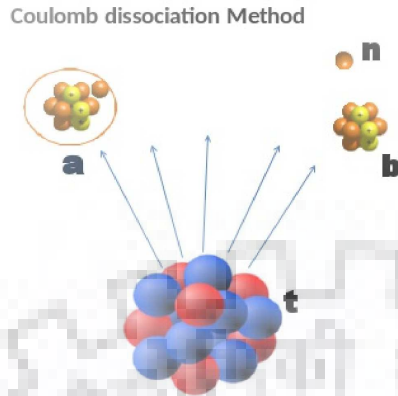
Figure 1.3: Coulomb break-up of projectile, a in the field of heavy target, t

ied [46]. The radiative capture reactions plays vital role both in determining nuclear structure and nucleosynthesis in nuclear astrophysics. Thus capture reactions can be studied via Coulomb break-up reactions.

Recently [49], the post form finite range distorted wave Born approximation (FRDWBA) theory of Coulomb break-up reactions has been extended to include the deformation of the projectile by using a deformed Woods-Saxon potential to describe the valence neutron-core relative motion. Hence, this provides a microscopic theoretical tool to study the Coulomb break-up of neutron-drip line nuclei lying in island of inversion in the vicinity of $N = 20 - 28$ and to investigate the correlation between halo formation and the shell evolution and deformation. In the first application of this theory, the Coulomb break-up of ^{31}Ne on a Pb target at the beam energy of 234 MeV/nucleon was investigated [49]. Comparison of calculated and the measured one-neutron removal cross-section (of Refs. [16, 50]) suggested that the ground state of ^{31}Ne is most likely to have a ^{30}Ne $\otimes 2p_{3/2}\nu$ configuration. The value of the one-neutron separation energy S_n is found to be correlated to the quadrupole deformation parameter (β_2). For β_2 between $0.0 - 0.5$, S_n varies between $0.24 - 0.58$ MeV. The calculated full width at half maximum (FWHM) of the parallel momentum distribution of ^{30}Ne fragment is closer to that of the core fragment seen

in the break-up reaction of the established halo nucleus ^{11}Be. This strongly suggests that the ground state of ^{31}Ne has a one-neutron halo structure in the $2p_{3/2}$ state. The theory can be used for the study of other loosely bound nuclei in the region of neutron drip line. One such candidate is ^{37}Mg. Its is said to be weakly bound deformed nuclei but its spin-parity of ground state is still uncertain.

1.3.1 Shell Evolution in exotic nuclei

The notion of "magic" numbers is one of the most fundamental concepts in nuclear structure physics [51,52]. If large gaps occur between groups of single-particle orbits that are completely filled with nucleons (neutrons or protons), then these nucleon numbers are called "magic". The seven most established magic numbers are 2, 8, 20, 28, 50, 82, and 126. However, in several nuclei near the neutron-drip line, modifications to this shell structure have been observed [53,54]. In these cases the magic numbers evolve as a function of the neutron number - old magic numbers may disappear while new ones emerge and conventional shell gaps may break down. For example, rapid changes in nuclear structure and vanishing of the $N = 8$, and 20 shell gaps have been seen in neutron rich nuclei ^{12}Be [55], and ^{32}Mg [56] and ^{30,32}Ne [57], respectively. For neutron drip line nuclei N=16 is new magic number as seen in case of ^{24}O [58–62]. Examples of $N = 28$ shell quenching have been observed in ^{36,38}Mg [63] and ^{42}Si [64]. It is suggested in Ref. [65] that island of inversion near $N = 20, 28$ comes about because of the fact that the $\nu(sd)^{-2}(fp)^2$ intruder configurations (here ν represents a relative neutron state), in which two neutrons from the sd shell are excited to the fp shell, become so low in energy that they form the ground states for $Z = 10 - 12$ and $N = 20 - 22$ nuclei. This suggestion was confirmed subsequently by mass measurements of the neutron rich isotopes of Ne, Na and Mg nuclei [66]. Recently, this behavior has been shown to be a general phenomena that should occur for most standard shell closures far from the line of stability, and the mechanism behind this is found to be related to the importance of the nucleon-nucleon tensor interaction [67]. It is obvious that due to the intruder

states, the single particle structure of the ground states of nuclei lying within island of inversion will not be the same as that emerging from the usual filling of the shell model states.

1.3.2 Exotic nuclei could be deformed

The mixing of neutron n-particle-n-hole $(np-nh)$ intruder configurations of $\nu(sd)^{-n}(fp)^n$ character to the ground state, causes large deformation to nuclei in island of inversion near $N = 20, 28$, which is confirmed by the measured low excitation energies and $B(E2)$ values of the first excited states (see, eg., Refs. [56, 57, 68–71]). It has been emphasized [65,72-74] that the deformation may also account for the enhanced binding energies manifested in some of the known nuclei in this region. The collective properties of neutron rich nuclei near $N = 20$ region are rather well described by Monte-Carlo shell model calculations that allow for unrestricted mixing of neutron particle-hole configurations across the shell gap [75, 76]. In Ref. [77, 78], nuclei in the neighborhood of neutron-drip line have been systematically investigated in a model where one-particle motion is described within spherical as well as deformed potentials. It has been concluded in this work that nuclei in the region of $N = 20 - 28$ are most likely to be deformed.

The evidence of a deformed nuclei is measurement of the root mean square radius (RMS). For a deformed nuclei root mean square radius is larger than $R = r_0 A^{1/3}$, where r_0 is radius parameter and A is mass number of nuclei. Total reaction cross-section (σ_R) depends on RMS radii of the projectile and the target nuclei. So for a deformed nuclei the value of interaction cross-sections (which are almost the same as the σ_R) is larger than neighbouring spherical nuclei.

1.3.3 Exotic nuclei and halo structure

Discovery of halo structure in some of the drip line nuclei is another important progress made in the studies of nuclei with large N to Z ratio near the limits of
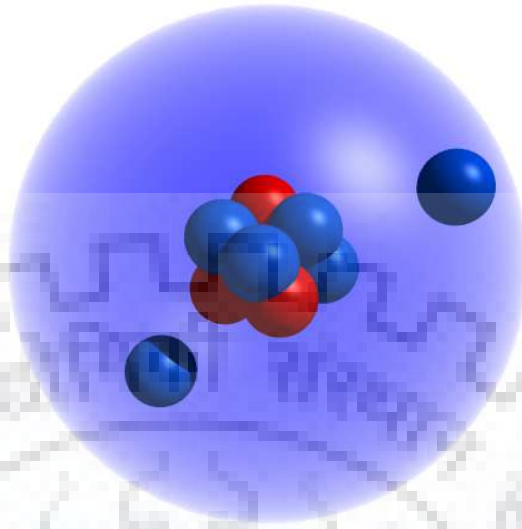
Figure 1.4: Halo structure in ^{11}Li.

nuclear stability [8, 79–85]. As one approaches the neutron-drip line nuclei experience weakening of the neutron separation energy, which leads to some interesting effects. The sudden rise of interaction cross-sections with increasing N in some of these nuclei can be attributed to the extended density distribution(s) of the valence neutron(s). This decoupling of the valence neutron(s) from the tightly bound core and the extension of the corresponding wavefunction to much larger radii have been referred to as neutron halo. This phenomena has been seen earlier in lighter nuclei like ^{11}Li [86], ^{11}Be [87], ^{19}C [79].

In recent years, there has been considerable interest in finding out if halo configurations also exist in nuclei lying near the neutron-drip line in the vicinity of island of inversion [88, 89]. ^{31}Ne with $Z = 10$ and $N = 21$, is a promising candidate to have a one-neutron halo configuration because the one-neutron separation energy of this nucleus is quite small (0.29 ± 1.64 MeV [90], or 0.06 ± 0.41 MeV [91]). Indeed, such a structure has been suggested for this isotope by Coulomb break-up studies [16]. This has been further supported by measurements [92] of the interaction cross-sections for Ne isotopes incident on a ^{12}C target at the beam energy of 240 MeV/nucleon,

where it was found that for ^{31}Ne the interaction cross-section was much larger than that of any other Ne isotope. Recently, measurements of σ_R for $^{24-38}$Mg isotopes on ^{12}C target at the beam energy of 240 MeV/nucleon have been reported in Ref. [93]. From a similar reasoning, it was suggested in this study that ^{37}Mg ($Z = 12, N = 25$) that lies in $N = 20 - 28$ island of inversion, is also a candidate for having a one-neutron halo structure. This was reinforced by measurements of Coulomb break-up of ^{37}Mg on C and Pb targets at the beam energy of 244 MeV/nucleon in Ref. [17].

The observation of the halo phenomena in the heavier nuclei lying in island of inversion, signals major changes in the shell evolution in these nuclei as compared to that seen in the spherical ones. One of the conditions for the halo formation is that the loosely bound neutron in the nucleus occupies a low orbital angular momentum state ($\ell = 0$ or 1) in order to reduce the centrifugal barrier effects that prevent it from spreading out [88]. In fact, in well established cases of light one-neutron halo nuclei like ^{11}Be and ^{19}C, the ground states have predominant s-wave neutron plus core configurations [81, 94–97]. According to the conventional shell model evolution, one expects to see the domination of the $1f_{7/2}$ orbit in nuclei in the vicinity of $N = 20 - 28$. This would not favor the halo formation because a larger centrifugal barrier would prevent the $l = 3$ neutrons to extend too far out in the space. Therefore, a significant contribution from the s- or p-wave orbits has to be there in the ground state structure of these nuclei to minimize the centrifugal barrier. Thus, the existence of halo structure would imply a significant modification of the shell structure that involves considerable mixing of the intruder states like $2p_{3/2}$ or $2s_{1/2}$ into the ground states of these nuclei, which also leads to the appreciable deformation of these states. Therefore, the halo formation in heavier nuclei in island of inversion region has strong correlation with the shell evolution and the presence of deformation.

1.4   Role of neutron radiative capture reaction in nuclear astrophysics

Neutron radiative capture reactions plays crucial role in element production in primordial, interstellar and stellar nucleosynthesis [98–102]. In primordial synthesis, light nuclei such as Hydrogen, Helium and some traces of Lithium are produced by Big Bang. Interstellar nucleosynthesis leads to formation of elements like Lithium, Beryllium and Boron whereas stellar and explosive nucleosynthesis produces elements from Carbon to Uranium. Thats how elements formations takes place in various astrophysical sites. With Sun being the nearest star, it's easy to observe solar abundances. Observing solar abundances in regions $A = 80-90, 120-130, 180-210$, we finds abundances peaks are placed at neutron shell closure i.e. at $N = 50, 82, 126$. Further study reveals that in these regions the element synthesis takes place by two different processes, $s-$ process [103] and $r-$ process [104] followed by $\beta-$decay. The s(slow)-process refers to the case when neutron capture reaction rate is less than β-decay rate which occurs in neutron deficient environment (i.e near bottom of valley of stability). In this process competition between neutron capture reactions leads to the branching in reaction paths [105] and r(rapid)-process means when neutron capture rate dominates over β-decay rate [106]. It takes place in neutron drip line region as high neutron density is required. Neutron capture reaction leads to formation of new element until it is counter balanced by hot photon bath and reach equilibrium at waiting point where $(n, \gamma) = (\gamma, n)$. Astrophysical sites for s- process and r-process is still largely unknown [107]. Red Giant stars can be probable site for $s-$process and supernovae type II for $r-process$.

The problem with direct measurement of the radiative capture is that it has to be measured at low stellar energy, resulting in low cross-section and also in the presence of intense background, complications are further added with involvement of radioactive beam. The other way to study radiative capture is reverse reactions

i.e. to study $(\gamma, n)^1$ instead of (n, γ) reactions. The break-up reaction cross-section can be correlated with the radiative capture cross-section using principle of detailed balance. In Coulomb break-up, virtual photon of Coulomb field provides the γ flux. The advantage of this indirect radiative capture measurement is that one can study break-up cross-section at higher energy and then can relate it to low energy the radiative capture cross-section. With advancement in RIB facility it is now possible to perform experiment on reactions of astrophysical. interest. For example Laboratory for Underground Nuclear physics (LUNA)accelerator in Italy has done measurement on critical reaction in hydrogen burning. At HRIBF and at TRIUMF in Canada several reactions in hot CNO cycle have been measured using inverse kinematics with short lived radioactive beam on H and He gas target. With high intensity beam faciliies such as RIPS at RIKEN, SPIRAL at GANIL, FAIR at GSI, HIE-ISOLDE at CERN, FRIB at MSU, we can study many reactions of stellar nucleosynthesis .

1.5 Scope of the thesis

With this brief discussion on studies of nuclei near drip line and the importance of neutron radiative capture reactions in astrophysics, we now focus on the scope of the thesis. The thesis is divided into two parts.

In **chapter 2** the transition matrix for a elastic break-up reaction and the post form finite range distorted wave Born approximation formalism for Coulomb break-up of a projectile into two fragments are explained. In **chapter 3** we examine the structure of a deformed exotic medium mass nucleus, ^{37}Mg, using the Coulomb dissociation method and try to set limits on the ground state spin-parity and the one neutron separation energy of ^{37}Mg. This constitutes the first part of the thesis.

In **chapter 4**, we study the ^{15}N$(n, \gamma)^{16}$N capture cross-section using the Coulomb dissociation of ^{16}N as an indirect approach in nuclear astrophysics and subsequently

---

[1]Radiative capture involves proton, α and neutron capture. The work in this thesis is based on neutron capture. So we will emphasize on neutron capture.

also calculate the reaction rate of $^{15}\text{N}(n,\gamma)^{16}\text{N}$. We also investigate the effects of spectroscopic factors of different levels of ^{16}N to the cross-section. Reaction rates are also compared with other charged particle reactions. In **chapter 5**, summary and future outlook of the thesis are presented. This, along with two appendices, constitutes the second part of the thesis.

BIBLIOGRAPHY

[1] José J, and Iliadis C., Nuclear astrophysics: the unfinished quest for the origin of the elements, Rep. Prog. Phys. **74**, 096901 (2011).

[2] Tanihata I., Savajols H., and Kanungo R., Recent experimental progress in nuclear halo structure studies, Prog. Part. Nucl. Phys. **68**, 215 (2013).

[3] Hagino K., Tanihata I., and Sagawa H., Exotic nuclei far from the stability line, arXiv:1208.1583 [nucl-th], (2012).

[4] Hansen P. G. and Sherill B. M., Reactions and single-particle structure of nuclei near the drip lines, Nucl. Phys. A **693**, 133 (2001).

[5] Jonson B., Halo states in nuclei, Nucl. Phys. A **631**, 376 (1998).

[6] Riisager K., Nuclear halo states, Rev. Mod. Phys. **66**, 1105 (1994).

[7] Zhukov M. V., Danilin B. V., Federov D. V., Bang J. M., Thompson I. J., and Vaagen J. S., Bound state properties of Borromean halo nuclei: ^{6}He and ^{11}Li, Phys. Rep. **231**, 151 (1993).

[8] Bertulani C. A., Canto L. F., and Hussain M. S., The structure and reactions of neutron-rich nuclei, Phys. Rep. **226**, 281 (1993).

15

[9] Hansen P. G., Nuclear structure at the drip lines, Nucl. Phys. A **553**, 89 (1993).

[10] Mueller A. C. and Sherill B. M., Nucli at the Limits of Particle Stability, Ann. Rev. Nucl. Part. Sci. **43**, 529 (1993).

[11] Santra S., Kailas S., Ramachandran K., Parkar V. V., Roy B. J., Shukla P., Reaction mechanisms involving weakly bound ^{6}Li and ^{209}Bi around Coulomb barrier, Phys. Rev. C **83**, 034616 (2011).

[12] Stefan I. *et al.*, Probing nuclear forces beyond the drip-line using the mirror nuclei ^{16}N and ^{16}F, Phys. Rev. C **90**, 014307 (2014).

[13] Bhattacharya M., Gangopadhyay G. and Roy S., Helium nuclei around the neutron drip line, Phys. Rev. C **85**, 034312 (2012).

[14] Signorini C., Andrighetto A., Guo J.Y., Vitturi A., **et al.**, The potential of the loosely bound Be-9 from Bi-209 elastic scattering: unusual behaviour at near threshold energy, Nucl. Phys. A **701**, 23 (2002).

[15] Mazzocco M., Scopel P., Signorini C., Vitturi A., *et al.*, Excitation of Li-6 above the breakup threshold in the Li-6+Pb-208 system around the Coulomb barrier, Eur. Phys. J A **18**, 583 (2003).

[16] Nakamura T., *et al.*, Halo Structure of the Island of Inversion Nucleus ^{31}Ne, Phys. Rev. Lett. **103**, 262501 (2009).

[17] Kobayashi N. *et al.*, Observation of a p-Wave One-Neutron Halo Configuration in Mg^{37}, Phys. Rev. Lett. **112**, 242501 (2014).

[18] Alvarez-Pol H. *et al.*, Production of new neutron-rich isotopes of heavy elements in fragmentation reactions of ^{238}U projectiles at 1 **A** GeV, Phys. Rev. C **82**, 041602 (2010).

[19] Blumenfeld Y., Nilsson T., and Duppen P. V., Facilities and method for radioactive ion beam production, Phys. Scr.T **152**, 014023 (2013).

[20] Tarasov O. B., Portillo M., Amthor A. M., Baumann T., and Bazin D., *et al.*, Production of very neutron-rich nuclei with a ^{76}**Ge** beam, Phys. Rev. C **87**, 054612 (2013).

[21] Corradi L., Pollarolo G., and Szilner S., Multinucleon transfer processes in heavy-ion reactions, J. Phys. G **36**, 113101 (2009).

[22] Santra S., Singh P., Kailas S., Chatterjee A., Shrivastava A. and Mahata K.,Coupled reaction channel analysis of elastic, inelastic, transfer andfusion cross section for 12C+208Pb, Phys. Rev. C **64**, 024602 (2001).

[23] Liang J. F., Signorini C., FUSION INDUCED BY RADIOACTIVE ION BEAMS, Int. Jour. of Mod. Phys. E **14**, 1121 (2005).

[24] Bertulani C. A. and Gade A., Nuclear Astrophysics with Radioactive Beams, Phys. Rep. **485**, 195 (2010).

[25] Jonson B. and Richter A., More than three decades of ISOLDE physics, Hyp. Int. **129**, 1 (2000).

[26] *http:// www. cyc.ucl.ac.be/RIB/.*

[27] *http:// www. phy.ornl.gov/hrifb/.*

[28] *http://pro.ganil-spiral2.eu/laboratory/ganil-accelerators/spiral/introduction.*

[29] Habs D., Kester O., Seiber T., *et al.*, The REX-ISOLDE project, Hyp. Int. **129**, 43 (2000).

[30] *http:// www. triumph.ca/research/research-facilities/isac-facilities-for-rare-isotope-beams.*

[31] *http:// accelconf.web.cern.ch/accelconf/e00/PAPERS/WEP5B01.pdf.*

[32] *http://triac.kek.jp/en/.*

[33] *http://hie-isolde.web.cern.ch/HIE-ISOLDE/.*

[34] Lindroos M., Butler P. A., Huyse M., Riisager K., HIE-ISOLDE, Nucl. Instrum. Methods B **266**, 4687 (2008).

[35] *http://www.lnl.infn.it/ spes/.*

[36] Viyogi Y. P., Symons T. J. M., Doll P., Greiner D. E., and Heckman H. H., *et al.*, Fragmentations of ^{40}**Ar** at 213 MeV/Nucleon, Phys. Rev. Lett. **42**, 33 (1979).

[37] Anne R., Bazin D., The achromatic spectrometer LISE at GANIL , Nucl. Instr. Meth., Ser. A **257**, 215 (1987).

[38] Sherrill B. M., Morrissey D. J., Nolen J. A., and Winger J. A., The A1200 projectile fragment separator, Nucl. Instr. Meth., Ser. B **56/57**, 1106 (1992).

[39] Kubo T. *et al.*, In Proc. First Intl. Conf. on Radioactive Nuclear Beams, W.D. Myers, J.M. Nitschke, and E. Norman, eds. (World Scientific, Singapore, 1990) pp. 563.

[40] Geissel H., Armbruster P., Behr K. H., *et al.*, The GSI Projectile Fragment Separator (FRS): a versatile magnetic system for relativistic heavy ions, Nucl. Instr. Meth., Ser. B **70**, 286 (1992).

[41] Artukh A.G., Klygin S.A., Kononenko G.A., Kyslukha D.A., and Lukyanov S.M., *et al.*, Radioactive nuclear beams of COMBAS facility, Phys. Part. Nucl. **47**, 49 (2016).

[42] Mueller A.C., and Anne R., Production of and studies with secondary radioactive ion beams at LISE, Nucl. Instr. and Meth. B **56/57**, 559 (1991).

[43] Morrissey D.J., Sherrill B.M., Steiner M., Stolz A., Wiedenhoever I., Commissioning the A1900 projectile fragment separator, Nucl. Instr. and Meth. B **204**, 90 (2003).

[44] Kubo T., **et al.**, In-flight RI beam separator Big RIPS at RIKEN and elsewhere in Japan, Nucl. Instr. and Meth. B **204**, 97 (2003).

[45] Geissel H., Weick H., Winkler M., Münzenberg G., and Chichkine V., *et al.*, The Super-FRS project at GSI, Nucl. Instr. and Meth. B **204**, 71 (2003).

[46] Baur G, Bertulani C A, and Rebel H, Coulomb dissociation as a source of information on radiative capture processes of astrophysical interest, Nucl. Phys. A **458**, 188 (1986).

[47] Fermi E., $\ddot{U}$ber die Theorie des Stoβes zwischen Atomen und elektrisch geladenen Teilchen, Z. Phys. **29**, 315 (1924).

[48] Fermi E.,On the Theory of Collisions between Atoms and Electrically Charged Particles, Nuovo Cimento **2**, 143 (1925).

[49] Shubhchintak and Chatterjee R., Deformation effects in the Coulomb breakup of ^{31}Ne, Nucl. Phys. A **922**, 99 (2014).

[50] Nakamura T., *et al.*, Deformation-Driven p-Wave Halos at the Drip Line: ^{31}Ne, Phys. Rev. Lett. **112**, 142501 (2014).

[51] Haxel O., Jensen J., and Suess H., On the "Magic Numbers" in Nuclear Structure, Phys. Rev. **75**, 1766 (1949).

[52] Mayer M. G., On Closed Shells in Nuclei. II, Phys. Rev. **75**, 1969 (1949) .

[53] Stanoiu M., Sohler D., Sorlin O., Azaiez F., Mandal S., *et al.*, Disappearance of the N = 14 shell gap in the carbon isotopic chain, Phys.Rev. C **78**, 034315 (2008).

[54] Sorlin O. and Porquet M. G., Nuclear magic numbers: new features far from stability, Prog. Part. & Nucl. Phys. **61**, 602 (2008).

[55] Iwasaki H., *et al.*, Quadrupole deformation of ^{12}Be studied by proton inelastic scattering, Phys. Lett. B **481**, 7 (2000) .

[56] Motobayashi T., *et al.*, Large deformation of the very neutron-rich nucleus ^{32}Mg from intermediate-energy Coulomb excitation, Phys. Lett. B **346**, 9 (1995).

[57] Doornenbal P., Scheit H., Aoi N., Takeuchi S., and Li K., *et al.*, Spectroscopy of ^{32}Ne and the Island of Inversion, Phys. Rev. Lett. **103**, 032501 (2009).

[58] Ozawa A., *et al.*, New magic number, N = 16, near the neutron drip line, Phys. Rev. Lett. **84**, 5493 (2000).

[59] Hoffman, *et al.*, Evidence for a doubly magic ^{24}O, Phys. Lett. B **672**, 17 (2009).

[60] Cortina-Gil D., Fernandez-Vazquez J., Aumann T., T. Baumann,and Mandal S., et al., One-neutron knockout of ^{23}O, Eur.Phys.J. A **25**, 343 (2005).

[61] Kanungo R., *et al.*, One-neutron removal measurement reveals ^{24}O as a new doubly magic nucleus, Phys. Rev. Lett. **102**, 152501 (2009).

[62] Tshoo K., *et al.*, N=16 Spherical shell closure in ^{24}O, Phys. Rev. Lett. **109**, 022501 (2012).

[63] Doornenbal P., *et al.*, In-Beam γ -Ray Spectroscopy of ^{34,36,38}Mg : Merging the N = 20 and N = 28 Shell Quenching, Phys. Rev. Lett. **111**, 212502 (2013).

[64] Bastin B., *et al.*, Collapse of the N =28 Shell Closure in ^{42}Si, Phys. Rev. Lett. **99**, 022503 (2007).

[65] Warburton E. K., Becker J. A. and Brown B. A., Mass systematics for A=29 - 44 nuclei: The deformed A 32 region, Phys. Rev. C **41**, 1147 (1990).

[66] Orr N.A., Mittig W., Fifield L.K., Lewitowicz M., Plagnol E., Schutz Y., Long Zhan Wen, New mass measurements of neutron-rich nuclei near N = 20, Phys. Lett. B **258**, 29 (1991).

[67] Otsuka T., Suzuki T., Fujimoto R., Grawe H., and Akaishi Y., Evolution of Nuclear Shells due to the Tensor Force, Phys. Rev. Lett. **95**, 232502 (2005) .

[68] Detraz C., Guillemaud D., Huber G., Klapisch R., Langevin M., Naulin F., Thibault C., Carraz L. C., Touchard F., Beta decay of Na-27-32 and their descendants, Phys. Rev. C **19**, 164 (1979).

[69] Iwasacki H., Motobayashi T., Sakurai H., Yoneda K., and Gomi T., *et al.*, Large collectivity of Mg-34, Phys. Lett. B **522**, 227 (2001).

[70] Gade A., *et al.*, Spectroscopy of Mg-36: Interplay of Normal and Intruder Configurations at the Neutron-Rich Boundary of the 'Island of Inversion', Phys. Rev. Lett. **99**, 072502 (2007).

[71] Yoneda K., Sakurai H., Gomi T., Motobayashi T., and Aoi N., *et al.*, Deformation of 34 Mg studied via in-beam γ-ray spectroscopy using radioactive-ion projectile fragmentation, Phys. Lett. B **499**, 233 (2001).

[72] Campi X., Flocard H., Kerman A. K., and Koonin S., Shape transition in the neutron rich sodium isotopes, Nucl. Phys. A **251**, 193 (1975).

[73] Patra S. K. and Praharaj C. R., Relativistic mean field study of 'island of inversion' in neutron rich Ne, Na, Mg nuclei, Phys. Lett. B **273**, 13 (1991).

[74] Poves A.and Retamosa J., Theoretical study of the very neutron-rich nuclei around N = 20, Nucl. Phys. A **571**, 221 (1994).

[75] Utsuno Y., Otsuka T., Mizusaki T., and Honma M., Varying shell gap and deformation in N approximately 20 unstable nuclei studied by the Monte Carlo shell model, Phys. Rev. C **60**, 054315 (1999).

[76] Otsuka T., Fujimoto R., Utsuno Y., Brown B. A., Honma M., and Mizusaki T., Magic numbers in exotic nuclei and spin isospin properties of it N N interaction, Phys. Rev. Lett. **87**, 082502 (2001).

[77] Hamamoto I., Nilsson diagrams for light neutron-rich nuclei with weakly-bound neutrons, Phys. Rev. C **76**, 054319 (2007).

[78] Hamamoto I., Neutron shell structure and deformation in neutron-drip-line nuclei, Phys. Rev. C **85**, 064329 (2012) .

[79] Tanihata I., *et al.*, Phys. Rev. Lett. **55**, 2676 (1985).

[80] Hansen G. and Jonson B., The Neutron halo of extremely neutron-rich nuclei, Euro. Phys. Lett. **4**, 409 (1987).

[81] Banerjee P. and Shyam R., Structure of ^{19}C from Coulomb dissociation studies, Phys. Rev. C **61**, 047301 (1999).

[82] Jonson B., Light dripline nuclei, Phys. Rep. **389**, 1 (2004).

[83] Frederico T., Dalfino A., Tomio L., and Yamashita M., Universal aspects of light halo nuclei, Prog. Part. Nucl. Phys. **67**, 939 (2012).

[84] Tanihata I., Savajols H., and Kanungo R., Universal aspects of light halo nuclei, Prog. Part. Nucl. Phys. **68**, 215 (2013).

[85] Nakamura T., Fukuda N., Kobayashi T., Aoi N., and Iwasaki H., *et. al.*, Coulomb Dissociation of ^{19}C and its Halo Structure, Phys. Rev. Lett. **83**, 1112 (1999).

[86] Tanihata I. *et al.*, Determination of the density distribution and the correlation of halo neutrons in ^{11}Li, Phys. Lett. B **287**, 307 (1992).

[87] Fukuda M.*et al.*, Neutron halo in ^{11}Be studied via reaction cross sections, Phys. Lett. B **268**, 339 (1991).

[88] Rotival V. and Duguet T., New analysis method of the halo phenomenon in finite many-fermion systems: First applications to medium-mass atomic nuclei, Phys. Rev. C **79**, 054308 (2009).

[89] Chatterjee R., Shyam R., Tsushima K., and Thomas A. W., Structure and Coulomb dissociation of ^{23}O within the quark-meson coupling model, Nucl. Phys. A **913**, 116 (2013).

[90] Jurado B., *et al.*, Phys. Lett. **101**, 023210 (2007).

[91] Gaudefroy L., *et al.*, Direct mass measurements of ^{19}B,^{22}C,^{29}F,^{31}Ne,^{34}Na, and other light exotic nuclei, Phys. Rev. Lett. **109**, 202503 (2012).

[92] Takechi M., Ohtsubo T., Kuboki T., Fukuda M., Nishimura D., Suzuki T., Yamaguchi T., Ozawa A., Moriguchi T., Sumikama T., *et al.*, Measurements of nuclear radii for neutron -rich Ne isotopes $^{28-32}$Ne, Nucl. Phys. A, **834**, 412 (2010).

[93] Takechi M., Suzuki S., Nishimura D., Fukuda M., Ohtsubo T., Nagashima M., Suzuki T., Yamaguchi T., Ozawa A., Moriguchi T., *et al.*, Search for halo nucleus in Mg isotopes through the measurements of reaction cross sections towards the vicinity of neutron drip line, EPJ Web of Confs. **66**, 02101 (2014).

[94] Nakamura T., *et al.*, Coulomb dissociation of a halo nucleus ^{11}Be at 72A MeV, Phys. Lett. B. **331**, 296 (1994).

[95] Nunes F. M., Thompson I. J., and Johnson R. C., Core excitation in one neutron halo systems, Nucl. Phys. A **596**, 171 (1996).

[96] Aumann T., Navin A., Balamuth D. P., Bazin D., and Blank B., *et al.*, One-Neutron Knockout from Individual Single-Particle States of ^{11}Be, Phys. Rev. Lett. **84**, 35, (2000).

[97] Palit R., Adrich P., Aumann T., Boretzky K., Carlson, D. Cortina B. V., Pramanik U. Datta, Elze Th. W., Emling H., Geissel H., *et al.*, (LAND/FRS Collaboration), Exclusive measurement of breakup reactions with the one-neutron halo nucleus ^{11}Be, Phys. Rev. C **68**, 034318 (2003).

[98] Burbidge E., Burbidge G., Fowler W., and Hoyle F., Synthesis of the Elements in Stars, Rev. Mod. Phys. **29**, 547 (1957).

[99] Cameron A., Stellar Evolution, Nuclear Astrophysics, and Nucleogenesis, Technical Report CRL - 41 (1957).

[100] Coc A., Goriely S., Xu Y, Saimpert M., and Vangioni E., STANDARD BIG BANG NUCLEOSYNTHESIS UP TO CNO WITH AN IMPROVED EX-TENDED NUCLEAR NETWORK, Astrophys. J. **744**, 158 (2012).

[101] Suess H. and Urey H., Abundances of the elements, Rev. Mod. Phys. **28**, 53 (1956).

[102] Clayton D., Principles of stellar evolution and nucleosynthesis. The University of Chicago Press, (1983).

[103] Dutta S., Gangopadhyay G. and Bhattacharyya A., Neutron capture reactions relevant to the s and p processes in the region of the N=50 shell closure, Phys. Rev. C **94** , 024604 (2016).

[104] Lahiri C. and Gangopadhyay G., Neutron rich nuclei in a new binding energy formula and the astrophysical r-process, Int. J. Mod. Phys. E **21**, 1250042 (2012).

[105] Clayton D. and Ward R., S-Process Studies: Exact Evaluation of an Expo-nential Distribution of Exposures, Astrophys. J. **193**, 397 (1974).

[106] Arnould M., Goriely S., and Takahashi K., The r-process of stellar nucleosyn-thesis: Astrophysics and nuclear physics achievements and mysteries, Phys. Rep. **450**, 97 (2007).

[107] Thielemann F. K., ArconesA., Käppeli R., Liebendörfer M., Rauscher T., Winteler C., Fröhlich C., Dillmann I.,*et al.*, What are the astrophysical sites for the image-process and the production of heavy elements?, Prog. Part. Nucl. Phys. **66**, 346 (2011).

CHAPTER 2

THEORETICAL FORMALISM

2.1 Introduction

Theory and experiments go together while explaining the structure of drip line nuclei and reactions of astrophysics interest. With recent advances in radioactive ion beam (RIB) facilities it has become possible to do experiments on these exotic nuclei. The responsibility of a theoretician here is two fold, first to set various input parameters, for exotic nuclei as no prior knowledge is available on these near drip line isotopes so that experiments on such nuclei can be done. Second is to verify and explain the outcome of experiments by developing proper theoretical models. Coulomb dissociation (or break-up) [1] method is an important method to study structure and reaction of exotic nuclei. It can be used as an indirect method to study radiative capture.

Several mathematical approaches or models such as time-dependent models [2,3], Eikonal approximations [4,5], continuum discretised channel method(CDCC) [6,7] and distorted wave Born approximation(DWBA [8,9] can be used to study break-up reactions. All these models rely on the assumption that the projectile exhibits a

two- or three- cluster structure and interaction of these clusters can be stimulated by optical potentials. The main differences in these methods are approximation they use to solve the subsequent three-body Schrödinger equation. The starting point of all these methods is to solve the transition matrix or T-matrix. Thereby it can be further used to calculate the reaction observables. In section **2.2**, transition matrix is calculated for elastic break-up reaction. In section **2.3**, distorted wave Born approximation(DWBA) is discussed. In section **2.4**, Finite range distorted wave Born approximation (FRDWBA) using local momentum approximation (LMA) is explained.

2.2 The transition matrix for break-up reaction

Consider a break-up reaction in which a projectile a with wave vector $\mathbf{k}_a$ come under the influence of Coulomb and nuclear field of target t and is fragmented into two substructures b and c having wave vector $\mathbf{k}_b$ and $\mathbf{k}_c$, respectively. The Hamiltonian of the system can be written as

$$H = T_b + T_c + T_t + V_{bc} + V_{bt} + V_{ct} \tag{2.1}$$

where T_i is kinetic energy of particle i and V_{ij} repesents interaction between particle i and j. Separation between two substructures is given by $\mathbf{r}_{ij}$.

Asymptotic hamiltonians in initial (prior) and final(post) channels can be written as

$$H_i = T_b + T_c + T_t + V_{bc} \tag{2.2}$$

and

$$H_f = T_b + T_c + T_t. \tag{2.3}$$

respectively and corresponding interactions in respective channel are,

$$V_i = H - H_i = V_{bt} + V_{ct} \tag{2.4}$$

and

$$V_f = H - H_f = V_{bc} + V_{bt} + V_{ct}. \tag{2.5}$$

The transition matrix in post form and prior form [10] can be written as

$$T_{fi}^{(+)[post]} = \langle \exp^{i\mathbf{k}_c.\mathbf{r}_{ct}} \exp^{i\mathbf{k}_b.\mathbf{r}_{bt}} | V_{bc} + V_{bt} + V_{ct} | \psi_i^{(+)} \rangle \tag{2.6}$$

and

$$T_{fi}^{(-)[prior]} = \langle \psi_f^{(-)} | V_{bc} + V_{ct} | \exp^{i\mathbf{k}_a.\mathbf{r}_{at}} \phi_a(\mathbf{r}_{bc}) \rangle. \tag{2.7}$$

$\phi_a(\mathbf{r_{bc}})$ is exact ground state wavefunction of projectile. and $\mathbf{r}_{bc}$ is distance between the substructures. $\psi_i^{(+)}$ and $\psi_f^{(-)}$ are exact three-body wavefunction with outgoing and ingoing wave boundary condition and satisfy

$$H\psi_i^{(+)} = E\psi_i^{(+)} \tag{2.8}$$

and

$$H\psi_f^{(-)} = E\psi_i^{(+)} \tag{2.9}$$

respectively; E is total energy of the system.

Plane wavefunctions can be replaced by distorted wavefunctions assuming auxiliary potential acting on fragments because of Coloumb and nuclear field of target. This is realised by using Gell-Mann -Goldberger two potential formula [11].

T-matrices in both channels become,

$$T_{fi}^{(+)[post]} = \langle \chi^{(-)}(\mathbf{k}_c, \mathbf{r}_{ct}) \chi^{(-)}(\mathbf{k}_b, \mathbf{r}_{bt}) | V_{bc} + V_{bt} + V_{ct} - U_{bt} - U_{ct} | \psi_i^{(+)} \rangle$$

(2.10)

and

$$T_{fi}^{(-)[prior]} = \langle \psi_f^{(-)} | V_{ct} + V_{bt} - U_{at} | \chi^{(+)}(\mathbf{k}_a, \mathbf{r}_{at}) \phi_a(\mathbf{r}_{bc}) \rangle.$$

(2.11)

In the above equations, χ_i's and U_i are distorted wavefunctions and auxiliary potentials of particle i with respect to target respectively. Assuming $V_{bt} = U_{ct}$ and $V_{ct} = U_{ct}$ [12,13] in Eq.(2.10), post form T-matrix become

$$T_{fi}^{(+)[post]} = \langle \chi^{(-)}(\mathbf{k}_c, \mathbf{r}_{ct}) \chi^{(-)}(\mathbf{k}_b, \mathbf{r}_{bt}) | V_{bc} | \psi_i^{(+)} \rangle.$$

(2.12)

To solve the above equations we need further approximations for the total wavefunctions. One such approximation is the distorted wave Born approximation (DWBA) which is explained below.

2.3   Distorted wave Born approximation (DWBA)

As an approximation to the exact wavefunctions $\psi_i^{(+)}$ and $\psi_f^{(-)}$, distorted wave Born approxiamtion is used in Eqn. (2.11) and (2.12). For small inelastic excitations of projectile, the wavefunction $\psi_i^{(+)}$ is approximated by

$$\Psi_i^{(+)} \approx \chi_a^{(+)}(\mathbf{k}_a, \mathbf{r}_{at}) \phi_a(\mathbf{r}_{bc}).$$

(2.13)

Transition matrix in post form will become

$$T_{fi}^{(+)[post]}(DWBA) = \langle \chi_c^{(-)}(\mathbf{k}_c, \mathbf{r}_{ct}) \chi_b^{(-)}(\mathbf{k}_b, \mathbf{r}_{bt}) | V_{bc} | \chi_a^{(+)}(\mathbf{k}_a, \mathbf{r}_{at}) \phi_a(\mathbf{r}_{bc}) \rangle.$$

(2.14)

The other approximation is to neglect interaction between fragments in final channel and it gives

$$\Psi_f^{(-)} \approx \chi_b^{(-)}(\mathbf{k}_b, \mathbf{r}_{bt}) \chi_c^{(-)}(\mathbf{k}_c, \mathbf{r}_{ct}),$$

(2.15)

and then prior form DWBA T- matrix is given by

$$T^{(-)[prior]}(DWBA) = \langle \chi_b^{(-)}(\mathbf{k}_b, \mathbf{r}_{bt}) \chi_c^{(-)}(\mathbf{k}_c, \mathbf{r}_{ct}) | V_{ct} + V_{bt} - V_{at} | \chi_a^{(+)}(\mathbf{k}_a, \mathbf{r}_{at}) \phi_a(\mathbf{r}_{bc}) \rangle.$$

(2.16)

The above two versions of the T- matrices Eqs.[2.14, 2.16] have been shown to be equal in [14]. The post form DWBA is widely used in [1, 15–17], as it has the advantage of having a short range potntial, V_{bc} in Eq. 2.14. On the other hand the potential in prior form $V_{ct} + V_{bt} - U_{at}$, appearing in Eq. 2.16, will involve complex coordinate transformations. Numerical calculations in post form is thus easier to perform than the prior form.

2.4 Coulomb break-up with finite range distorted wave Born approximation (FRDWBA)

Consider a break-up reaction of a projectile a into the core fragment b and the valence neutron n [1] in the Coulomb field of a target t which can be represented as

---

[1] We replace substructure c (charged or uncharged) with chargeless particle, neutron. So c from above sections will be replaced with n. Consequently, the distorted wave $\chi_c^{(-)}$ will be replaced by a plane wave, in the Coulomb field of the target.

$a + t \to b + n + t$. We assume that target nucleus remains in its ground state during the break-up process. Thus this is also known as the elastic Coulomb break-up reaction. The chosen coordinate system is shown in Fig. (2.1).
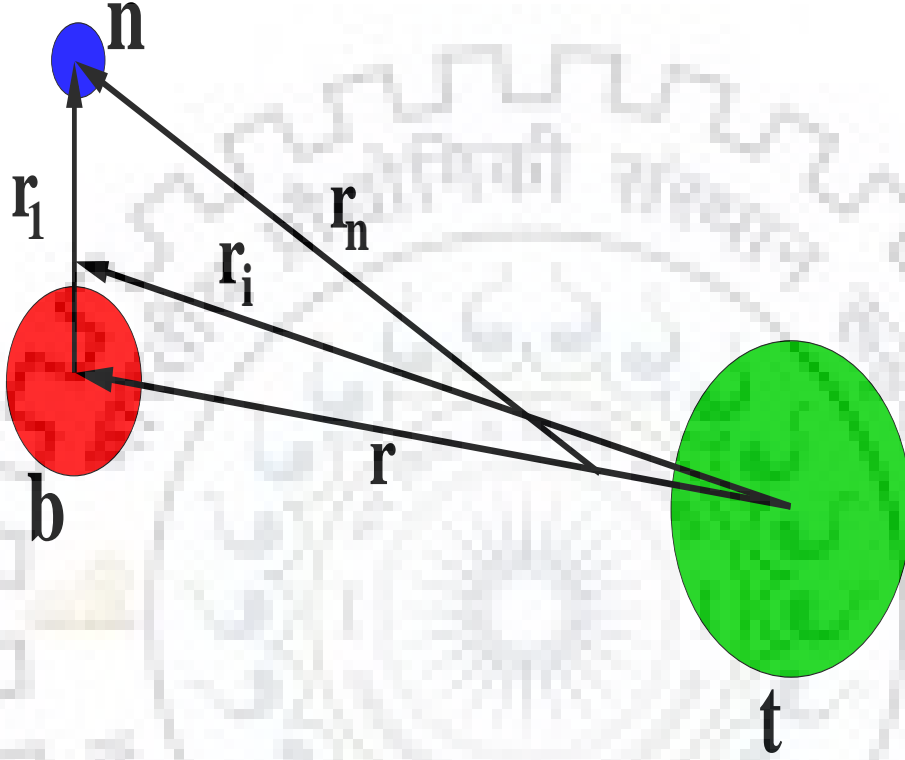
Figure 2.1: The three-body coordinate system. The charged core fragment, the valence neutron and the target nucleus are denoted by b, n and t, respectively.

The position vectors satisfy the following relations:

$$\mathbf{r} = \mathbf{r}_i - \alpha \mathbf{r}_1, \quad \alpha = \frac{m_n}{m_n + m_b}, \tag{2.17}$$

$$\mathbf{r}_n = \gamma \mathbf{r}_1 + \delta \mathbf{r}_i, \quad \delta = \frac{m_t}{m_b + m_t}, \quad \gamma = (1 - \alpha\delta). \tag{2.18}$$

The starting point of the FRDWBA theory of Coulomb break-up is the post-form T-matrix of the reaction given by

$$T = \int d\xi d\mathbf{r}_1 d\mathbf{r}_i \chi_b^{(-)*}(\mathbf{k}_b, \mathbf{r}) \Phi_b^*(\xi_b) \chi_n^{(-)*}(\mathbf{k}_n, \mathbf{r_n}) \Phi_n^*(\xi_n) V_{bn}(\mathbf{r}_1) \Psi_a^{(+)}(\xi_a, \mathbf{r}_1, \mathbf{r}_i). \tag{2.19}$$

The functions χ are the distorted waves for the relative motions of b and n with respect to t and the center of mass (c.m.) of the $b + t$ system, respectively. The functions Φ are the internal state wavefunctions of the concerned particles dependent on the internal coordinates ξ. The function $\Psi_a^{(+)}(\xi_a, \mathbf{r}_1, \mathbf{r}_i)$ is the exact three-body scattering wavefunction of the projectile with a wave vector $\mathbf{k}_a$ satisfying outgoing boundary conditions. The vectors $\mathbf{k}_b$ and $\mathbf{k}_n$ are the Jacobi wave vectors of b and n, respectively, in the final channel of the reaction. The function $V_{bn}(\mathbf{r}_1)$ represents the interaction between b and n. As we concentrate only on Coulomb break-up, the function $\chi_b^{(-)}(\mathbf{k}_b, \mathbf{r})$ is taken as the Coulomb distorted wave (for a point Coulomb interaction between the charged core b and the target) satisfying incoming wave boundary conditions, and the function $\chi_n^{(-)}(\mathbf{k}_n, \mathbf{r}_n)$ describing the relative motion of the neutron with respect to the target, is just a plane wave. It may be noted that within this approach the fragment-target interactions are treated to all orders.

In the distorted wave Born approximation (DWBA), we write

$$\Psi_a^{(+)}(\xi_a, \mathbf{r}_1, \mathbf{r}_i) = \Phi_a(\xi_a, \mathbf{r}_1)\chi_a^{(+)}(\mathbf{k}_a, \mathbf{r}_i), \qquad (2.20)$$

The assumption inherent in Eq. (2.20) is that the break-up channels are very weakly coupled and hence this coupling needs to be treated only in the first order. We expect this approximation to be valid for those cases where there are no resonances in the $n + b$ continuum. Most of the neutron halo systems come in this category. For those cases where higher order effects of fragment-fragment interaction are non-negligible, the applicability of this method would be limited. Ideally, a rigorous description of the break-up process of all types of projectiles would require the use of Faddeev type of three-body methods that include Coulomb potentials in the fragment-target and fragment-fragment (if required) interactions. A few such calculations have become available recently although they are confined to the break-up reactions on a proton target [18–21].

In Eq. (2.20) the dependence of Φ_a on $\mathbf{r}_1$ describes the relative motion of the frag-

ments b and n in the ground state of the projectile. The function $\chi_a^{(+)}(\mathbf{k}_a, \mathbf{r}_i)$ is the Coulomb distorted scattering wave describing the relative motion of the c.m. of the projectile with respect to the target, satisfying outgoing wave boundary conditions.

The integration over the internal coordinates ξ in the T-matrix gives

$$\int d\xi \Phi_b^*(\xi_b)\Phi_n^*(\xi_n)\Phi_a(\xi_a, \mathbf{r}_1) = \sum_{\ell m j \mu} \langle \ell m j_n \mu_n | j \mu \rangle \langle j_b \mu_b j \mu | j_a \mu_a \rangle i^\ell \Phi_a(\mathbf{r}_1,$$
(2.21)

The ground state wavefunction $\Phi_a(\mathbf{r}_1)$ can be expressed in terms of its radial, $u_\ell(r_1)$ and angular parts, $Y_\ell^m(\hat{\mathbf{r}}_1)$ assuming a particular partition, in which the relative motion between n and b has an orbital angular momentum ℓ as

$$\Phi_a(\mathbf{r}_1) = \sqrt{C^2 S}\, u_\ell(r_1) Y_\ell^m(\hat{\mathbf{r}}_1),$$
(2.22)

where $C^2 S$ is the spectroscopic factor for the given partition. In Eq. (2.21), ℓ is coupled to the spin of n and the resultant channel spin j is coupled to the spin j_b of the core b to yield the spin of a (j_a). The partition represented by Eq. (2.22) will be retained even if the potential $V_{bn}(\mathbf{r}_1)$ is deformed.

The T-matrix can now be written as

$$T = \sum_{\ell m j \mu} \langle \ell m j_n \mu_n | j \mu \rangle \langle j_b \mu_b j \mu | j_a \mu_a \rangle i^\ell \hat{\ell} \beta_{\ell m}(\mathbf{k}_b, \mathbf{k}_n; \mathbf{k}_a),$$
(2.23)

where

$$\hat{\ell}\beta_{\ell m}(\mathbf{k}_b, \mathbf{k}_n; \mathbf{k}_a) = \int d\mathbf{r}_1 d\mathbf{r}_i \chi_b^{(-)*}(\mathbf{k}_b, \mathbf{r}) e^{-i\mathbf{k}_n.\mathbf{r}_n}$$
$$\times V_{bn}(\mathbf{r}_1) u_\ell(r_1) Y_\ell^m(\hat{\mathbf{r}}_1) \chi_a^{(+)}(\mathbf{k}_a, \mathbf{r}_i).$$
(2.24)

with $\beta_{\ell m}$ being the reduced T-matrix and with $\hat{\ell} \equiv \sqrt{2\ell + 1}$.

Eq. (2.24) involves a six dimensional integral which makes the computation of $\beta_{\ell m}$ quite complicated. The problem gets further acute because the integrand involves a

product of three scattering waves that exhibit oscillatory behavior asymptotically. In the past calculations have been simplified by using approximate methods, such as the zero-range approximation (see e.g., [10, 22, 23]) or the Baur-Trautmann approximation [1, 24] that led to the factorization of the T-matrix into two terms; each involving three-dimensional integrals (we refer to [25] for a detailed discussion). However, these methods are not valid for break-up reactions at higher beam energies and for heavier projectiles that can have non-s-wave ground states.

In our FRDWBA theory we use a method that was proposed in Ref. [26] for describing the heavy ion induced transfer reactions, and was adopted in Ref. [27] for describing the break-up reactions of heavy projectiles. This was shown [25, 28] to be well suited for calculating the Coulomb break-up of halo nuclei. In this method, the Coulomb distorted wave of particle b in the final channel is written as [28]

$$\chi_b^{(-)}(\mathbf{k}_b, \mathbf{r}) = e^{-i\alpha \mathbf{K}.\mathbf{r}_1} \chi_b^{(-)}(\mathbf{k}_b, \mathbf{r}_i). \tag{2.25}$$

Eq. (2.25) represents an exact Taylor series expansion about $\mathbf{r}_i$ if $\mathbf{K} = -i\nabla_{\mathbf{r}_i}$ is treated exactly. However, instead of doing this we employ a local momentum approximation (LMA) where the magnitude of momentum $\mathbf{K}$ is taken to be

$$K(\mathcal{R}) = \sqrt{\frac{2m}{\hbar^2}(E - V(\mathcal{R}))}. \tag{2.26}$$

Here m is the reduced mass of the $b-t$ system, E is the energy of particle b relative to the target in the c.m. system and $V(\mathcal{R})$ is the Coulomb potential between b and the target separated by $\mathcal{R}$. Thus, the magnitude of the momentum of $\mathbf{K}$ is evaluated at some separation $\mathcal{R}$, which is held fixed for all the values of r. The value of $\mathcal{R}$ was taken to be equal to 10 fm. For reactions under investigation in this research work, the magnitude of $\mathbf{K}$ remains constant for distances larger than 10 fm. Due to the peripheral nature of the break-up reaction, the region $\mathcal{R} \gtrsim 10$ fm contributes maximum to the cross-section. Furthermore, the results of the calculations for these reactions, at the beam energies under investigation, are almost independent of the

choice of the direction of momentum $\mathbf{K}$ [28]. Therefore, we have taken the directions of $\mathbf{K}$ and $\mathbf{k_b}$ to be the same in all the calculations presented in this chapter.

Substituting Eq. (2.25) into Eq. (2.24), the reduced amplitude is obtained in a factorized form as

$$
\hat{\ell}\beta_{\ell m} = \int d\mathbf{r}_i e^{-i\delta\mathbf{k}_n.\mathbf{r}_i} \chi_b^{(-)*}(\mathbf{k}_b, \mathbf{r}_i)\chi_a^{(+)}(\mathbf{k}_a, \mathbf{r}_i)
$$
$$
\times \int d\mathbf{r}_1 e^{-i\mathbf{Q}.\mathbf{r}_1} V_{bn}(\mathbf{r}_1)u_\ell(r_1)Y_\ell^m(\hat{\mathbf{r}}_1), \qquad (2.27)
$$

where, $\mathbf{Q} = \gamma\mathbf{k}_n - \alpha\mathbf{K}$. The first integral in Eq. (2.27), is the dynamics part in the Coulomb break-up and the second integral in Eq. (2.27) contains the projectile structure information and Eq.(2.27) can be writen as

$$
\hat{\ell}\beta_{\ell m} = I_d \times I_f \qquad (2.28)
$$

In Eq. (2.28), I_d represents the dynamics of the reaction and the second part I_f contains information about the structure of projectile.

Solution of dynamics part, I_d

In Eq. (2.27), I_d can be simplified further using Coulomb distorted waves for $\chi_a^{(+)}(\mathbf{k}_a, \mathbf{r}_i)$ and $\chi_b^{(-)*}(\mathbf{k}_b, \mathbf{r}_i)$ and subsequently by finding an analytic solution to the integral. Using

$$
\chi_a^{(+)}(\mathbf{k}_a, \mathbf{r}_i) = e^{-\pi\eta_a/2}\Gamma(1 + i\eta_a)e^{i\mathbf{k}_a.\mathbf{r}_i}\,_1F_1(-i\eta_a, 1, i(k_a r_i - \mathbf{k}_a.\mathbf{r}_i)), \qquad (2.29)
$$
$$
\chi_b^{(-)*}(\mathbf{k}_b, \mathbf{r}_i) = e^{-\pi\eta_b/2}\Gamma(1 + i\eta_b)e^{-i\mathbf{k}_b.\mathbf{r}_i}\,_1F_1(-i\eta_b, 1, i(k_b r_i + \mathbf{k}_b.\mathbf{r}_i)), \qquad (2.30)
$$

we have

$$I_d = \int d\mathbf{r}_i e^{-\pi\eta_a/2}\Gamma(1+i\eta_a)e^{-\pi\eta_b/2}\Gamma(1+i\eta_b)e^{i\tilde{\mathbf{Q}}.\mathbf{r}_i}{}_1F_1(-i\eta_a, 1, i(k_a r_i - \mathbf{k}_a.\mathbf{r}_i))$$

$$\times {}_1F_1(-i\eta_b, 1, i(k_b r_i + \mathbf{k}_b.\mathbf{r}_i)).$$

(2.31)

Here η is Sommerfeld parameter and ${}_1F_1(a, b; c; z)$ is hypergeometric function. Eq.(2.31) can be expressed analytically in terms of the Bremsstrahlung integral [29] ($\tilde{\mathbf{Q}} = \mathbf{k}_a - \mathbf{k}_b - \delta\mathbf{k}_n$) and hence can be calculated as,

$$I_d = e^{-\pi\eta_a/2}\Gamma(1+i\eta_a)e^{-\pi\eta_b/2}\Gamma(1+i\eta_b)$$

$$\times \int d\mathbf{r}_i e^{i\tilde{\mathbf{Q}}.\mathbf{r}_i}{}_1F_1(-i\eta_a, 1, i(k_a r_i - \mathbf{k}_a.\mathbf{r}_i)){}_1F_1(-i\eta_b, 1, i(k_b r_i + \mathbf{k}_b.\mathbf{r}_i))$$

$$= e^{-\pi\eta_a/2}\Gamma(1+i\eta_a)e^{-\pi\eta_b/2}\Gamma(1+i\eta_b) \times I_B. \quad (2.32)$$

The Bremsstrahlung integral, I_B, can be analytically expressed as,

$$I_B = -i\Big[B(0)\big(\frac{d\zeta}{d\lambda}\big)_{\lambda=0}(-\eta_a\eta_b){}_2F_1(1-i\eta_a, 1-i\eta_b); 2; \zeta(0))$$

$$+\big(\frac{dB}{d\lambda}\big)_{\lambda=0}{}_2F_1(-i\eta_a, -i\eta_b); 1; \zeta(0))\Big],$$

(2.33)

where

$$B(\lambda) = \frac{4\pi}{k^{2(i\eta_a+i\eta_b+1)}}\Big[(k^2 - 2\mathbf{k}.\mathbf{k}_a - 2\lambda k_a)^{i\eta_a}(k^2 - 2\mathbf{k}.\mathbf{k}_b - 2\lambda k_b)^{i\eta_b}\Big], \quad (2.34)$$

and

$$\zeta(\lambda) = \frac{2k^2(k_b k_a + \mathbf{k}_b.\mathbf{k}_a) - 4(\mathbf{k}.\mathbf{k}_b - \lambda k_b)(\mathbf{k}.\mathbf{k}_a + \lambda k_a)}{(k^2 - 2\mathbf{k}.\mathbf{k}_a - 2\lambda k_a)(k^2 - 2\mathbf{k}.\mathbf{k}_b - 2\lambda k_b)}. \quad (2.35)$$

Solution of structure part, I_f

Using $\mathbf{Q} = \gamma\mathbf{k_n} - \alpha\mathbf{K}$ and $\phi_a^{\ell m}(\mathbf{r_1}) = u_\ell(r_1)Y_\ell^m(\hat{\mathbf{r}_1})$,

$$I_f = \int d\mathbf{r_1} e^{-i\mathbf{Q}.\mathbf{r_1}} V_{bn}(r_1) u_\ell(r_1) Y_\ell^m(\hat{\mathbf{r}}_1). \tag{2.36}$$

Expanding the exponential in Eq. 2.36 in terms of spherical harmonics

$$e^{-i\mathbf{Q}.\mathbf{r_1}} = 4\pi \sum_{l_1 m_1} i^{-l_1} j_{l_1}(Qr_1) Y_{l_1}^{m_1*}(\hat{\mathbf{r}}_1) Y_{l_1}^{m_1}(\hat{\mathbf{Q}}) \tag{2.37}$$

and using 2.37 in 2.36, structure factor, I_f reduces to

$$
\begin{aligned}
I_f &= 4\pi \sum_{l_1 m_1} i^{-l_1} Y_{l_1}^{m_1}(\hat{\mathbf{Q}}) \int r_1^2 dr_1 j_{l_1}(Qr_1) V_{bn}(r_1) u_\ell(r_1) \int d\mathbf{\Omega}_{r_1} Y_{l_1}^{m_1*}(\hat{\mathbf{r}}_1) Y_\ell^m(\hat{\mathbf{r}}_1) \\
&= 4\pi \sum_{l_1 m_1} i^{-l_1} Y_{l_1}^{m_1}(\hat{\mathbf{Q}}) \int r_1^2 dr_1 j_{l_1}(Qr_1) V_{bn}(r_1) u_\ell(r_1) \delta_{l_1,\ell} \delta_{m_1,m} \\
&= 4\pi i^{-\ell} Y_\ell^m(\hat{\mathbf{Q}}) I_{F\ell},
\end{aligned}
\tag{2.38}
$$

where

$$I_{F\ell} = \int r_1^2 dr_1 j_\ell(Qr_1) V_{bn}(r_1) u_\ell(r_1). \tag{2.39}$$

From Eq. 2.39 it's clear that ground state wavefunction of any angular momentum configuration is an input to the theory. Substituting Eqns.(2.32, 2.38) in Eq. (2.27) the reduced T-marix can be evaluated in the post form finite range distorted wave Born approximation. It is worth noting that, electromagnetic interaction between the fragments and the target are included up to all orders and entire non-resonant continuum (corresponding to all multipoles and relative orbital angular momentum between the fragments) are included in the theory. Ground state wave function of the projectile is taken as the only input in this theory and hence one avoids the uncertainties associated with multipole strength distributions of the projectile [1,28]. The analytic nature of this theory stems from the fact that pure Coulomb wave functions are used in the calculation and that the dynamics can be analytically

evaluated.

The triple differential cross-section for the reaction is related to reduced transition amplitude $\beta_{\ell m}$ as

$$\frac{d^3\sigma}{dE_b d\Omega_b d\Omega_n} = \frac{2\pi}{\hbar v_a} \rho(E_b, \Omega_b, \Omega_n) \sum_{\ell m} |\beta_{\ell m}|^2, \tag{2.40}$$

where v_a is the $a - t$ relative velocity in the entrance channel and $\rho(E_b, \Omega_b, \Omega_n)$ is the phase space factor appropriate to the three-body final state [30] and is given by (see Appendix B)

$$\rho(E_b, \Omega_b, \Omega_n) = \frac{h^{-6} m_b m_n m_t p_b p_n}{m_t + m_n - m_n \frac{\mathbf{p}_n \cdot (\mathbf{p}_a - \mathbf{p}_b)}{p_n^2}}, \tag{2.41}$$

where m_i and p_i are the mass and linear momenta of the particle i. Once triple differential cross-section is calculated, various reaction observables such as relative energy spectra, parallel momentum distribution can be calculated. The parallel momentum distribution (PMD) of the charged fragment b [31–33] can be calculated as

$$\frac{d\sigma}{dp_z} = \int d\Omega_n dp_x dp_y m_b p_b \frac{2\pi}{\hbar v_a} \rho(E_b, \Omega_b, \Omega_n)$$

$$\times \left\{ \sum_{\ell m} \frac{1}{(2\ell + 1)} |\beta_{\ell m}|^2 \right\}, \tag{2.42}$$

Here p_x and p_y are the x- and y- components of the momentum p_b of fragment. From the PMD distribution of the charged particle b, full width at half maximum (FWHM) is calculated. For stable nuclei the value of FWHM is about $120 - 140$ Mev/c whereas for halo nuclei this value is around 44 MeV/c.

The relative energy spectra $(\frac{d\sigma}{dE_{bn}})$ [34, 35] of the outgoing fragments is given by

$$\frac{d\sigma}{dE_{rel}} = \int_{\Omega_{bn}\Omega_{at}} d\Omega_{bn} d\Omega_{at}$$

$$\times \sum_{\ell m} \frac{1}{(2\ell+1)} |\beta_{\ell m}|^2 \frac{2\pi}{\hbar v_{at}} \frac{\mu_{bn}\mu_{at}p_b p_{at}}{h^6}, \qquad (2.43)$$

where E_{rel} is the $b-n$ relative energy in the final channel, v_{at} is the $a-t$ relative velocity in the initial channel, Ω_{bn} and Ω_{at} are solid angles, μ_{bn} and μ_{at} are the reduced masses and p_{bn} and p_{at} are linear momenta of the $b-n$ and $a-t$ systems, respectively.

The formalism explained above will be used in chapters 3 and 4. The Eq.(2.27) can be further extended to account for a deformed nuclei as done in chapter 3. Eq.(2.42) is used to calculate parallel momentum distribution of the charged fragment in the final channel and is used in chapter 3. Using Eq.(2.43) we will calculate photodisintegration cross-section and subsequently the radiative capture cross-section in chapter 4.

BIBLIOGRAPHY

[1] Baur G., Rösel F., Trautmann D., and Shyam R., Fragmentation processes in nuclear reactions, Phys. Rep. **111**, 333 (1984) .

[2] Typel S. and Wolter H., Dynamical Description of Coulomb Dissociation*, Z. Naturforsch. **54**, 63 (1999).

[3] Capel P., Goldstein G., and Baye D., Time-dependent analysis of the breakup of Be-11 on C-12 at 67- MeV/nucleon, Phys. Rev. C **70**, 064605 (2004).

[4] Glauber R. J., Lectures in Theoretical Physics, eds. W. E. Brittin and L. G. Dunham, Interscience Publ., New York, (1959).

[5] Esbensen H., and Bertsch G. F., Eikonal approximation in heavy-ion fragmentation reactions, Phys. Rev. C **64**, 014608 (2001).

[6] Kawai M., Foundations of the Continuum-Discretized Coupled Channels Analysis of the Deuteron-Nucleus Three-Body Model, Prog. Theor. Phys. **80**, 694 (1988).

[7] Matsumoto T., Kamizato T., Ogata K., and Iseri Y., *et.al.*, New treatment of breakup continuum in the method of continuum discretized coupled channels, Phys. Rev. C **68**, 064607 (2003).

[8] Shyam R., Banerjee P., and Baur G., Coulomb dissociation of ^{11}Li and ^{11}Be in a direct fragmentation model, Nucl. Phys. A **540**, 341 (1992).

[9] Chatterjee R., Full quantal theory of one-neutron halo breakup reactions, Phys. Rev. C **68**, 044604 (2003).

[10] Satchler G. R., *Direct Nuclear Reactions*, Oxford University Press, New York, (1991).

[11] Gell-Mann M. and Goldberger M. L., The Formal Theory of Scattering, Phys. Rev. **91**, 398 (1953).

[12] Levin F. S., Particle transfer reactions as probes of particle unstable states, Ann. Phys. **46**, 41 (1968).

[13] Vincent C. M., Gell-Mann-Goldberger Relation for Reactions of the Form **(d,pn)**, Phys. Rev. **175**, 1309 (1968).

[14] Huby R. and Mines J. R., Distorted-Wave Born Approximation for Stripping to Virtual Levels, Rev. Mod. Phys. **37**, 406 (1965).

[15] Chatterjee R., Progress in all-order breakup reaction theories, Pramana - J. Phys. **75**, 127 (2010).

[16] Baur G. and Trautmann D., Sub-Coulomb (d, p) stripping theory into the continuum, Nucl. Phys. A **199**, 218 (1973); The break-up of the deuteron and stripping to unbound states, Phys. Rep. **25**, 293 (1976); Baur G., Rösel F. and Trautmann D., Investigations of the deuteron break-up on heavy nuclei above the Coulomb barrier, Nucl. Phys. A **265**, 101 (1976).

[17] Pampus J, Bisplinghoff J., Ernst J., and Mayer-Kuckuk T., *et.al.*, Inclusive proton spectra from deuteron break-up: Theory and experiment, Nucl. Phys. A **311**, 141 (1978); Kleinfeller J., Bisplinghoff J., Ernst J., Mayer-Kuckuk T., *et.al.*, Study of inclusive proton spectra from low energy deuteron reactions in

terms of spectator break-up and coulomb dissociation of the projectile, Nucl. Phys. A **370**, 205 (1981).

[18] Deltuva A. and Fonseca A. C., Three-body Faddeev-Alt-Grassberger-Sandhas approach to direct nuclear reactions, Phys. Rev. C **79**, 014606 (2009) .

[19] Crespo R., Deltuva A., Rodriguez-Gallardo M., Cravo E., and Fonseca A. C., Spectroscopy of unbound states under quasifree scattering conditions: One-neutron knockout reaction of ^{14}B, Phys. Rev. C **79**, 014609 (2009) .

[20] Cravo E., Crespo R., Moro A. M., and Deltuva A., Probing nucleon-nucleon interactions in breakup of the one-neutron halo nucleus ^{11}Be on a proton target, Phys. Rev. C **81**, 031601 (2010) .

[21] Upadhyay N. J., Deltuva A., and Nunes F. M., Testing the continuum-discretized coupled channels method for deuteron-induced reactions, Phys. Rev. C **85**, 054621 (2012).

[22] Austern N., *Direct Nuclear Reactions Theory*, (Wiley, New York, 1970).

[23] Glendenning N., *Direct Nuclear Reaction*, (Academic 1983).

[24] Baur G. and Trautmann D., The Coulomb break-up of the deuteron, Nucl. Phys. A **191**, 321 (1972).

[25] Shyam R. and Danielewicz P., Core excitation in Coulomb breakup reactions, Phys. Rev. C **63**, 054608 (2001).

[26] Braun-Munzinger P. and Harney H. L., An approximate treatment of recoil effects in heavy ion transfer reactions, Nucl. Phys. A **233**, 381 (1974).

[27] Shyam R. and Nagarajan M. A., A Distorted-Wave Born-Approximation Theory of Heavy-Ion-Induced Projectile Breakup Reactions, Ann. Phys. (N.Y.) **163**, 265 (1985).

[28] Chatterjee R., Banerjee P. and Shyam R., Projectile structure effects in the Coulomb breakup of one-neutron halo nuclei, Nucl. Phys. A **675**, 477 (2000).

[29] Nordsieck, Reduction of an Integral in the Theory of Bremsstrahlung, Phys. Rev. **93**, 785 (1954).

[30] Fuchs H., On cross section transformations in reactions with three outgoing fragments, Nucl. Instrum. Methods **200**, 361 (1982).

[31] Orr N. A., Anantaraman N., Austin S. M., and Bertulani C. A., *et.al.*, Momentum distributions of ^{9}Li fragments from the breakup of ^{11}Li and the neutron halo, Phys. Rev. C **51**, 3116 (1995).

[32] Bazin D., Brown B. A., Brown J., and Fauerbach M., *et. al.*, One-Neutron Halo of ^{19}C, Phys. Rev. Lett. **74**, 3569 (1995).

[33] Banerjee P., and Shyam R., Momentum distribution of fragments in reactions induced by neutron rich nuclei, Phys. Lett. B **349**, 421 (1995).

[34] Bertulani C. A., and Baur G., Electromagnetic processes in relativistic heavy ion collisions, Phys. Rep. **163**, 299 (1988).

[35] Bertulani C. A., and Gade A, Nuclear astrophysics with radioactive beams, Phys. Rep. **485**, 195 (2010).

CHAPTER 3

STUDY OF GROUND STATE OF DEFORMED NUCLEUS ^{37}Mg

3.1 Introduction

In this chapter we will calculate Coulomb break-up of the neutron rich nucleus ^{37}Mg on a Pb target at the beam energy of 244 MeV/nucleon within the framework of a finite range distorted wave Born approximation (FRDWBA) theory that is extended to include the effects of projectile deformation. In this theory, the break-up amplitude involves the full wavefunction of the projectile ground state. The total one-neutron removal cross-section (σ_{-1n}), the neutron-core relative energy spectrum, the parallel momentum distribution of the core fragment, the valence neutron angular, and energy-angular distributions will be calculated. The calculated σ_{-1n} will be compared with the recently measured data to put constraints on the spin parity, and the one-neutron separation energy (S_n) of the ^{37}Mg ground state (^{37}Mg$_{gs}$). The dependence of σ_{-1n} on the deformation of this state will be investigated. We will study the narrow parallel momentum distribution of the core fragment and the

strong forward peaking of the valence neutron angular distribution to suggest a one-neutron halo configuration of the ^{37}Mg ground state. In section **3.2** we will present brief review of ^{37}Mg. In the section **3.3**, we present our formalism where we recall some important aspects of the FRDWBA theory of break-up reactions and its extension to include the deformation of the projectile ground state. The results of our calculations are presented in section **3.4**, where we discuss the one-neutron removal cross-section, the relative energy spectra of the fragments, the parallel momentum distribution of the core fragment, the angular and energy distribution of valence neutron as a function of the projectile deformation. The summary and conclusions of our study are presented in section **3.5**.

3.2   Brief review of ^{37}Mg

With the advances made in the technology of producing nuclear species with relatively large neutron (N) to proton (Z) number ratios, it is now possible to extensively study nuclei near the neutron-drip line with $Z > 8$. During the last three decades measurements performed on mass, radius and spectroscopy of such nuclei have shown that they have structures that are at variance with those of their "near the line of stability" counterparts.

With the advent of new generation of radioactive ion beam facilities, it has now become possible not only to produce medium mass neutron rich nuclei in the vicinity of the magic numbers but also employ them as projectiles to initiate reactions (e.g., break-up) on nuclear targets [1, 2]. This provides excellent opportunity to perform quantitative study of the single-particle structure and the shell evolution in this region. It is predicted that in the region of Ne, Na, and Mg isotopes near N = 20 − 22, ground states to have intruder $\nu(sd)^{-}2(fp)^2$ configuration [3] which leads to disappearance of magic number $N = 20$ and mass measurement [4] also confirm the same. It is suggested that nucleon- nucleon tensor interaction [5, 6] can be the reason for the shell- gap quenching. Low excitation energies and large B(E2) suggests

large deformation in the nuclei [7–11]. It is suggested by work [12, 13] on neutron drip-line nuclei in region $N = 20-28$ most nuclei are to be deformed. The root mean square radius (RMS) of a deformed nucleus becomes effectively larger than that of a spherical one. This enhances the total reaction cross-section (σ_R) that depends on RMS radii of the projectile and the target nuclei. Large interaction cross-sections (which are almost the same as the σ_R) have been measured for $^{29-32}$Ne [14, 15] and $^{24-38}$Mg [16] nuclei. This has led to the conclusion that the isotopes $^{29-32}$Ne have strong deformation [17–19]. For the Mg case, these studies [19, 20] suggest that while ^{27}Mg and ^{30}Mg are spherical, $^{25,29,33-38}$Mg are more likely to be deformed. The reason for large interaction cross-section can be valence nucleon has extended density distribution (i.e. halo structure) and ^{37}Mg can have halo structure. Recently, measurements of σ_R for $^{24-38}$Mg isotopes on ^{12}C target at the beam energy of 240 MeV/nucleon have been reported in Ref. [16]. From a similar reasoning, it was suggested in this study that ^{37}Mg ($Z = 12, N = 25$) that lies in $N = 20 - 28$ island of inversion, is also a candidate for having a one-neutron halo structure. This was reinforced by measurements of Coulomb break-up of ^{37}Mg on C and Pb targets at the beam energy of 244 MeV/nucleon in Ref. [2].

^{37}Mg is the most neutron-rich bound odd-mass Mg isotope. However, the experimental information about its mass and the ground state spin parity is not available, even though mass systematics suggest that it is a very weakly bound system with S_n in the range of 0.16 ± 0.68 MeV [21]. Therefore, it is another promising candidate for having a one-neutron halo structure in island of inversion near $N = 20 - 28$. However, a $1f_{7/2}$ configuration for its ground state that would result in the conventional spherical shell model, will suppress the halo formation due to the high centrifugal barrier. Hence, a significant modification of its spherical shell structure with introduction of the intruder configurations having s- and p-wave states, is necessary for this nucleus to have a halo like structure. This also implies that its ground state should be deformed.

The aim of this chapter is to investigate the one-neutron removal cross-section of

^{37}Mg on a Pb target at the beam energy of 244 MeV/nucleon within the FRDWBA theory of Coulomb break-up reactions. By comparing the σ_{-1n} calculated within this theory with the corresponding experimental data we would like to extract most plausible spin-parity for the ground state of this nucleus. We attempt to put constraints on the large uncertainty in its S_n value. We investigate the effect of the ground state deformation of this nucleus on the values of σ_{-1n} deduced in our analysis. Furthermore, we make predictions for the observables such as relative energy spectra of the valence neutron-core fragments, parallel momentum distribution of the core fragment, and the angular distribution of the valence neutron as a function of deformation. Our study is expected to provide more understanding about the evolution of the shell structure in island of inversion from $N = 20$ to 28, about which some conflicting results have been reported recently [22, 23]. Furthermore, our study is expected to quantify the presence of a neutron halo structure in ^{37}Mg and provide information about its correlation to the ground state deformation of this nucleus.

The study of Coulomb break-up of ^{37}Mg is also of interest in astrophysics because it provides an indirect way to determine the rate of the radiative neutron capture reaction ^{36}Mg$(n, \gamma)^{37}$Mg, which is of importance in the study of the r-process nucleosynthesis in supernovae [24].

3.3   Formalism : Finite range distorted Born approximation with deformed projectile

Reduced T-matrix, $\hat{\ell}\beta_{\ell m}$ using Eq. (2.27) from chapter 2, can be written as

$$
\begin{aligned}
\hat{\ell}\beta_{\ell m} = &\int d\mathbf{r}_i e^{-i\delta\mathbf{k}_n \cdot \mathbf{r}_i} \chi_b^{(-)*}(\mathbf{k}_b, \mathbf{r}_i) \chi_a^{(+)}(\mathbf{k}_a, \mathbf{r}_i) \\
&\times \int d\mathbf{r}_1 e^{-i\mathbf{Q}\cdot\mathbf{r}_1} V_{bn}(\mathbf{r}_1) u_\ell(r_1) Y_\ell^m(\hat{\mathbf{r}}_1),
\end{aligned} \tag{3.1}
$$

These two parts namely dynamic part, I_d and structure part, I_f can be solved analytically as explained in chapter 2. For a deformed nuclei, the interaction between should be incorporated with these deformations.

We now introduce deformation in potential $V_{bn}(\mathbf{r}_1)$ in Eq. (3.1). Following [25], we write the axially symmetric quadrupole-deformed Woods-Saxon potential (without taking the spin-orbit term) as

$$V_{bn}(\mathbf{r}_1) = V_{ws}(r_1) - \beta_2 k(r_1) Y_2^0(\hat{\mathbf{r}}_1). \tag{3.2}$$

We take the Woods-Saxon form for the potential $V_{ws}(r_1)$, and write, $V_{ws}(r_1) = V_{ws}^0 f(r_1)$, where V_{ws}^0 is the depth of the potential and $f(r_1)$ describes its shape. $f(r_1)$ and $k(r_1)$ are defined as

$$f(r_1) = \frac{1}{1 + exp(\frac{r_1 - R}{a})}, \quad k(r_1) = RV_{ws}^0 \frac{df(r_1)}{dr_1},$$

with radius $R = r_0 A^{1/3}$ where r_0 and a are the radius and diffuseness parameters, respectively. β_2 is the quadrupole deformation parameter. In Eq. (3.2), we have included only the lowest-order term in the deformation parameter of the deformed Woods-Saxon potential (see, e.g., Ref. [26]). This is an approximation. However, this should be sufficient for our purpose of illustrating the role of projectile deformation effects on the breakp cross-sections.

The radial wavefunction corresponding to the potential $V_{bn}(\mathbf{r}_1)$ should be obtained by solving the coupled equation

$$\left\{ \frac{d^2}{dr_1^2} - \frac{\ell(\ell+1)}{r_1^2} + \frac{2\mu}{\hbar^2}[E - V_{ws}(r_1)] \right\} u_{\ell m}(r_1)$$
$$= \frac{2\mu}{\hbar^2} \sum_{\ell'} \langle Y_\ell^m(\hat{\mathbf{r}}_1)| - \beta_2 k(r_1) Y_2^0(\hat{\mathbf{r}}_1) | Y_{\ell'}^m(\hat{\mathbf{r}}_1) \rangle u_{\ell' m}(r_1). \tag{3.3}$$

Therefore, the radial wavefunctions obtained from Eq. (3.3), corresponding to a given ℓ will have an admixture of wavefunctions corresponding to other ℓ values

of the same parity. Thus this wavefunction can be quite different from that of the spherical Woods-saxon potential. However, if components of the admixed states of higher ℓ are quite weak, then the pure states of lowest ℓ can become dominant. In such a situation, one can use the solutions of the spherical Woods-Saxon potential corresponding to a single ℓ for the wavefunction $u_\ell(r_1)$ in Eq. (3.1). Indeed, it has been shown in Ref. [25] that as the binding energies approach zero, the lowest ℓ components become dominant in the neutron orbits of the realistic deformed potential irrespective of the size of the deformation. In this work, we have made the approximation of taking $u_\ell(r_1)$ as the state of a given single ℓ value that is the solution of the Schrödinger equation with spherical Woods-Saxon potential. In any case, if the spectroscopic factors of shell model calculations are used for a particular state, the wavefunctions obtained in a spherical basis for that state should already include the admixture of different ℓ states.

We would like to point out here that only the structure part of the amplitude given by Eq. (3.1) is affected by the deformation in the interaction $V_{bn}(\mathbf{r}_1)$ - the dynamical part of it remains the same as it would be in no-deformation case. With the deformation effects introduced through Eq. (3.2), analytic expressions can be written for the structure part of the amplitude in Eq. (3.1). Let us define

$$I_f = \int \mathbf{dr}_1 e^{-i\mathbf{Q}\cdot\mathbf{r}_1} V_{bn}(\mathbf{r}_1) u_\ell(r_1) Y_\ell^m(\hat{\mathbf{r}}_1). \tag{3.4}$$

$$
\begin{aligned}
I_f = {}& 4\pi \sum_{l_1 m_1} i^{-l_1} Y_{l_1}^{m_1}(\hat{\mathbf{Q}}) \int r_1^2 dr_1 j_{l_1}(Qr_1) \\
& \times \int d\Omega_{r_1} \left[V_{ws}(r_1) - \beta_2 R V_{ws}^0 Y_2^0(\hat{\mathbf{r}}_1) \frac{df(r_1)}{dr_1} \right] Y_{l_1}^{m_1*}(\hat{\mathbf{r}}_1) Y_\ell^m(\hat{\mathbf{r}}_1) u_\ell(r_1) \\
= {}& 4\pi \sum_{l_1 m_1} i^{-l_1} Y_{l_1}^{m_1}(\hat{\mathbf{Q}}) \int r_1^2 dr_1 j_{l_1}(Qr_1) u_\ell(r_1) \\
& \times \left[\int d\Omega_{r_1} V_{ws}(r_1) Y_{l_1}^{m_1*}(\hat{\mathbf{r}}_1) Y_\ell^m(\hat{\mathbf{r}}_1) - \int d\Omega_{r_1} \beta_2 R V_{ws}^0 \frac{df(r_1)}{dr_1} Y_2^0(\hat{\mathbf{r}}_1) Y_{l_1}^{m_1*}(\hat{\mathbf{r}}_1) Y_\ell^m(\hat{\mathbf{r}}_1) \right].
\end{aligned}
\tag{3.5}
$$

Simplifying further

$$I_f = 4\pi \sum_{l_1 m_1} i^{-l_1} Y_{l_1}^{m_1}(\hat{\mathbf{Q}}) \int r_1^2 dr_1 j_{l_1}(Qr_1) u_\ell(r_1)$$

$$\times \left[V_{ws}(r_1)\delta_{l_1,\ell}\delta_{m_1,m} - \beta_2 R V_{ws}^0 \frac{df(r_1)}{dr_1} \int d\Omega_{r_1} Y_2^0(\hat{\mathbf{r}}_1) Y_{l_1}^{m_1*}(\hat{\mathbf{r}}_1) Y_\ell^m(\hat{\mathbf{r}}_1) \right]. \quad (3.6)$$

In this equation first part is simple spherical potential as we solved earlier. For solving second part,

$$I_f = 4\pi \sum_{l_1 m_1} i^{-l_1} Y_{l_1}^{m_1}(\hat{\mathbf{Q}}) \int r_1^2 dr_1 j_{l_1}(Qr_1) u_\ell(r_1)$$

$$\times \left[V_{ws}(r_1)\delta_{l_1,\ell}\delta_{m_1,m} - \beta_2 R V_{ws}^0 \frac{df(r_1)}{dr_1} I_1 \right], \quad (3.7)$$

where I_1 is defined as

$$I_1 = \int d\Omega_{r_1} Y_2^0(\hat{\mathbf{r}}_1) Y_{l_1}^{m_1*}(\hat{\mathbf{r}}_1) Y_\ell^m(\hat{\mathbf{r}}_1) = (-1)^{m_1} \sqrt{\frac{5}{4\pi}} \left[\frac{(2\ell+1)(2l_1+1)}{4\pi} \right]^{1/2}$$

$$\times \begin{pmatrix} l_1 & 2 & \ell \\ 0 & 0 & 0 \end{pmatrix} \begin{pmatrix} l_1 & 2 & \ell \\ -m_1 & 0 & m \end{pmatrix}, \quad (3.8)$$

with $|\ell - 2| < l_1 < |\ell + 2|$ and $m_1 = m$. Notice that there would be a limited number of l_1 values to be considered, given that ℓ is the orbital angular momentum of the projectile ground state. In the limit of $\beta_2 = 0$, the above equation would contain the first term in the square bracket [involving the spherical potential $V_{ws}(r_1)$] that is reduced precisely in the same form as that obtained in Ref. [27] for the case where there is no deformation.

In Eq. (3.7), the spherical harmonic $Y_{l_1}^{m_1*}(\hat{\mathbf{Q}})$ (where $\mathbf{Q} = \gamma\mathbf{q_n} - \alpha\mathbf{K}$) can be written in terms of product of two spherical harmonics, one depending on $\hat{\mathbf{q}}_n$ and

the other depending on $\hat{\mathbf{K}}$, using Moshinsky's formula [28]:

$$(|\mathbf{Q}|)^{l_1} Y_{l_1}^{m_1}(\hat{\mathbf{Q}}) = \sum_{LM_L} \frac{\sqrt{4\pi}}{\hat{L}} \begin{pmatrix} 2l_1 + 1 \\ 2L \end{pmatrix}^{1/2} |\alpha K|^{l_1 - L} (\gamma q_n)^L$$

$$\times \langle l_1 - L \ m_1 - M_L \ L \ M_L | l_1 \ m_1 \rangle Y_{l_1-L}^{m_1-M}(\hat{\mathbf{K}}) Y_L^M(\hat{\mathbf{q}}_n),$$

(3.9)

where $\begin{pmatrix} 2l_1 + 1 \\ 2L \end{pmatrix}$ is the binomial coefficient and $\hat{L} = \sqrt{2L+1}$ with L varying from 0 to l_1. Therefore, the structure part Eq. (3.7), can be evaluated and would contain the effect of the deformation of the projectile.

We once again wish to emphasize the analytic nature of our calculation at this point. With the structure part given by Eq. (3.7), the dynamics part in Eq. (3.1) is still given by the Bremsstrahlung integral [29], which can be solved analytically. Various reaction observables can be calculated as explained in chapter 2.

3.4   Results and discussions

The formalism described in Section 3.2, has been employed to investigate Coulomb break-up of ^{37}Mg on a Pb target at the beam energy of 244 MeV/nucleon. In our analysis the calculated one-neutron removal cross-sections are compared with the corresponding data as reported in Ref. [2]. To calculate the Coulomb break-up amplitude [see, Eq. (3.1)], we require the single-particle wavefunction $u_\ell(r)$ that describes the core-valence neutron relative motion in the ground state of the projectile (for a given neutron-core configuration). As discussed in the previous section, we take this wavefunction as that of a state of a single ℓ value and obtain it by solving the Schrödinger equation with a spherical Woods-Saxon potential with radius (r_0) and diffuseness (a) parameters of 1.24 fm and 0.62 fm, respectively. The depth of this well is adjusted to reproduce the valence neutron separation energy corresponding

to this state.

Table 3.1: Depth (V_{ws}^0) of the Woods-Saxon potential well as a function of S_n corresponding to neutron removal from the $2p_{3/2}$, $2s_{1/2}$, $1f_{7/2}$ orbitals. The values of parameters r_0 and a are taken to be 1.24 fm and 0.62 fm, respectively in all the cases.

S_n (MeV)	V_{ws}^0 $(2p_{3/2})$ (MeV)	V_{ws}^0 $(2s_{1/2})$ (MeV)	V_{ws}^0 $(1f_{7/2})$ (MeV)
0.01	43.97	24.73	43.36
0.05	44.18	25.28	43.43
0.10	44.42	25.72	43.53
0.15	44.64	26.06	43.62
0.20	44.84	26.36	43.71
0.22	44.92	26.47	43.75
0.25	45.04	26.63	43.81
0.30	45.23	26.88	43.90
0.35	45.42	27.11	43.99
0.40	45.60	27.33	44.09
0.45	45.77	27.53	44.18
0.50	45.94	27.73	44.27
0.55	46.11	27.92	44.37
0.60	46.28	28.11	44.46
0.65	46.44	28.29	44.55
0.70	46.60	28.46	44.64

Various observables for the reaction have been obtained by integrating the triple differential cross-sections [see, Eq. (2.40) of chapter 2] over appropriate angles and energies of the unobserved quantity. For example, the total Coulomb one-nucleon removal cross-section for a given ℓj configuration of the valence neutron is obtained by integrating the triple differential cross-sections over angles and energy of fragment b and angles of the valence neutron n.
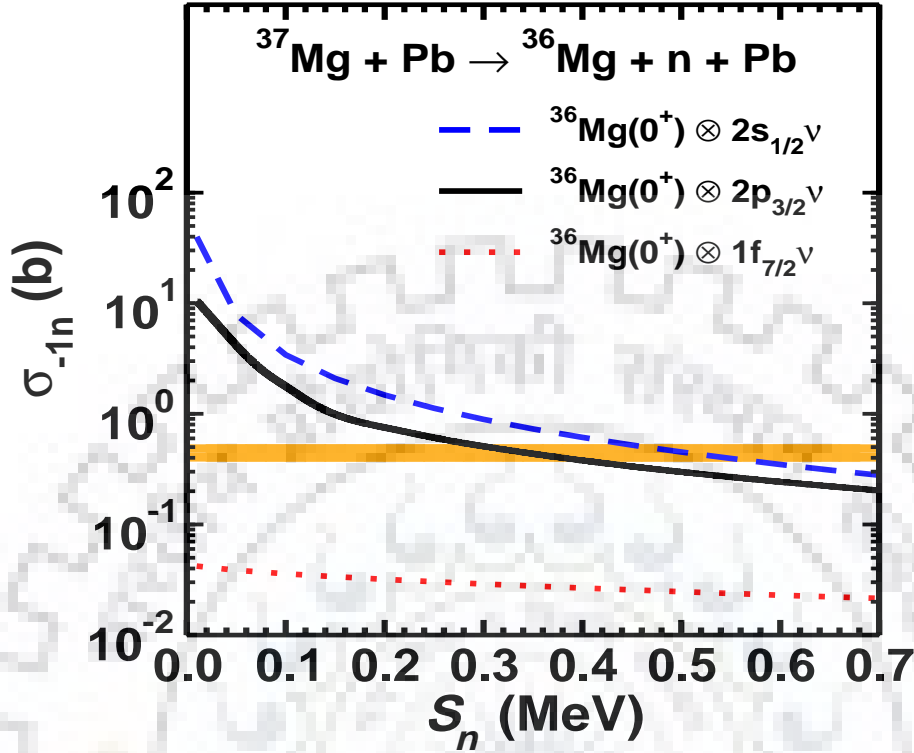
Figure 3.1: Pure Coulomb total one-neutron removal cross-section, σ_{-1n}, in the break-up reaction of ^{37}Mg on a Pb target at 244 MeV/nucleon beam energy as a function of one-neutron separation energy S_n obtained with configurations ^{36}Mg(0^+) $\otimes$ $2p_{3/2}\nu$ (solid line), ^{36}Mg(0^+) $\otimes$ $2s_{1/2}\nu$ (dashed line) and ^{36}Mg(0^+) $\otimes$ $1f_{7/2}\nu$ (dotted line) for ^{37}Mg$_{gs}$ using the spectroscopic factors (C^2S) 1.0 in each case. The experimental cross-section (taken from Ref. [2]) is shown by the shaded band.

The nuclei in island of inversion are expected to have significant components of $2p - 2h$ $[\nu(sd)^{-2}(fp)^2]$ neutron intruder configurations. Indeed, in Ref. [2], it has been argued that the valence neutron in ^{37}Mg$_{gs}$ is most likely to have a spin parity (J^π) of $3/2^-$ that corresponds to the $2p_{3/2}$ orbital. In this work, we have considered neutron removal from the $2p_{3/2}$, $2s_{1/2}$ and $1f_{7/2}$ orbitals that correspond to ^{37}Mg ground state J^π of $3/2^-$, $1/2^+$, and $7/2^-$, respectively. Since the S_n of the valence neutron in the ^{37}Mg ground state is still uncertain, we show in Table 3.1, values of the depths of the potential well as a function of S_n for all of the three orbitals.

In Figure 3.1, we present the results of our calculations for the pure Coulomb σ_{-1n} in the break-up reaction of ^{37}Mg on a Pb target at the beam energy of 244 MeV/nucleon as a function of S_n corresponding to the one-neutron removal from the $2p_{3/2}$, $2s_{1/2}$ and $1f_{7/2}$ orbitals. For C^2S we have used a uniform value of one for each configuration. The shaded band in this figure shows the corresponding measured cross-section taken from Ref. [2] with its width representing the experimental uncertainty. We note that calculated cross-sections obtained with the ^{36}Mg$(0^+) \otimes 2p_{3/2}\nu$ and ^{36}Mg$(0^+) \otimes 2s_{1/2}\nu$ configurations (solid and dashed lines, respectively in Fig. 3.1) overlap with the experimental band in the S_n regions of 0.35 ± 0.06 MeV and 0.50 ± 0.07 MeV, respectively. Theoretical cross-sections for the $2p_{1/2}$ case are almost identical to those of the $2p_{3/2}$ case. On the other hand, for the ^{36}Mg$(0^+) \otimes 1f_{7/2}\nu$ configuration there is no overlap between calculated and experimental cross-sections anywhere, which excludes the assignment of $J^\pi = 7/2^-$ to ^{37}Mg$_{gs}$. Therefore, our results are consistent with the assignment of either of the $3/2^-$ and $1/2^+$ spin parity to the ground state of ^{37}Mg with one-neutron separation energies in the ranges as stated above. The S_n deduced in our work for either of these configurations is within the range of the evaluated value of 0.16 ± 0.68 MeV as reported in the most recent nuclear mass tabulation [21].

Nevertheless, it should be noted that there is a wide variation in the C^2S values for these states reported in the literature. For ^{36}Mg$(0^+) \otimes 2p_{3/2}\nu$ and ^{36}Mg$(0^+) \otimes 2s_{1/2}\nu$ configurations, while the shell model C^2S values are reported to be 0.31 and 0.001, respectively [9], values extracted from an analysis of the ^{37}Mg break-up data [2] are $0.42^{+0.14}_{-0.12}$ and $0.40^{+0.16}_{-0.13}$, respectively. In the latter work the theoretical cross-sections have been computed from the eikonal model of Ref. [30] for the C target and from the (semiclassical) Coulomb break-up model of Ref. [31] for the Pb target. On the other hand, for the ^{36}Mg$(0^+) \otimes 1f_{7/2}\nu$ configuration the C^2S is not mentioned in these references. For a given neutron-core configuration S_n extracted from the Coulomb break-up data is intimately related to the value of C^2S. Therefore, it would be interesting to investigate the C^2S dependence of S_n extracted in our

study.
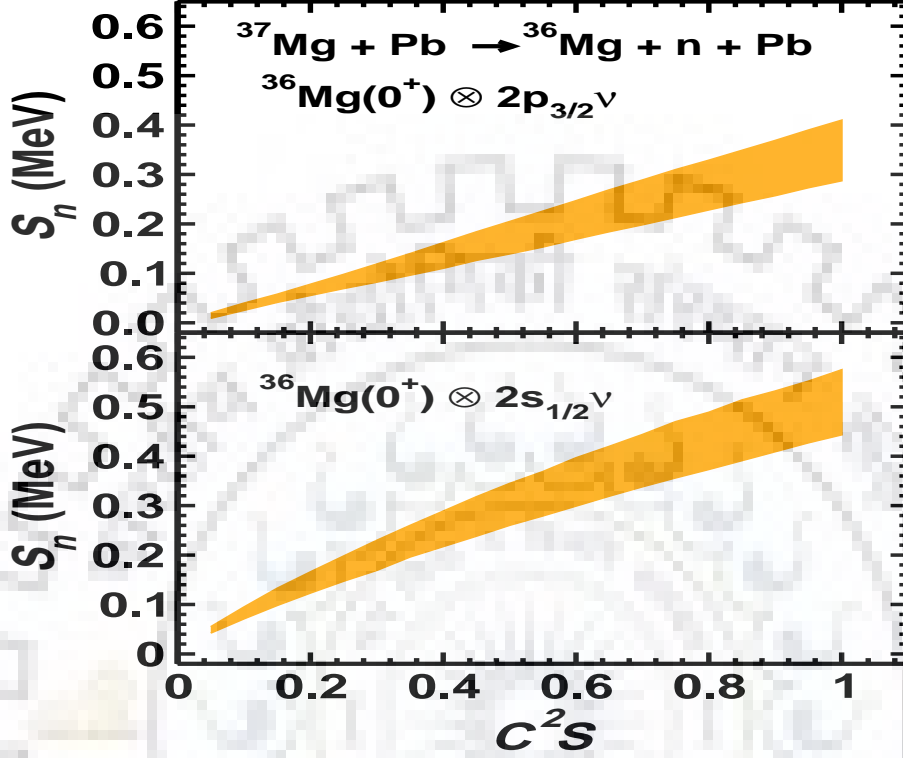
Figure 3.2: (upper) S_n as a function of C^2S for the same reaction as in Fig. 3.1 with the ^{37}Mg$_{gs}$ configuration of ^{36}Mg$(0^+) \otimes 2p_{3/2}\nu$, (lower) same as in (upper) for the ^{36}Mg$(0^+) \otimes 2s_{1/2}\nu$ configuration

In Figs. 3.2(upper) and 3.2(lower), we show this correlation for the same reaction as in Fig. 3.1 for the configurations ^{36}Mg$(0^+) \otimes 2p_{3/2}\nu$ and ^{36}Mg$(0^+) \otimes 2s_{1/2}\nu$ of the ^{37}Mg$_{gs}$, respectively. In these calculations, for each C^2S the corresponding S_n is deduced from the region of overlap of the calculated cross-section and the measured data band as shown in Fig. 3.1. We see that S_n increases steadily with increasing C^2S. Also the uncertainty in the extracted S_n increases with C^2S, because at larger C^2S flatter portions of the calculated cross-section overlap with the data band that encompasses larger parts of the band. It may be mentioned here that in our calculations S_n corresponding to the C^2S of 0.42 for the configuration ^{36}Mg$(0^+) \otimes 2p_{3/2}\nu$, is 0.14 ± 0.03 MeV, which is lower than the mean value of S_n (0.22 MeV) obtained in Ref. [2] for the same C^2S. It is clear from this figure that for a reliable

extraction of S_n from the Coulomb break-up studies, it is essential to have accurate knowledge of the spectroscopic factors for different configurations.
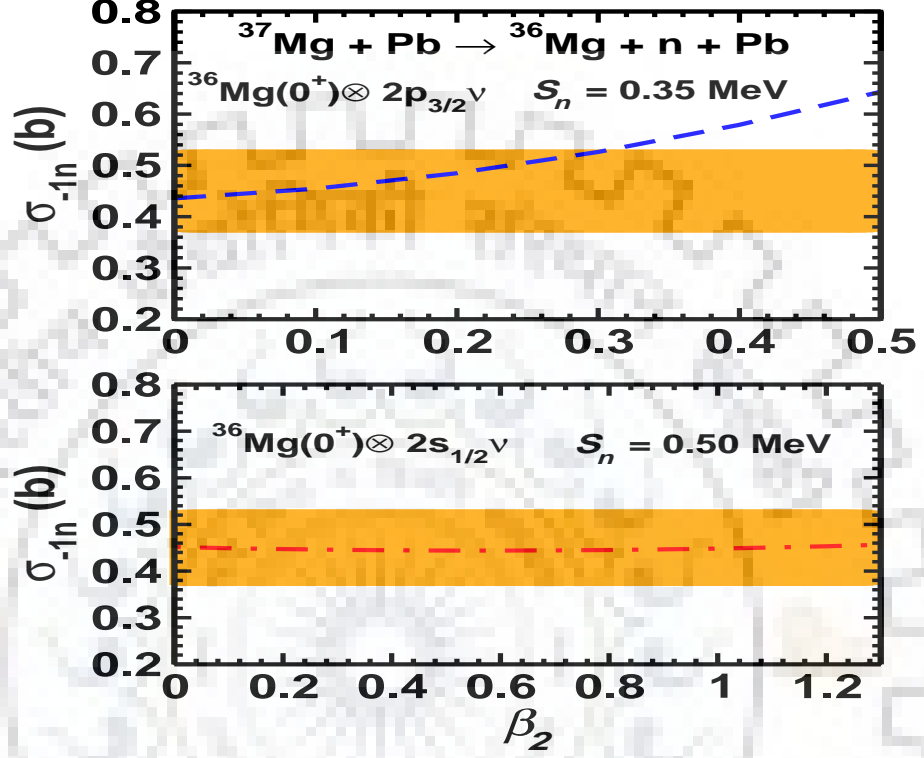
Figure 3.3: (upper)σ_{-1n} as a function of the deformation parameter β_2 in the Coulomb break-up of ^{37}Mg on a Pb target at the beam energy of 244 MeV/nucleon with the configuration ^{36}Mg$(0^+) \otimes 2p_{3/2}\nu$ for ^{37}Mg$_{gs}$. The S_n is taken to be 0.35 MeV with C^2S values being 1.0. (lower) Same as in Fig. (upper) for ^{36}Mg$(0^+) \otimes 2s_{1/2}\nu$ configuration with C^2S and S_n of 1.0 and 0.50 MeV, respectively. In both (upper) and (lower) the experimental data (shown by the shaded region) are taken from Ref. [2].

To substantiate the information extracted from the studies of the one-neutron removal cross-section, it is desirable to investigate other effects and observables to determine the most reliable configuration of ^{37}Mg$_{gs}$ to this end,in Figs. 3.3(upper) and 3.3(lower) we investigate the effect of projectile deformation on σ_{-1n} for the reaction studied in Fig. 3.1. As discussed earlier, the presence of neutrons in nearby degenerate j shells (eg., $1f_{7/2}$ and $2p_{3/2}$) in ^{37}Mg that couple strongly to each other by the quadrupole-quadrupole interaction, can lead to the quadrupole deformation of this nucleus.

In Fig. 3.3(upper), we show our results for σ_{-1n} as a function of β_2 for the ^{36}Mg$(0^+) \otimes 2p_{3/2}\nu$ configuration of ^{37}Mg$_{gs}$ with C^2S values of 1.0 corresponding to a S_n of 0.35, which is the mean value of the one-neutron separation energies extracted from the comparison of the calculated and experimental total cross-sections in Fig. 3.1. For $\beta_2 = 0$, the σ_{-1n} is the same as that shown in Fig. 3.1 for the same value of S_n. With increasing β_2, the cross-section increases, and the overlap between calculations and the data band ceases for $\beta_2 > 0.32$. Therefore, our calculations do not support a quadrupole deformation parameter in excess of 0.32 for this state.

In Fig. 3.3(lower) we show the same results for the ^{36}Mg$(0^+) \otimes 2s_{1/2}\nu$ configuration with C^2S and S_n values of 1.0 and 0.50 MeV, respectively, The contribution of the deformation term to the cross-section is substantially low for the s-wave configuration, which results in almost constant σ_{-1n} as a function of β_2 as seen in Fig. 3.3(lower). We further note that in contrast to the results in Fig. 3.3(upper), the overlap between calculated cross sections and the data band exists even for values of β_2 as high as 1.2. We have checked that the situation remains the same for β_2 values even beyond 1.2. This result indicates that the s-wave configuration does not provide any constraint on the deformation parameter β_2 in our calculations. On the other hand, the Nilsson model study of Ref. [12] predicts the β_2 parameter of the $2s_{1/2}$ state to be below 0.3. This, however, does not imply that the s-wave configuration is negated for the ground state of ^{37}Mg in our calculations. It simply does not constrain the β_2 value for this state. In any case, it is not possible to obtain more definite constraints on the configuration of ^{37}Mg$_{gs}$ from a single measurement as available at present.
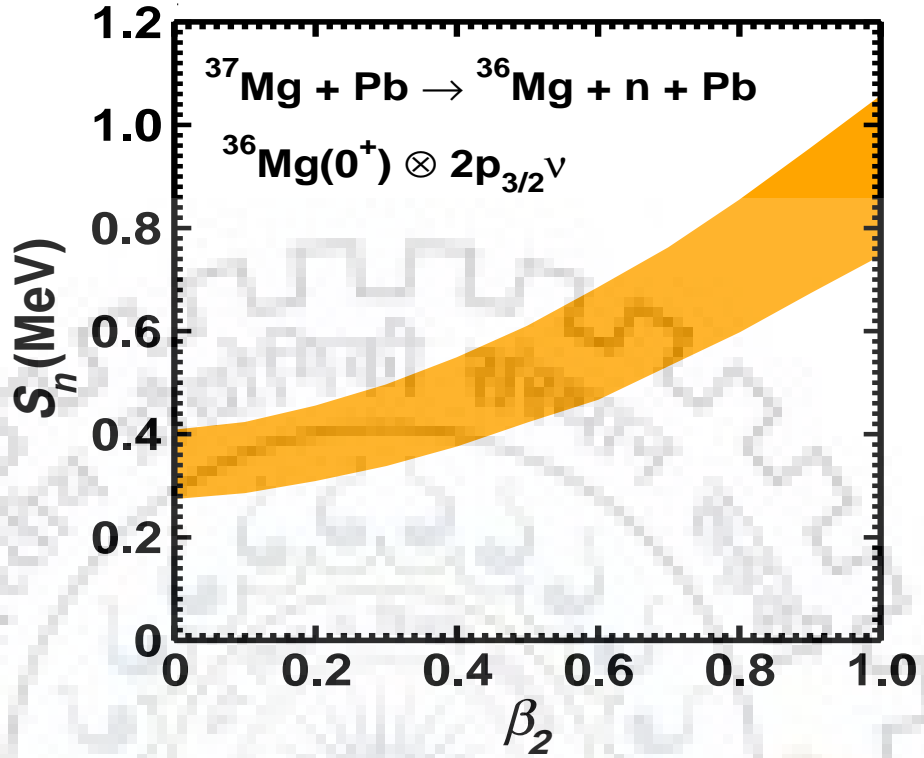
Figure 3.4: S_n deduced from the comparison of our calculations with the experimental data as a function of the parameter β_2 for the same reaction as in Fig. **3.3**(upper), corresponding to the $^{36}\mathrm{Mg}(0^+) \otimes 2p_{3/2}\nu$ configuration of $^{37}\mathrm{Mg}_{gs}$ with $C^2S = 1.0$.

The variation of S_n with the deformation parameter β_2 is studied in Fig. 3.4 for the same reaction as in Fig. 3.3(upper) for the $^{37}\mathrm{Mg}_{gs}$ configuration of $^{36}\mathrm{Mg}(0^+) \otimes 2p_{3/2}\nu$ with C^2S value of one. Several authors have argued that the deformation can lead to the enhancement of binding energies in the island of inversion region nuclei [3, 32–34] due to the mixing of $2\hbar\omega$ $2p-2h$ neutron excitations to $0\hbar\omega$ states. We notice in this figures that S_n indeed increases with β_2. For $\beta_2 > 0.70$, the S_n value exceeds the upper limit of that evaluated in Ref. [21]. Therefore, for the p-wave configuration of the $^{37}\mathrm{Mg}_{gs}$, the deformation parameter remains reasonable even for maximum predicted S_n. On the other hand, with the $^{36}\mathrm{Mg}(0^+) \otimes 2s_{1/2}\nu$ configuration, the S_n remains unchanged with β_2, which is obvious from Fig.3.3(lower).

The investigation of more exclusive observables in the Coulomb break-up reactions of the projectile provides significant advantages in the understanding of its
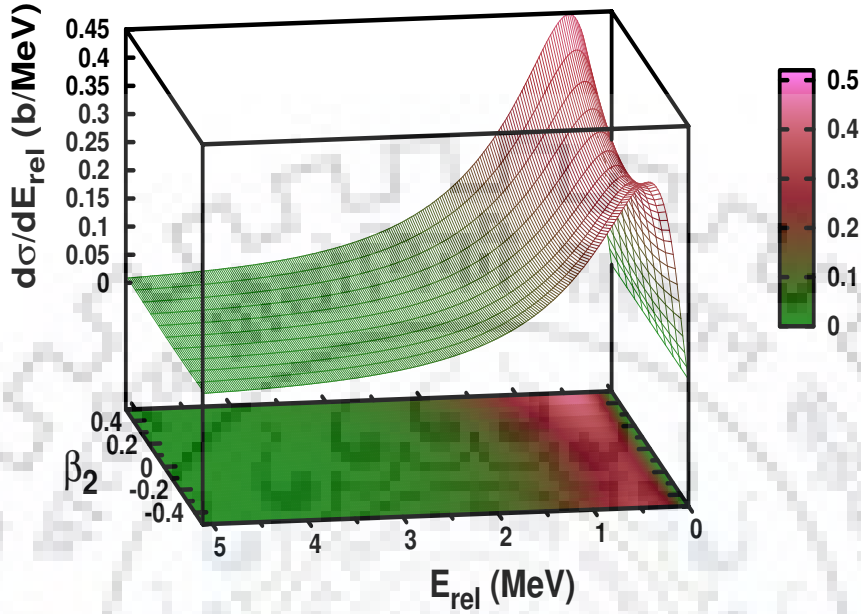
Figure 3.5: Relative energy spectra for the Coulomb break-up of ^{37}Mg($J^\pi = 3/2^-$) on a Pb target at 244 MeV/nucleon beam energy, calculated for different values of β_2 with $C^2S = 1.0$ and $S_n = 0.35$ MeV.

ground state structure. In Fig. 3.5, we show the ^{36}Mg$-n$ relative energy spectra in Coulomb breakup of ^{37}Mg on a Pb target at the beam energy of 244 MeV/nucleon as a function of the ^{36}Mg$-n$ relative energy (E_{rel}) and β_2 simultaneously. The ^{37}Mg$_{gs}$ configuration is ^{36}Mg(0^+) $\otimes$ $2p_{3/2}\nu$ with C^2S and S_n values of 1.0 and 0.35 MeV, respectively. We note that the height of the peak depends on the value of β_2. The position of the peak in this spectrum is dependent on the configuration of the projectile ground state, which is made more explicit in the next figure.

In Fig. 3.6, we show the relative energy spectra ($d\sigma/dE_{rel}$) as a function of E_{rel} for the same reaction as in Fig. 3.1 for two different configurations of ^{37}Mg ground state as indicated in the figure. Since, the peak position of $d\sigma/dE_{rel}$ is known to depend on the value of S_n [35–41], we have used the same values of S_n and C^2S (0.35 MeV and 1.0, respectively), for the two configurations. This ensures that differences seen in
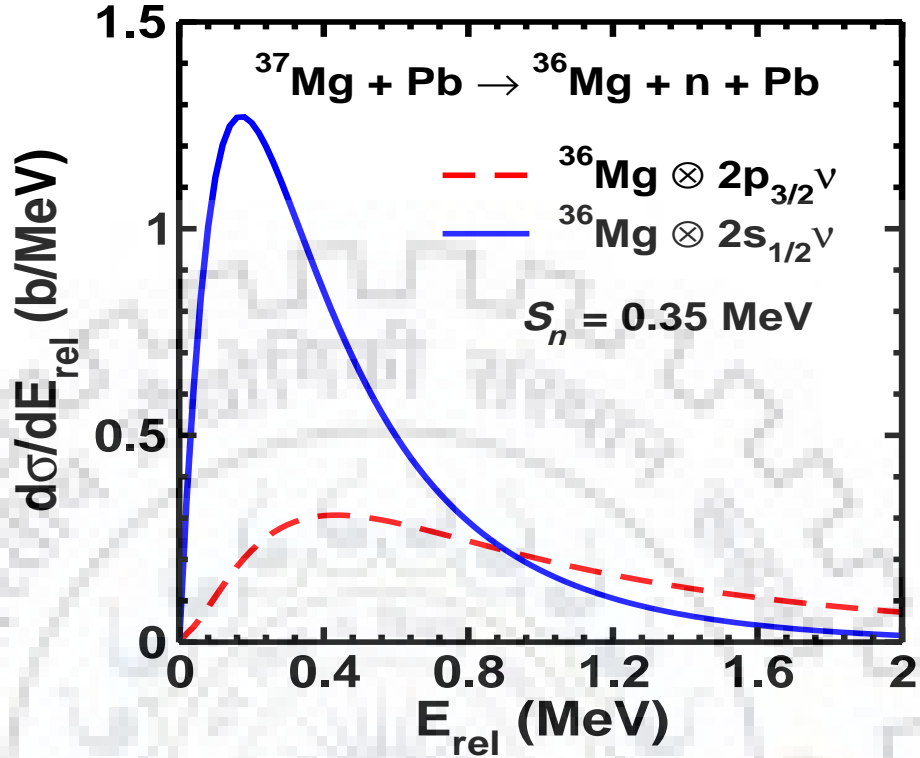
Figure 3.6: Comparison of relative energy spectra for the Coulomb break-up of ^{37}Mg on Pb target at 244 MeV/nucleon beam energy corresponding to two different possible ground state configurations, ^{36}Mg(0^+)$\otimes 2p_{3/2}\nu$ (dashed line) and ^{36}Mg(0^+)$\otimes 2s_{1/2}\nu$ (solid line). The values of S_n and C^2S are 0.35 MeV and 1.0, respectively for both the configurations. No deformation of the projectile has been included in these calculations.

the relative energy differential cross-sections of the two configurations are attributed solely to the differences in the projectile ground state structure. We see that the relative energy spectra obtained with two configurations show drastically different behavior as a function of E_{rel}. With the s-wave configuration, the magnitude of the cross-section near the peak position is more than 3 times larger than that obtained with the p-wave one. Even the peak position of the two configuration are at different values of E_{rel} - the p-wave cross-sections peak at higher E_{rel} as compared to those of the s-wave.

In view of the results shown in Fig. 3.6 measurements of the relative energy spectra in the break-up reactions of ^{37}Mg would be of great help in reducing the uncertainty in its ground state configuration and also in its one-neutron separa-
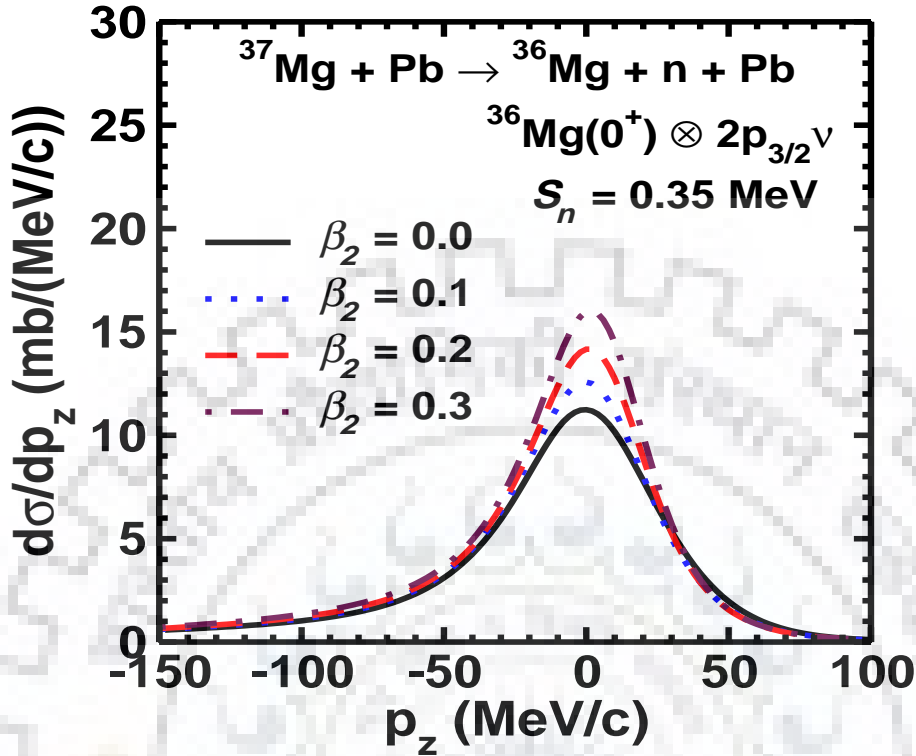
Figure 3.7: Parallel momentum distribution of ^{36}Mg fragment in the Coulomb break-up of ^{37}Mg on Pb target at 244 MeV/nucleon beam energy for the $J^{\pi} = 3/2^-$ configuration of ^{37}Mg$_{gs}$ with $S_n = 0.35$ MeV and C^2S of 1.0.

tion energy. Fixing of these quantities will lead to a better understanding of the quadrupole deformation of this nucleus, which also affects the height of the peak in the relative energy spectra. In Fig. 3.7, we show the parallel momentum distribution (PMD) of the core fragment ^{36}Mg in the Coulomb break-up reaction ^{37}Mg + Pb $\rightarrow$ ^{36}Mg + n + Pb at the beam energy of 244 MeV/nucleon. ^{37}Mg$_{gs}$ was assumed to have the ^{36}Mg$(0^+) \otimes 2p_{3/2}\nu$ configuration with S_n and C^2S being 0.35 MeV and 1.0, respectively. Results are shown for several values of the β_2 parameter. We note that the magnitude of the cross-section near the peak position is quite sensitive to the β_2 value. Therefore, measurement of this observable is a useful tool for putting constraints on the degree of the quadrupole deformation in ^{37}Mg.

We note from Table 3.2 that the full width at half maximum (FWHM) of the PMD are almost the same for $\beta_2 \geq 0.30$ (44.0 MeV/c). Even for $\beta_2 = 0.0$, the

Table 3.2: Full width at half maximum of the parallel momentum distribution of ^{36}Mg, obtained in Coulomb break-up of ^{37}Mg on a Pb target at the beam energy of 244 MeV/nucleon. The projectile ground state corresponds to the configuration of ^{36}Mg(0^+) $\otimes 2p_{3/2}\nu$ with S_n and C^2S values of 0.35 MeV and 1.0, respectively.

S_n (MeV)	β_2	FWHM (MeV/c)
	0.0	54.65
	0.1	50.97
0.35	0.2	48.03
	0.3	45.82
	0.4	44.85
	0.5	44.61

FWHM is only about 15% larger than its value at higher β_2. This is very close to the FWHM of the PMD of the core fragment seen in the break-up reactions of the established low mass halo nuclei like ^{11}Be and ^{19}C. Therefore, the p-wave ($J^\pi = 3/2^-$) ground state of ^{37}Mg is highly likely to have a halo structure.

In Fig. 3.8 we show a detailed dependence of FWHM of the PMD on the one-neutron separation energy, S_n, for various values of the deformation parameter β_2. The reactions is the same as that studied in Fig. reff4.8 with same value of C^2S. We note that regardless of the value of β_2 the FWHM increases with increasing S_n. This is expected because with increasing binding energy the neutron orbits tend to become more and more like those of the nuclei away from the drip line. Furthermore, for most values of S_n, the β_2 dependence of the not of the PMD is similar to that shown in Table 3.2.

In Fig. 3.9(a) we show the double differential cross-section $d^2\sigma/dE_n d\Omega_n$ as a function of the neutron energy for three neutron angles between $1° - 3°$. The configuration of ^{37}Mg$_{gs}$, and C^2S and S_n values were the same as those in Fig. 4.8. No deformation of the projectile was considered in these calculations (that is β_2 = 0). We see that magnitude of the cross-section near the peak position reduces with increasing neutron angle. An interesting observation is that for all the three angles, the peak occurs near the neutron energy that correspond to the beam veloc-
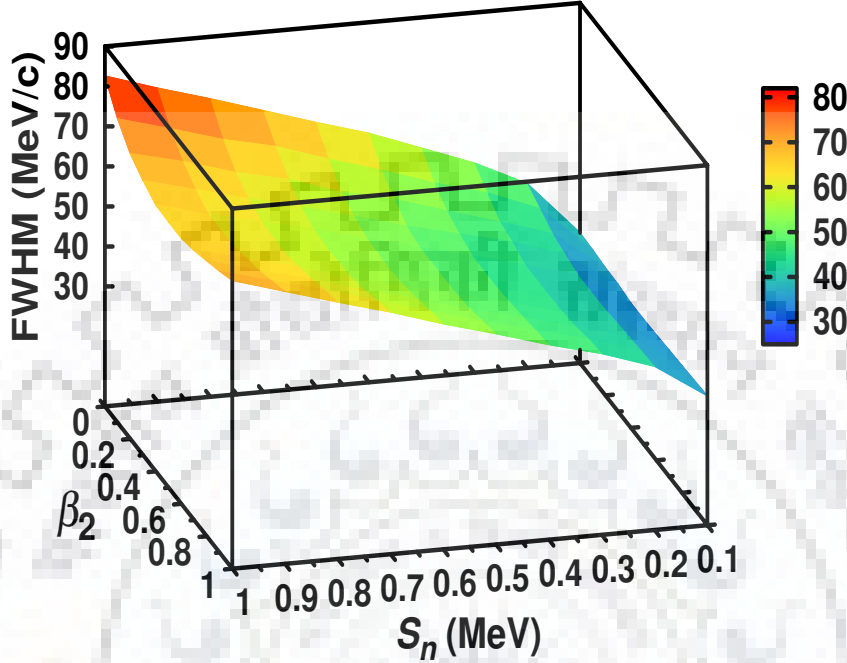
Figure 3.8: Full width at half maximum of the parallel momentum distribution of ^{36}Mg, obtained in Coulomb break-up of ^{37}Mg on a Pb target at the beam energy of 244 MeV/nucleon as a function of the one-neutron separation energy S_n and the quadrupole deformation parameter β_2. The projectile ground state corresponds to the configuration of ^{36}Mg$(0^+) \otimes 2p_{3/2}\nu$ with a C^2S value of 1.0.

ity. This is consistent with the picture that fragments move with the beam velocity after the break-up. If the charged fragment gets post-accelerated as it leaves the reaction zone (which is the case for the break-up reactions of stable nuclei [42, 43]), one would expect the position of the peak in the neutron spectrum at energies below that corresponding to the beam velocity. We do not see this post-acceleration effect even if Coulomb effects have been included to all orders in the incoming and outgoing channels in our theory. Due to very small binding energies of the halo nuclei and the reactions at higher beam energies, the break-up occurs at distances much larger than the distance of closest approach, thus the post-acceleration effects are minimal [44–46].

The effect of projectile deformation on the cross-section $d^2\sigma/dE_n d\Omega_n$ is studied
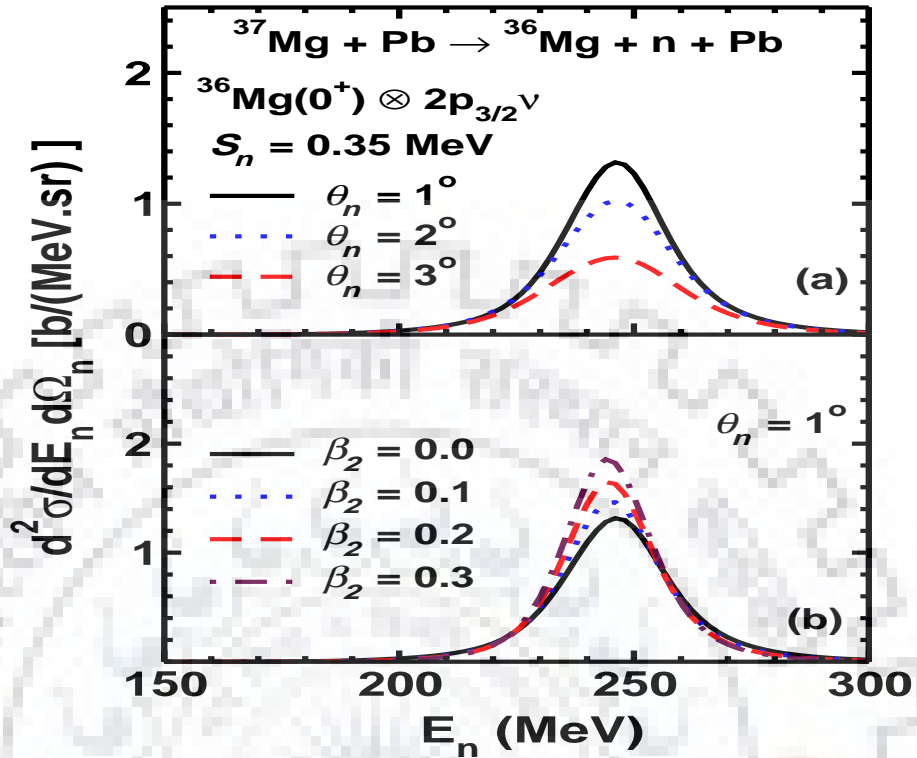
Figure 3.9: Neutron energy-angular distribution for the Coulomb break-up of ^{37}Mg on a Pb target at 244 MeV/nucleon beam energy calculated for $S_n = 0.35$ MeV and $C^2S = 1.0$ for the projectile ground state configuration corresponding to $J^\pi = 3/2^-$ for (a) (θ_n) at $1°$, $2°$ and $3°$, and (b) with different values of β_2 for $\theta_n = 1°$,

in Fig. 3.9(b) for the same reaction as in Fig. 3.9(a) for one angle of $\theta_n = 1°$. It is evident from this figure that magnitude of the cross-section increases with β_2. This is most visible near the peak position. Therefore, measurements of the double differential cross-sections are expected to provide additional information about the deformation of the projectile ground state.

The angular distributions of neutrons emitted in the projectile break-up reactions reflect to a great extent the momentum distribution of the fragments in the ground state of the projectile (see, e.g., Ref. [47]). Therefore, their study is expected to provide further information about the neutron halo structure in ^{37}Mg. In Fig. 3.10, we show the neutron angular distribution in the Coulomb break-up reaction ^{37}Mg + Pb → ^{36}Mg + n + Pb at the beam energy of 244 MeV/nucleon. The ground state
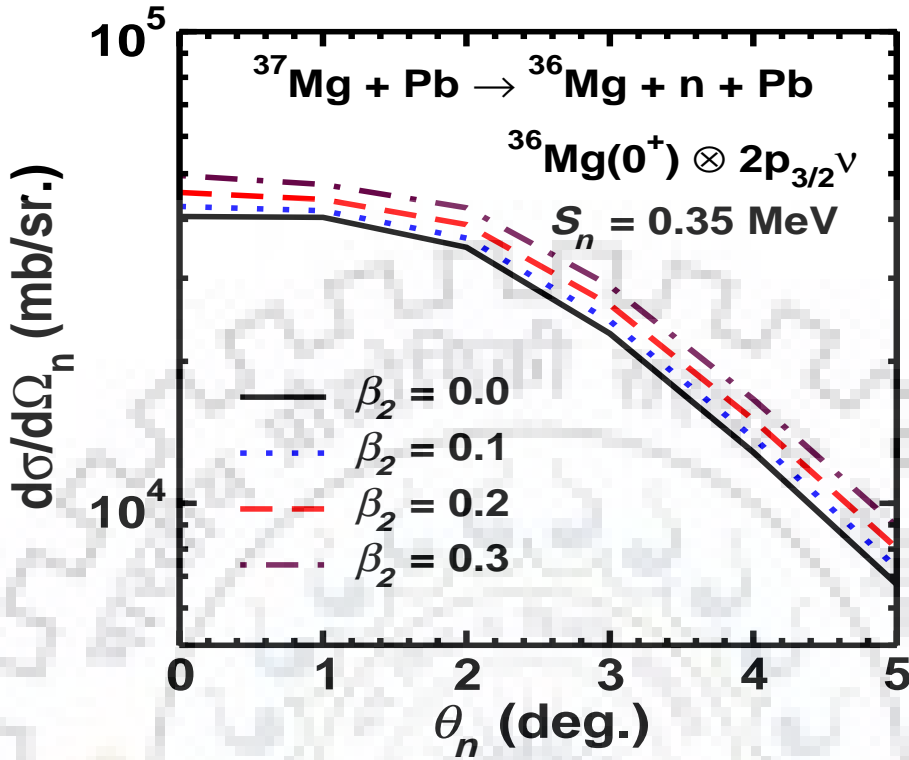
Figure 3.10: Neutron angular distribution for Coulomb break-up of ^{37}Mg on a Pb target at 244 MeV/nucleon beam energy. The projectile ground state configuration, S_n and C^2S were the same as those in Fig. 3.9

configuration, the S_n and C^2S were the same as those in Fig. 3.9. The results are presented for four values of the β_2 parameter. We notice that cross-sections drop very steeply with increasing neutron angle in the forward directions. The narrow angular distributions of neutrons below the grazing angles in the Coulomb break-up reactions of ^{37}Mg reflect the small widths of the parallel momentum distribution and hence the large spatial extension of the valence neutron in its ground state. The effect of the deformation is significant at the forward angles [this was already seen in Fig. 3.9(b)

3.5   Conclusions

In this chapter we have studied the Coulomb break-up reaction $^{37}\text{Mg} + \text{Pb} \rightarrow {}^{36}\text{Mg}$ + n + Pb at the beam energy of 244 MeV/nucleon, within the framework of the post form finite range distorted wave Born approximation theory that is extended to include the projectile deformation effects. In this formalism the transition amplitude is factorized into two parts - one containing the dynamics of the reaction and the another the projectile structure informations such as the fragment-fragment interaction and the corresponding wavefunction in its ground state. Analytic expressions can be written for both parts. This formalism opens up a route to perform realistic quantum mechanical calculations for the break-up of neutron-dripline nuclei in the medium mass region that can be deformed. We calculated the total one-neutron removal cross sections (σ_{-1n}) in this reaction and compared our results with the corresponding data reported in a recent publication [2] in order to determine the configuration of the ^{37}Mg ground state. The analysis of this single measured cross-section already rules out the $^{36}\text{Mg}(0^+) \otimes 1f_{7/2}\nu$ configuration for the ground state of ^{37}Mg. However, it does not allow to exclude either of the $^{36}\text{Mg}(0^+) \otimes 2p_{3/2}\nu$ and $^{36}\text{Mg}(0^+) \otimes 2s_{1/2}\nu$ configurations for $^{37}\text{Mg}_{gs}$. Assuming a spectroscopic factor of one, the extracted values of one-neutron separation energies for these two configurations are 0.35 ± 0.06 MeV and 0.50 ± 0.07 MeV, respectively. However, the deduced S_n depends on the value of C^2S. Our study shows that S_n rises steadily with increasing C^2S. In order to gain more insight in the ground state structure of ^{37}Mg, we studied the effect of the projectile deformation on σ_{-1n}. We find that for the configuration $^{36}\text{Mg}(0^+) \otimes 2p_{3/2}\nu$ for the ^{37}Mg ground state, the calculated σ_{-1n} overlaps with the experimental data band for the quadrupole deformation parameter (β_2) below 0.32. This is in line with the Nilsson model calculations of Ref. [12] where the β_2 for this state is predicted to lie in the range 0.30 - 0.34. However, with the $^{36}\text{Mg}(0^+) \otimes 2s_{1/2}\nu$ configuration, the overlap between calculations and the data occurs for even very large values of β_2. Thus with this configuration, our cal-

culations are unable to put any constraint on deformation parameter β_2. We also calculated more exclusive observables such as the core-valence neutron relative energy spectra, the energy-angle and the angular distributions of the emitted neutron and the parallel momentum distribution of the core fragment. The position of the peak as well as the magnitude of the cross-section near the peak of the core-valence neutron relative energy spectra are found to be dependent on the configuration of the projectile ground state as well as on its deformation. Similar trend was also observed in the parallel momentum distribution of the core fragment. The FWHM of this distribution are found to be of the same order of magnitude as those seen in the break-up of established light halo nuclei. This confirms that ^{37}Mg ground state has a halo structure. The angular distribution of the emitted neutrons is strongly forward peaked and the cross-sections in the forward directions, are dependent on the projectile deformation. Thus, we identified the observables that are more critically dependent on the ground state structure of the projectile. Therefore, our study is expected to provide motivation for future experiments on break-up reactions of the neutron rich medium mass nuclei. In calculations of the break-up reactions of nuclei at higher beam energies, relativistic effects could play a role [48, 49]. Our theory is essentially non-relativistic in nature. Nevertheless, we have seen in Ref. [50] that this theory is able to reproduce well the data on the excitation energy spectra and the total electromagnetic one-neutron removal cross-section in the break-up reaction of ^{23}O on a Pb target at even higher beam energy of 422 MeV/nucleon.

BIBLIOGRAPHY

[1] Nakamura T., *et al.*, Halo Structure of the Island of Inversion Nucleus ^{31}Ne, Phys. Rev. Lett. **103**, 262501 (2009).

[2] Kobayashi N., *et. al.*, Observation of a *p*-Wave One-Neutron Halo Configuration in ^{37}Mg, Phys. Rev. Lett.**112**, 242501 (2014).

[3] Warburton E. K., Becker J. A., and Brown B. A., Mass systematics for A=29 - 44 nuclei: The deformed A 32 region, Phys. Rev. C **41**, 1147 (1990).

[4] Orr N., Mittig W., and Fifield L. K. et al., New mass measurements of neutron-rich nuclei near N= 20 , Phys. Lett. B **258**, 29 (1991).

[5] Otsuka T., Suzuki T., Fujimoto R., Grawe H., and Akaishi Y., Evolution of Nuclear Shells due to the Tensor Force, Phys. Rev. Lett. **95**, 232502 (2005).

[6] Otsuka T., Suzuki T., Honma M., Utsuno Y., and Tsunoda N., *et. al.*, Novel Features of Nuclear Forces and Shell Evolution in Exotic Nuclei, Phys. Rev. Lett. **104**, 012501 (2010).

[7] Motobayashi T., Ikeda Y., Leki K., and Inoue M. *et. al.*, Large deformation of the very neutron-rich nucleus ^{3}2Mg from intermediate-energy Coulomb excitation, Phys. Lett. B **346**, 9 (1995).

[8] Caurier E., Nowacki F., Poves A., and Retamosa J., Shell model study of the neutron rich isotopes from oxygen to silicon, Phys. Rev.C **58**, 2033 (1998).

[9] Utsuno Y., Otsuka T., Mizusaki T., and Honma M., Varying shell gap and deformation in N 20 unstable nuclei studied by the Monte Carlo shell model, Phys. Rev. C **60**, 054315 (1999).

[10] Iwasacki H., Motobayashi T., Sakurai H., and Yoneda K.,*et. al.*, Large collectivity of Mg-34, Phys. Lett. B. **522**, 227 (2001).

[11] Yanagisawa Y. **et. al.**, The first excited state of ^{30}Ne studied by proton inelastic scattering in reversed kinematics, Phys. Lett. B. **566**, 84 (2003).

[12] Hamamoto I., Nilsson diagrams for light neutron-rich nuclei with weakly-bound neutrons, Phys. Rev. C **76**, 054319 (2007).

[13] Hamamoto I., Neutron shell structure and deformation in neutron-drip-line nuclei, Phys. Rev. C **85**, 064329 (2012).

[14] Takechi M., Ohtsubo T., Kuboki T., and Fukuda M., *et al.*, Measurements of nuclear radii for neutron -rich Ne isotopes 28-32 Ne, Nucl. Phys. A **834**, 412 (2010).

[15] Takechi M., Ohtsubo T., Fukuda M., and Nishimura D., *et al.*, Interaction cross sections for Ne isotopes towards the island of inversion and halo structures of ^{2}9Ne and ^{3}1Ne Phys. Lett. B **707**, 357 (2012).

[16] Takechi M., Suzuki S., Nishimura D., and Fukuda M., *et al.*, Search for halo nucleus in Mg isotopes through the measurements of reaction cross sections towards the vicinity of neutron drip line, EPJ Web of Confs. **66**, 02101 (2014).

[17] Minomo K., Sumi T., Kimura M., and Ogata K., *et al.*, Determination of the structure of ^{31}Ne by full-microscopic framework, Phys. Rev. Lett. **108**, 052503 (2012).

[18] Sumi T., Minomo K., Tagami S., Ogata K. and Kimura M., *et al.*, Deformation of Ne isotopes in the island-of-inversion region, Phys. Rev. C **85**, 064613 (2012).

[19] Horiuchi W., Inakura T., Nakatsukasa T., and Suzuki Y., Glauber-model analysis of total reaction cross sections for Ne, Mg, Si, and S isotopes with Skyrme-Hartree-Fock densities, Phys. Rev. C **86**, 024614 (2012).

[20] Watanabe S. *et al.*, Ground-state properties of neutron-rich Mg isotopes, Phys. Rev. C **89**, 044610 (2014).

[21] Wang M., Audi G., Wapstra A. H., and Kondev F. G., The Ame2012 atomic mass evaluation, Chin. Phys. C **36**, 1603 (2012).

[22] Gade A., *et al.*, Spectroscopy of Mg-36: Interplay of Normal and Intruder Configurations at the Neutron-Rich Boundary of the 'Island of Inversion', Phys. Rev. Lett. **99**, 072502 (2007).

[23] Doornenbal P., *et al.*, In-Beam γ -Ray Spectroscopy of ^{34,36,38}Mg : Merging the N = 20 and N = 28 Shell Quenching, Phys. Rev. Lett. **111**, 212502 (2013).

[24] Terasawa M., Sumiyoshi K., Kajino T., Mathews G. J., and Tanihata I., New Nuclear Reaction Flow during r-Process Nucleosynthesis in Supernovae: Critical Role of Light Neutron-rich Nuclei, Astr. J. **562**, 470 (2001).

[25] Hamamoto I., Dominance of low-l component in weakly bound deformed single-neutron orbits, Phys. Rev. C **69**, 041306(R) (2004).

[26] Fäldt G. and Glauber R., Diffraction theory of scattering by rotating nuclei, Phys. Rev. C **42**, 395 (1990).

[27] Chatterjee R., Banerjee P. and Shyam R., Projectile structure effects in the Coulomb breakup of one-neutron halo nuclei, Nucl. Phys. A **675**, 477 (2000).

[28] Moshinsky M., Transformation brackets for harmonic oscillator functions, Nucl. Phys. **13**, 104 (1959).

[29] Nordsieck, Reduction of an Integral in the Theory of Bremsstrahlung, Phys. Rev. **93**, 785 (1954).

[30] Hansen P. G. and Tostevin J. A., DIRECT REACTIONS WITH EXOTIC NUCLEI, Annu. Rev. Nucl. Part. Sci. **53**, 219 (2003).

[31] Nakamura T. *et al.*, Deformation-Driven p- Wave Halos at the Drip Line: ^{31}Ne, Phys. Rev. Lett. **112**, 142501 (2014).

[32] Campi X., Flocard H., Kerman A. K., and Koonin S., Shape transition in the neutron rich sodium isotopes, Nucl. Phys. A **251**, 193 (1975).

[33] Poves A. and Retamosa J., Theoretical study of the very neutron-rich nuclei around N = 20, Nucl. Phys. A **571**, 221 (1994).

[34] Watt A., Singhal R. P., Storm M. H. and Whitehead R. R., A shell-model investigation of the binding energies of some exotic isotopes of sodium and magnesium, J. Phys. G **7**, 145 (1981).

[35] Banerjee P. and Shyam R., Structure of ^{19}C from Coulomb dissociation studies, Phys. Rev. C **61**, 047301 (1999).

[36] Baur G., Hencken K. and Trautmann D., Electromagnetic dissociation as a tool for nuclear structure and astrophysics, Prog. Part. Nucl. Phys. **51**, 487 (2003).

[37] Nagarajan M. A., Lenzi S. and Vitturi A., Low-lying dipole strength for weakly bound systems: A simple analytic estimate, Eur. Phys. J. A **24**, 63 (2005).

[38] Singh J., Fortunato L., Vitturi A. and Chatterjee R., Electric multipole response of the halo nucleus 6He, Eur. Phys. J. A **52**, 209 (2016).

[39] Chatterjee R., Fortunato L. and Vitturi A., Role of Higher Multipole Excitations in the Electromagnetic Dissociation of One Neutron Halo Nuclei, Eur.J.Phys. A **35**, 213 (2008).

[40] Mason A., Chatterjee R., Fortunato L., and Vitturi A., Electric and magnetic response to the continuum for A = 7 isobars in a dicluster model, Eur. Phys. J. A **39**, 107 (2009).

[41] Typel S. and Baur G., Electromagnetic strength of neutron and proton single-particle halo nuclei, Nucl. Phys. A **759**, 247 (2005).

[42] Baur G. and Trautmann D., The Coulomb break-up of the deuteron, Nucl. Phys. A **191**, 321 (1972).

[43] Baur G., Rösel F., Trautmann D., and Shyam R., Fragmentation processes in nuclear reactions, Phys. Rep. **111**, 333 (1984).

[44] Banerjee P. and Shyam R., Coulomb and nuclear effects in the fragmentation of exotic nuclei, Nucl. Phys. A **561**, 112 (1993).

[45] Banerjee P. and Shyam R., Energy and momentum distribution of fragments in reactions induced by one neutron halo nucleus, J. Phys. G: Nucl. Part. Phys. **22**, 79 (1996).

[46] Banerjee P., Baur G., Hencken K., Shyam R. and Trautmann D., Postacceleration effects in the Coulomb dissociation of neutron halo nuclei, Phys. Rev. C **65**, 064602 (2002).

[47] Esbensen H., Angular distribution of neutrons emitted in (11 Li, 9 Li) breakup reactions, Phys. Rev. C **44**, 440 (1991).

[48] Bertulani C. A., Relativistic continuum-continuum coupling in the dissociation of halo nuclei, Phys. Rev. Lett. **94**, 072701 (2005).

[49] Ogata K., Bertulani C. A., Dissociation of relativistic projectiles with the continuum-discretized coupled-channels method, Progr. Theor. Phys. **121**, 1399 (2009).

[50] Chatterjee R., Shyam R., Tsushima K. and Thomas A. W., Structure and Coulomb dissociation of ^{23}O within the quark-meson coupling model, Nucl. Phys. A **913**, 116 (2013).

PART - II

CHAPTER 4

STUDY OF CAPTURE REACTION ^{15}N$(n, \gamma)^{16}$N
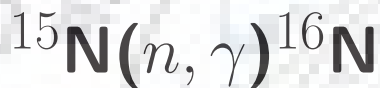
4.1 Introduction

In this chapter we will study break-up of ^{16}N nucleus on target Pb at energy 100 MeV/nucleon to study the capture cross-section and reaction rates of ^{15}N$(n, \gamma)^{16}$N. For the ^{15}N$(n, \gamma)^{16}$N reaction direct measurements have been possible only at few energies below 500 keV [1]. The situation can be addressed by an indirect method like the Coulomb dissociation method. The ^{14}C$(n, \gamma)^{15}$C [2] and ^{7}Li$(n, \gamma)^{8}$Li [3] neutron capture reactions are two recent examples where the Coulomb dissociation method have been used to study the corresponding radiative capture cross-section. Therefore it would be interesting to investigate if in the case of ^{15}N$(n, \gamma)^{16}$N too indirect measurements add to a better understanding of capture cross-sections at low energies. In section **4.2** presents review of the ^{15}N$(n, \gamma)^{16}$N radiative capture reaction. In section **4.3**, a brief formalism of the Coulomb break-up process and the capture cross-section is presented. Results are presented in section **4.4**, where the

capture cross-section and rate of the ^{15}N$(n, \gamma)^{16}$N reaction are calculted from the Coulomb dissociation of ^{16}N and in section **4.5** are the conclusions.

4.2   Overview of the ^{15}N$(n, \gamma)^{16}$N radiative capture reaction

The radiative neutron capture ^{15}N$(n, \gamma)^{16}$N reaction, plays an important role in the synthesis of heavy elements by *s*-process nucleosynthesis in red giant stars and also in the inhomogeneous big bang model [4–6]. This reaction is also a part of the neutron induced chain which leads to the breakout from the CNO cycle and hence depletion of CNO abundances [7]. Being the competing reaction with ^{15}N$(\alpha, \gamma)^{19}$F, the neutron capture ^{15}N$(n, \gamma)^{16}$N reaction is also important in determining the abundance of Fluorine [8, 9]. Furthermore, it is also thought to compete with charged particle capture reactions on ^{15}N [5] and therefore can affect the abundance of heavier mass elements.

The only direct measurement of the ^{15}N$(n, \gamma)^{16}$N capture cross-section has been performed at neutron lab energies of 25, 152 and 370 keV by Meissner *et al.* [1]. The direct capture calculations performed in order to explain the data using experimental spectroscopic factor (C^2S) [10], show a *p*-wave dominated capture. These C^2S had an inherent uncertainity of 30%. Further, their calculated reaction rates were $30-50\%$ smaller than those calculated by Rauscher *et al.* [11]. Theoretical calculations by Herndl *et al.* [12], in the framework of a hybrid compound and direct capture model (C^2S from Ref. [10]) were used to explain the data [1] and their calculated rates were in agreement with those of Ref. [11]. Another direct capture calculation has been performed in Ref. [13] using potential model [14] with C^2S from Ref. [10].

In fact, the capture cross-section and the rate of the ^{15}N$(n, \gamma)^{16}$N reaction strongly depends upon the C^2S of the four low-lying levels (with spin-parity $J^\pi = 2^-$, 0^-, 3^- and 1^-) in ^{16}N. The calculations of Refs. [1, 13], could account for the data only when the suggested 30% uncertainty in the C^2S from Ref. [10] were con-

sidered. But this was not the case with the calculations of Ref. [12]. A point also to be noted is that the experimentally extracted $C^2 S$ in Ref. [10] are almost half as those calculated from shell model [1, 10], which gives a pure single particle picture of these levels. In this regard, an experiment was performed by Bardayan *et al.* [8], where they extracted the $C^2 S$ for all these four levels, from the measured angular distribution of ^{15}N$(d, p)^{16}$N. These $C^2 S$ values obtained were close to unity and were in good agreement with those suggested by the shell model [1, 10]. However, the $C^2 S$ values extracted in a recent experiment [9] from the measured angular distribution of ^{15}N$(^7$Li, ^{6}Li$)^{16}$N, are not in full agreement with either of the previous experiments [8, 10]. Their $C^2 S$ values suggest that the two levels of ^{16}N (with $J^{\pi} = 2^-$ and 3^-) are good single-particle levels whereas, the other two (with $J^{\pi} = 0^-$ and 1^-) are not.

     With this background we present an indirect method of calculating the ^{15}N$(n, \gamma)^{16}$N radiative capture cross-section from the Coulomb break-up of ^{16}N on Pb at 100 MeV/nucleon beam energy. The Coulomb break-up theory is fully quantum mechanical and is calculated under the post-form finite range distorted wave Born approximation (FRDWBA) [15]. The theory is mainly analytic in nature given that pure Coulomb wavefunctions are used in the calculation and that the dynamics can be exactly evaluated. Thus, the main aim of this chapter is to use this theory to calculate the ^{15}N$(n, \gamma)^{16}$N radiative capture cross-section and its subsequent reaction rate by an indirect method and in that process investigate the effects of $C^2 S$ of different levels of ^{16}N to the cross section. Previously this theory has been successfully applied to calculate the radiative neutron capture cross-sections and subsequent rates of the reactions ^{8}Li$(n, \gamma)^9$Li [16] and ^{14}C$(n, \gamma)^{15}$C [17] from the Coulomb break-up of ^{9}Li and ^{15}C, respectively.

.

4.3   Formalism

4.3.1   Calculation of radiative capture cross-section

The photodisintegration cross-section $(\sigma_{\gamma,n}^{\pi\lambda})$ for the reaction $a + \gamma \rightarrow b + n$ can be related to the relative energy spectra using Eq.(2.43) from chapter 2 as,

$$\frac{d\sigma}{dE_{rel}} = \frac{1}{E_\gamma} \sum_{\pi\lambda} \sigma_{\gamma,n}^{\pi\lambda} \, \text{n}_{\pi\lambda}, \tag{4.1}$$

In Eq. (4.1), $E_\gamma = E_{bn} + Q$ is the photon energy with Q as the Q-value of the reaction, π stands for either electric or magnetic transition of multipolarity λ and $\text{n}_{\pi\lambda}$ is the equivalent photon number which depends upon the $a - t$ system [17–20]. The equivalent photon number, $\text{n}_{\pi\lambda}$ given by

$$\text{n}_{\pi\lambda} = \int_0^{\theta_{gz}} \frac{d\text{n}_{\pi\lambda}}{d\Omega_{at}} d\Omega_{at}, \tag{4.2}$$

where θ_{gz} is the grazing angle for the scattering and $\frac{d\text{n}_{\pi\lambda}}{d\Omega_{at}}$ is the equivalent photon number per unit solid angle [18, 21, 22].

The photodisintegration cross-section in Eq.(4.1) is calculated for all possible multipolarities, both elecric and magnetic but in case a single multipolarity dominates, [23, 24] (as in ^{16}N, the γ-ray transitions to all four low lying levels 2^-, 0^-, 3^-, 1^- are dominated by $E1$ multipolarity [1, 13]). Virtual photon number per unit solid angle is given by

$$\frac{dn_{E1}}{d\Omega_{at}} = \frac{Z_t^2\alpha}{4\pi^2}\left(\frac{c}{v_{at}}\right)^2\epsilon^4\eta^2 e^{-\pi\eta}\left[\frac{1}{\gamma^2}\frac{\epsilon^2-1}{\epsilon^2}(K_{i\eta}(\epsilon\eta))^2 + (K_{i\eta}'(\epsilon\eta)^2)\right]. \tag{4.3}$$

Here $\eta = E_\gamma a/\hbar v_{at}\gamma$, with $a = Z_a Z_t e^2/\mu_{at}v_{at}^2$, being the half distance of closest approach in the head on collision. $\alpha = e^2/\hbar c$, $K_{i\eta}(y)$ are the modified Bessel functions and $K_{i\eta}'(y)$ is derivative of $K_{i\eta}(y)$ with respect to y. Further ϵ is the eccentricity parameter and it is related to the scattering angle $\epsilon = 1/\sin(\theta_{at}/2)$. The relativistic factor, γ is given by $\gamma = \frac{1}{\sqrt{1-v_{at}^2/c^2}}$.

For the case of a single multipolarity contributing to the cross-section, the photodisintegration cross-section simplifies to

$$\sigma_{\gamma,n}^{\pi\lambda} = \frac{E_\gamma}{n_{\pi\lambda}} \frac{d\sigma}{dE_{bn}}, \tag{4.4}$$

The radiative capture cross-section ($\sigma_{n,\gamma}$) can then be calculated utilising the principle of detailed balance,

$$\sigma_{n,\gamma} = \frac{2(2j_a + 1)}{(2j_b + 1)(2j_n + 1)} \frac{k_\gamma^2}{k_{bn}^2} \sigma_{\gamma,n}^{\pi\lambda}, \tag{4.5}$$

where j_a, j_b and j_n are the spins of particles a, b and n, respectively. k_γ and k_{bn} are the wave numbers of the photon and that of relative motion between b and n, respectively and are given by $E_\gamma/\hbar c$ and $\sqrt{2\mu_{bn} E_{bn}/\hbar^2}$ respectively.

4.3.2 Calculation of reaction rates

The non-resonant reaction rate per mole $N_A \langle \sigma v \rangle_{nr}$ (N_A being Avogadro constant) can be calculated from the neutron capture cross section $\sigma_{n,\gamma}(E_{bn})$ as [25, 26]:

$$N_A \langle \sigma v \rangle_{nr} = N_A \sqrt{\frac{8}{(k_B T)^3 \pi \mu_{bn}}}$$

$$\times \int_0^\infty \sigma_{n,\gamma}(E_{bn}) \, E_{bn} \, exp(-\frac{E_{bn}}{k_B T}) \, dE_{bn}, \tag{4.6}$$

Here E is in MeV, T in GK, μ in amu and σ is in barns ($10^{-28} m^2$), $k_B = 1.38 \times 10^{-23}$ JK^{-1} is Boltzmann's constant.

Substituting the constant values results in

$$N_A \langle \sigma v \rangle_{nr} = \frac{3.7318 \times 10^{10}}{(\mu_{bn} T^3)^{1/2}}$$

$$\times \int_0^\infty \sigma_{n,\gamma}(E_{bn}) \, E_{bn} \, exp(-11.605\frac{E_{bn}}{T}) \, dE_{bn} \, (cm^3 mol^{-1} s^{-1}), \tag{4.7}$$

Once $\sigma_{n,\gamma}$ is calculated, reactions rates can be calculated. When the significant

contribution to the reaction rate comes from a very small range of energies then the whole integration range in the previous equation need not be considered.

In case of narrow resonances, the capture cross-section can be obtained by using the one- level Breit-Wigner formula and is given by

$$\sigma_{BW}(E_{bn}) = \frac{\lambda^2(2J+1)(1+\delta_{bn})}{4\pi(2j_b+1)(2j_n+1)}\frac{\Gamma_{in}\Gamma_{out}}{(E_r - E_{bn})^2 + (\Gamma^2/4)} \tag{4.8}$$

λ is de Broglie wavelength which is given by $2\pi\hbar/\sqrt{2\mu_{bn}E_{bn}}$, J_b, J_n are spins of b and neutron. Resonant state spin and energy is J, E_r respectively. Γ_{in} and Γ_{out} are partial widths of initial and final channel respectively. Γ is total resonance width. Each partial width has to be summed over all possible values of angular momentum. The factor $1+\delta_{bn}$ is used as cross-section for identical particles doubled in entrance channel.

Reaction rate for a narrow resonance is given by

$$N_A\langle\sigma v\rangle_{res} = N_A\sqrt{\frac{8}{(k_BT)^3\pi\mu_{bn}}}$$
$$\times \int_0^\infty \sigma_{BW}(E_{bn})\,E_{bn}\,exp(-\frac{E_{bn}}{k_BT})\,dE_{bn}, \tag{4.9}$$

$$N_A\langle\sigma v\rangle_{res} = N_A\frac{\sqrt{2\pi}\hbar^2}{(\mu k_BT)^{3/2}}\omega\int_0^\infty \frac{\Gamma_{in}\Gamma_{out}}{(E_r - E_{bn})^2 + (\Gamma^2/4)}\,dE_{bn}. \tag{4.10}$$

Here $\omega \equiv (2J+1)(1+\delta_{bn})/[(2j_b+1)(2j_n+1)]$. In case of narrow resonances, the value of Maxwell- Boltzmann factor, e^{-E_{bn}/k_BT} and partial widths, Γ_i remains constant over total width of resonances. One can, in principle, replace them with their values

at E_r. Thereby, paving a way for analytic calculation of reaction rates.

$$N_A\langle\sigma v\rangle_{res} = N_A\frac{\sqrt{2\pi}\hbar^2}{(\mu_{bn}k_BT)^{3/2}}\,e^{-E_r/k_BT}\,\omega\frac{\Gamma_{in}\Gamma_{out}}{\Gamma}2$$

$$\times\int_0^\infty\frac{\Gamma/2}{(E_r - E_{bn})^2 + (\Gamma^2/4)}\,dE_{bc}.$$

$$= N_A\frac{\sqrt{2\pi}\hbar^2}{(\mu_{bn}k_BT)^{3/2}}e^{-E_r/k_BT}\omega\frac{\Gamma_{in}\Gamma_{out}}{\Gamma}2\pi$$

$$= N_A\left(\frac{2\pi}{\mu_{bn}k_BT}\right)^{3/2}\hbar_2 e^{-E_r/k_BT}\omega\gamma \qquad (4.11)$$

Resonance strength, $\omega\gamma$ is taken as ($=\omega\Gamma_{in}\Gamma_{out}/\Gamma$) and depends upon strength of the resonance cross-section.

For multiple narrow and isolated resonances, reaction rate per mole can be easily expressed as the sum over individual resonances with energy E_i [25] as

$$N_A\langle\sigma v\rangle_{res} = 1.54\times10^{11}(\mu_{bn}T)^{-3/2}$$

$$\times\sum_i(\omega\gamma)_i exp\left(\frac{-11.605E_i}{T_9}\right), \qquad (4.12)$$

Reaction rates for narrow resonances depends upon the energy and strength of resonance. Total reactions rates can be now calculated by summing non resonant reaction rates and resonant reaction rates.

4.4 Results and discussions

4.4.1 Structure of ^{16}N

^{16}N has one-neutron separation energy (S_n) of 2.491 MeV in its ground state having $J^\pi = 2^-$. There are three low-lying excited states with $J^\pi = 0^-$, 3^- and 1^- at energies 0.120, 0.298 and 0.397 MeV above the ground state, respectively. Two states 2^- and 3^- are formed by the coupling of $1d_{5/2}$ ν with the $1/2^-$ ground state of ^{15}N, whereas the other two states 0^- and 1^- are formed by the coupling of $2s_{1/2}$

ν with the $1/2^-$ ground state of ^{15}N. All these four levels have been suggested to contribute to the direct capture cross-section of ^{15}N$(n, \gamma)^{16}$N [1, 12, 13] and the capture process is dominated by E1 transitions [13]. Apart from these, the 862 keV resonance is the only relevant resonance which has been suggested to contribute to the reaction rate at high temperature (> 1 GK) [1].

In our study, we calculate the bound state wave function of the projectile (which is the only input in our theory) by assuming a Woods-Saxon interaction between the valence neutron and the charged core. The depth (V_0) of the potential is adjusted to reproduce the binding energy. The radius and diffuseness parameters are taken to be 1.25 fm and 0.65 fm, as in Refs. [9, 13].

We use shell model C^2S values which considers low-lying ^{16}N levels as good single-particle states. In fact, these are also supported by the experiment performed in Ref. [8]. Another support to our choice comes from isospin symmetry, given that the C^2S for low-lying four levels in mirror nucleus ^{16}F are near unity [27, 28]. Nevertheless, we have also performed our calculations with the C^2S of Refs. [9, 10] for the sake of completeness.

Table 4.1: Depths (V_0) of the Woods-Saxon potential obtained corresponding to neutron binding energies (S_n) of four low-lying states of ^{16}N. The shell model C^2S (OXBASH) of these levels are from Ref. [1]. The values of the radius and diffuseness parameters are taken to be 1.25 fm and 0.65 fm, respectively.

J^π	configuration	S_n (MeV)	V_0 (MeV)	C^2S
2^-	^{15}N$(1/2^-)\otimes 1d_{5/2}\nu$	2.491	58.06	0.93
0^-	^{15}N$(1/2^-)\otimes 2s_{1/2}\nu$	2.371	53.89	0.95
3^-	^{15}N$(1/2^-)\otimes 1d_{5/2}\nu$	2.193	45.04	0.87
1^-	^{15}N$(1/2^-)\otimes 2s_{1/2}\nu$	2.094	49.38	0.96

In Table 4.1, we show the respective depths of the Woods-Saxon potential obtained corresponding to neutron removal from all four levels mentioned above, along with their S_n and C^2S values.

4.4.2 Capture cross-section

The first step to calculate the capture cross-section is to calculate the relative energy spectra, which we have done for the Coulomb break-up of ^{16}N on a Pb target at 100 MeV/nucleon beam energy for all projectile bound state configurations mentioned in Table 4.1. From the relative energy spectra we calculate the photodisintegration
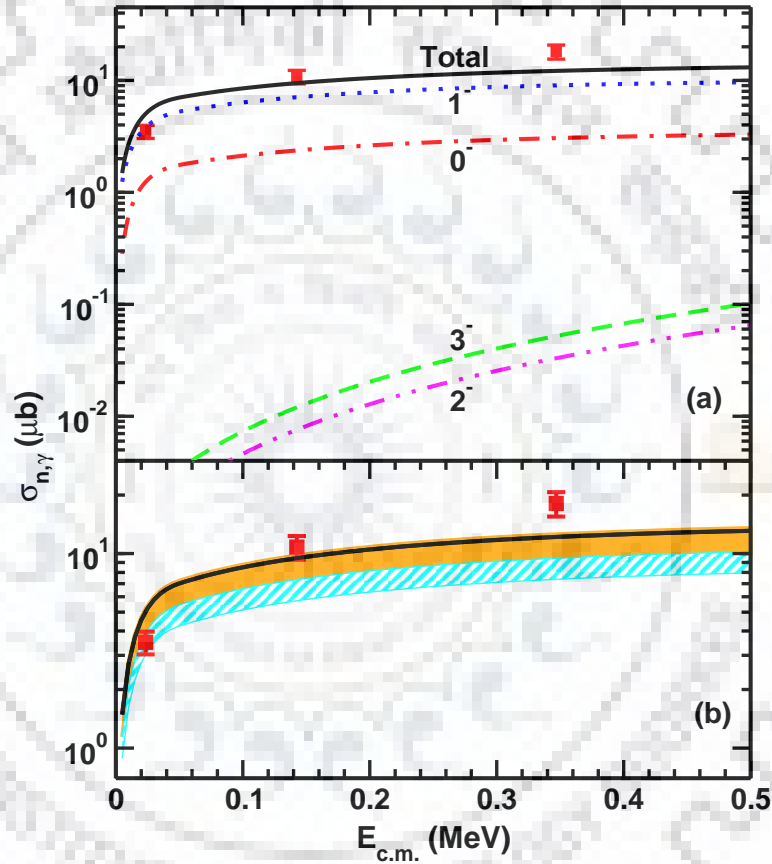

Figure 4.1: (a) Total non-resonant ^{15}N$(n, \gamma)^{16}$N cross-section (solid line) obtained by summing up contributions of capture to all four states of ^{16}N (given in Table I) using their respective shell model C^2S. (b) Total non-resonant capture cross-section obtained by using the experimentally extracted C^2S (including uncertainties) from Ref. [8] (filled band) and Ref. [9] (filled pattern) compared with the total non-resonant cross-section (solid line) shown in (a). The experimental data in both panels are from [1].

cross-section for the reaction ^{16}N$(\gamma, n)^{15}$N, using Eq.(4.4). This is the key step in using Coulomb dissociation as an indirect method in nuclear astrophysics. Furthermore, given that the gamma ray transition corresponding to all four levels of ^{16}N of

present interest are all dominated by E1 multipolarity [13], so the conditions for the applicability of Eq. (4.4) are fulfilled. The photodisintegration cross-sections are then used to calculate the radiative capture cross-sections by applying the principle of detailed balance [Eq. (4.5)].

In Fig. 4.1 (a), we show our $^{15}\text{N}(n,\gamma)^{16}\text{N}$ non-resonant capture cross-section as a function of the center of mass energy ($\text{E}_{c.m.}$) and compare it with the experimental data, which are available at three energies in the range $0 - 500$ keV. The solid line corresponds to total non-resonant capture cross-section which is obtained by summing up capture contributions to all the four levels of ^{16}N using their respective shell model C^2S values (given in Table I).

It is clear that among all these four states, nearly all the contribution to the total cross-section, come from the 1^- and the 0^- states. Therefore the change in C^2S of these two states can change the total cross-section to a significant extent. This point is further elucidated when in Fig. 4.1 (b), we compare the total capture cross-section with experimentally extracted C^2S (including their uncertainties) from Refs. [8] (filled band) and [9] (filled pattern) with those of the shell model (solid line). Clearly the difference between the C^2S of the 1^- and the 0^- states in these two experiments is the reason for their disagreement among the calculated cross-sections in Fig. 4.1 (b). It is clear that with the shell model C^2S (which is also supported by the upper limit of the calculations using C^2S of Ref. [8]), our results are in good agreement with the data. This would support the contention that the low-lying states of ^{16}N are predominantly single particle in nature.

We also wish to point out that capture cross-sections at energies below 500 keV will not have any significance contribution from the 862 keV resonance. However, it could contribute to the reaction rate for temperatures $T_9 > 1$, as will be seen later.

4.4.3 Dependence of the capture cross-section on Woods-Saxon parameters

We now investigate the dependence of the Woods-Saxon potential parameters on our results. In Fig. 4.2, we show the variation of the total capture cross-section for different combinations of the radius and diffuseness parameters which reproduce the same one neutron separation energy in ^{16}N. The solid line shows the result that we have used in this chapter. The dashed and dotted lines are those in which the radius and diffuseness parameters have been increased by 20%, respectively, over those shown by the solid line. We do not make out any major discernible difference in the results which could be validated by present day experiments.
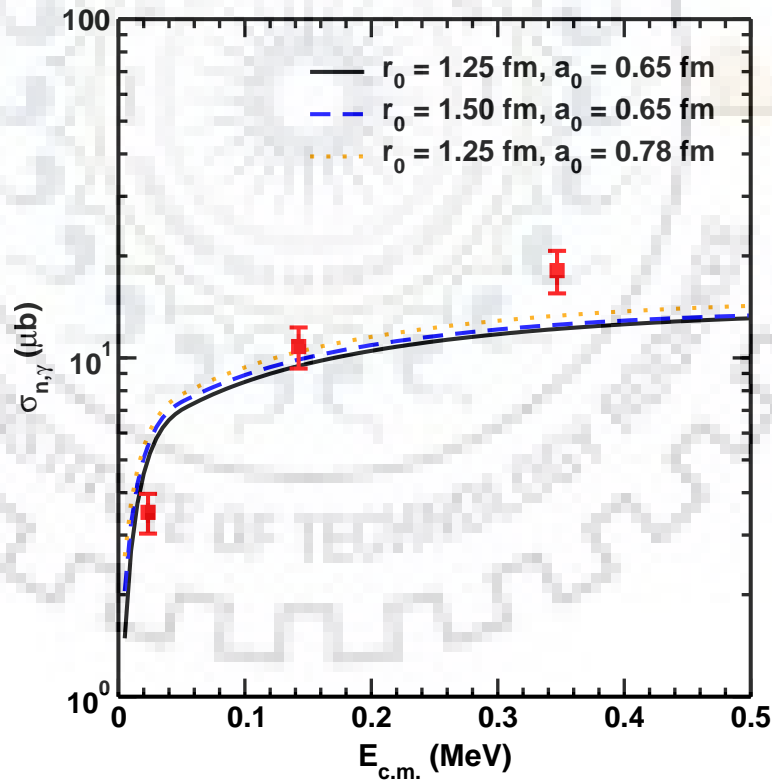

Figure 4.2: Variation of the total ^{15}N$(n, \gamma)^{16}$N capture cross-section with different Woods-Saxon parameterization.

4.4.4 Reaction rates

As mentioned earlier, ^{15}N$(n, \gamma)^{16}$N plays important role in the synthesis of heavier nuclei and also it is considered to compete with other charged particle reactions on ^{15}N. So it would be interesting to find the rate of the ^{15}N$(n, \gamma)^{16}$N reaction and compare it with the other charged particle reaction rates. In Fig. 4.3, we present

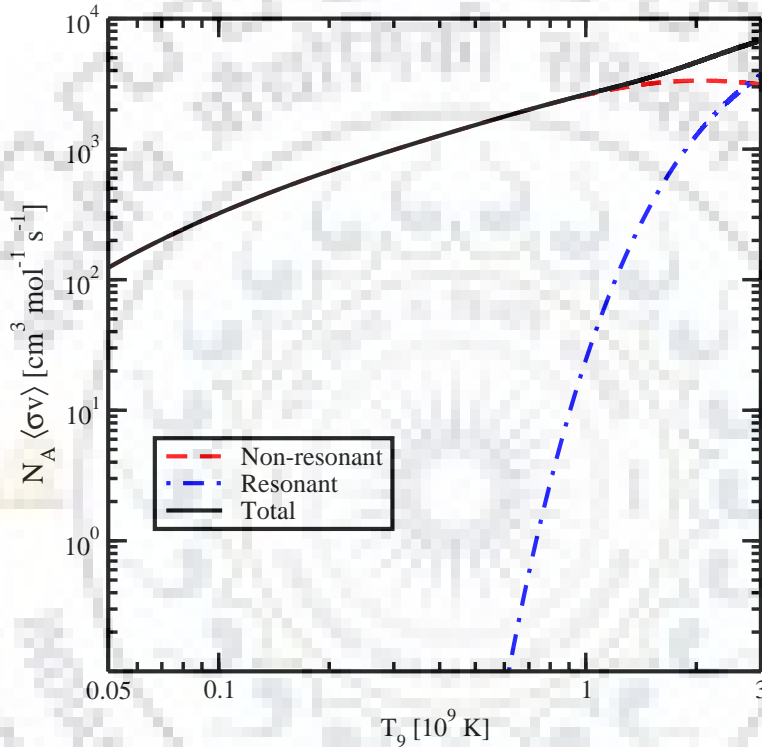**Figure 4.3:** Total ^{15}N$(n, \gamma)^{16}$N reaction rate (solid line) obtained by summing up the non-resonant (dashed line) and resonant (dot-dashed line) rates.

our ^{15}N$(n, \gamma)^{16}$N reaction rate in the temperature range $T_9 = 0.05 - 3$. The total rate (solid line) is the sum of non-resonant (dashed line) and resonant (dot-dashed line) rates. The non-resonant reaction rates are calculated by using Eq. (4.6), where the energy integration has been performed upto 0.5 MeV, consistent with the energy range shown in Fig. 4.1. In order to ensure that we have not missed any contribution to the non-resonant rates at higher energies we plot the integrand in Eq. (4.6) as a function of energy [at $T_9 = 0.1$, a typical temperature of Asymptotic Gaint Branch (AGB) stars] in Fig. 4.4. It is clear from the figure that at this temperature almost

all the contribution to the non-resonant rate is from the energy range below 0.1 MeV. In fact, we have checked that even at a higher temperature (at $T_9 = 1$) the contribution after 0.25 MeV is negligible. This shows that even in the temperature range relevant for inhomogeneous big bang model i.e. $T_9 = 0.2 - 1.2$, the maximum contribution to the non-resonant rate of ^{15}N$(n, \gamma)^{16}$N comes from the energies below 0.25 MeV. Fig. 4.1 shows that in this energy range our calculated neutron capture cross section are in good agreement with the experimental data. The resonant rates are calculated using Eq. (4.12) with the parameters given in Ref. [1]. They seem to be relevant only for temperatures $T_9 > 1$. As can be expected, different C^2S of the
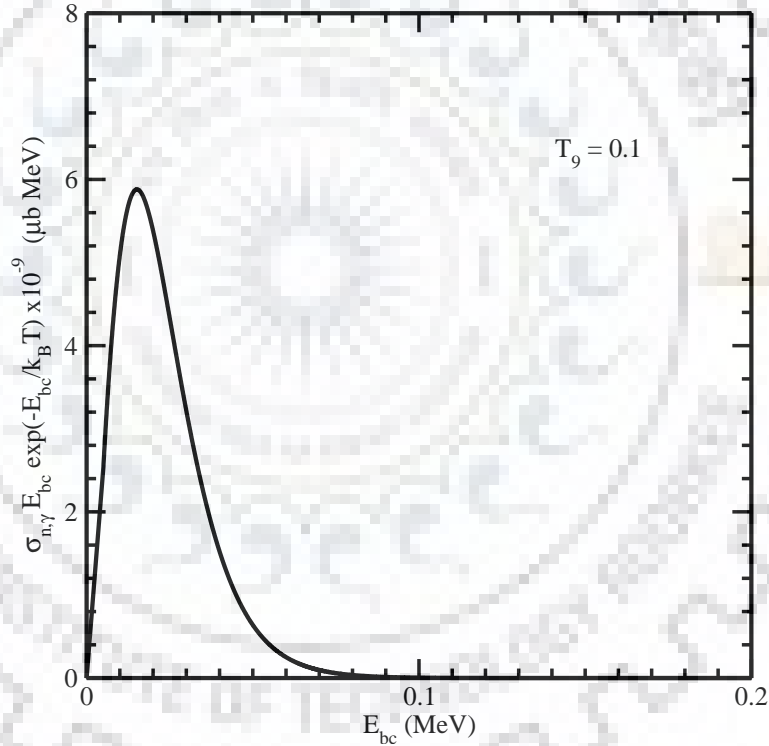
Figure 4.4: Integrand in Eq. (4.6), plotted as a function of relative energy (E_{bc}) for T_9 = 0.1 (typical temperature of AGB stars).

levels of ^{16}N affects the reaction rate and this has also been seen by several authors so far. In Fig. 4.5, we compare our total rates (solid line) with the rates from other theoretical predictions and evaluations based on various experimental estimates of C^2S [1,8,9,11]. The rates reported by Meissner *et al.* in Ref. [1] (dot-dashed line) are

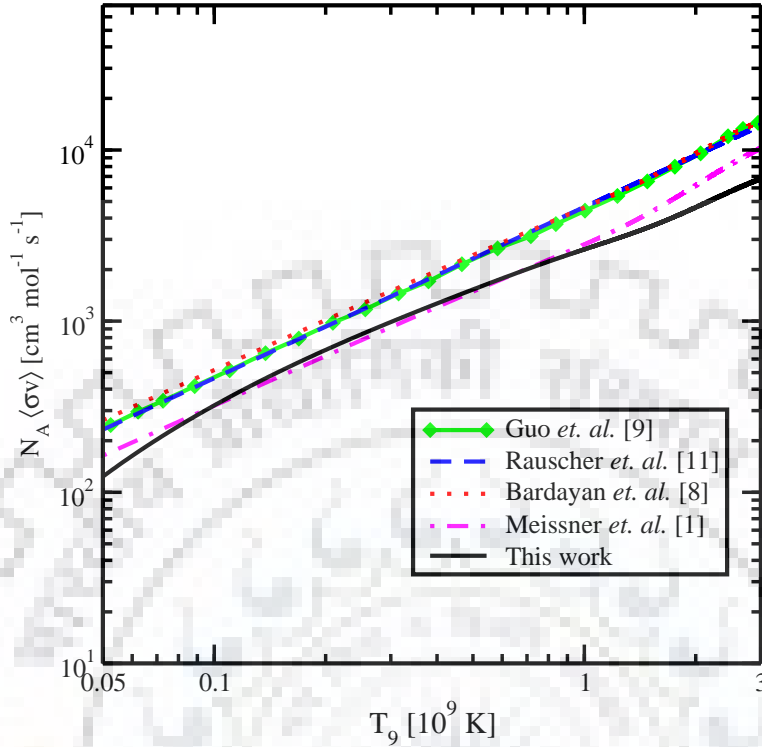**Figure 4.5:** Calculated $^{15}\text{N}(n,\gamma)^{16}\text{N}$ reaction rate (solid line) compared with other evaluations based on various experimental estimates of C^2S.

smaller than the rates calculated by Rauscher *et al.* [11] (dashed line) by $30-50\%$ and this discrepancy was traced to the different C^2S used. Rates calculated by Bardayan *et al.* [8] (dotted line), using their experimentally extracted C^2S were also almost double as compared to those calculated in Ref. [1]. The discrepancy of a similar factor has also been reported recently by Guo *et al.* in Ref. [9] (squared line), on comparing their rates with those of Meissner *et al.*

It is clear that in the temperature ranges relevant for inhomogeneous big bang model ($T_9 = 0.2 - 1.2$) and for typical AGB stars ($T_9 \approx 0.1$), our rates are almost same as those in Ref. [1]. However, in the same temperature range our predicted rates are slower than those of Refs. [8,9,11]. We reiterate that our reaction rates are based on capture cross-sections derived from a fully quantum mechanical Coulomb break-up theory.

Finally, we turn our attention to the comparison of our rates with those of

charged particle capture on ^{15}N. Fig. 4.6, shows the comparison of the rates of reactions ^{15}N$(n,\gamma)^{16}$N, ^{15}N$(p,\alpha)^{12}$C, ^{15}N$(p,\gamma)^{16}$O and ^{15}N$(\alpha,\gamma)^{19}$F in the temperature range of $T_9 = 0.001 - 3$. The rates of (p,γ) and (p, α) reactions are from NACRE II compilation [29], whereas those of (α, γ) are from NACRE compilation [30]. It is clear that at low temperature because of the Coulomb barrier the charged particle capture rates are significantly slower than the (n,γ) rate. Consequently the ^{15}N$(n,\gamma)^{16}$N reaction dominates over the ^{15}N$(p,\alpha)^{12}$C and ^{15}N$(p,\gamma)^{16}$O reactions in the temperature ranges $T_9 = 0 - 0.25$ and $0 - 1.3$, respectively. Again, given the fact that the rate of the ^{15}N$(\alpha,\gamma)^{19}$F reaction is very small in the given temperature range, formation of ^{16}N by neutron capture would be more favorable than the production of ^{19}F. Therefore, it appears that at temperatures below $T_9 < 0.25$, the probability of consumption of ^{15}N by neutron capture is more than the proton or alpha capture reactions.

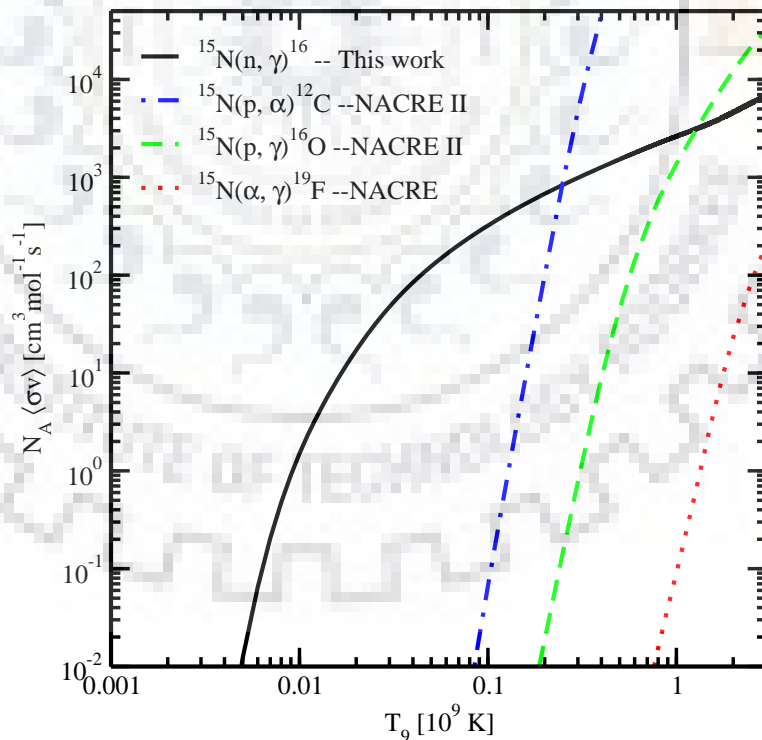**Figure 4.6:** Calculated ^{15}N$(n,\gamma)^{16}$N reaction rate (solid line) compared with those of ^{15}N$(p,\alpha)^{12}$C [29] (dot-dashed line), ^{15}N$(p,\gamma)^{16}$O [29] (dashed line) and ^{15}N$(\alpha,\gamma)^{19}$F [30] (dotted line).

4.5 Conclusions

In summary, we have calculated the $^{15}\text{N}(n,\gamma)^{16}\text{N}$ radiative capture cross-section and the associated reaction rate by using the Coulomb dissociation of ^{16}N on Pb at 100 MeV/nucleon, as an indirect method in nuclear astrophysics. Our Coulomb dissociation theory is purely quantum mechanical one, under the aegis of the post-form finite range distorted wave Born approximation. The entire non-resonant continuum is included in the theory and the projectile bound state information is the only input. The local momentum approximation to the transition amplitude allows us to factorize the break-up amplitude into the structure and the dynamics part. This theory has previously been used to study the structure and dynamics of nuclei away from the valley of stability and also to study radiative capture reactions.

We calculate the relative energy spectra in the break-up of ^{16}N on Pb at 100 MeV/nucleon and calculate the relevant photodisintegration cross-sections for the four low-lying states (2^-, 0^-, 3^- and 1^-) of ^{16}N. The principle of detailed balance is then invoked to calculate the relevant $^{15}\text{N}(n,\gamma)^{16}\text{N}$ radiative capture cross-sections to the different low-lying states of ^{16}N. We then bring into focus the state of affairs regarding the spectroscopic factors of these low-lying states. Comparison of our calculations with the available direct capture data [1] seems to favour the spectroscopic factors from Ref. [8] (which are similar to the shell model) than those of Refs. [9,10]. This would give the credence to the fact that the low-lying levels of ^{16}N could be single particle in nature.

Given the paucity of direct capture data for this reaction, it would certainly be useful to perform a Coulomb dissociation experiment to find the low energy capture cross-section for the reaction, especially below 0.25 MeV. In fact, recently the Coulomb dissociation method has been used to find the neutron capture cross-section to different states of ^8Li [3].

We also calculate the $^{15}\text{N}(n,\gamma)^{16}\text{N}$ reaction rate per mole as a function of temperature. For temperatures relevant for typical AGB stars and for inhomogeneous

big bang model, our calculations favor the destruction of ^{15}N by neutron capture than by proton or alpha capture.

BIBLIOGRAPHY

[1] Meissner J., Schatz H., Herndl H., Wiescher M., Beer H., and Köppeler F., Neutron capture cross section of ^{15}N at stellar energies, Phys. Rev. C **53**, 977 (1996).

[2] Nakamura T., Fukuda N., Aoi N., and Imai N., *et al.*, Neutron capture cross section of ^{14}C of astrophysical interest studied by Coulomb breakup of ^{15}C, Phys. Rev. C **79**, 035805 (2009).

[3] Izsák R., Horváth Á., Kiss Á., and Seres Z.,*et al.* Determining the ^{7} Li(n, γ) cross section via Coulomb dissociation of ^{8}Li, Phys. Rev. C **88**, 065808 (2013).

[4] Kajino T., Mathews G. J., and Fuller G. M. , in *Heavy-ion physics and astrophysical problems*, edited by S. Kubono (World Scientific, Singapore, 1989).

[5] Kawano L. H., Fowler W. A., Kavanagh R. W., Malaney R. A., Signatures of inhomogeneity in the early universe, Astrophys. J. **372**, 1 (1991).

[6] Dubovichenko S. B., Radiative n^{15}N Capture at Low Energies Russ. Phys. J., **56**, 494 (2013).

[7] Wiescher M., Görres J., Schatz H., Break-out reactions from the CNO cycles, J. Phys. G **25**, R133 (1999).

[8] Bardayan D. W., O'Malley P. D., Blackmon J. C., and Chae K. Y., *et al.* Spectroscopic study of low-lying ^{16}**N** levels, Phys. Rev. C **78**, 052801(R) (2008).

[9] Guo B. *et al.*, Spectroscopic factors for low-lying ^{16}N levels and the astrophysical ^{15}N$(n, \gamma)^{16}$N reaction rate, Phys. Rev. C **89**, 012801(R) (2014).

[10] Bohne W., Bommer J., Fuchs H., Grabisch K., Kluge H., Röschert G., Study of the (d, n) and (d, p) reactions on ^{15}N Nucl. Phys. A **196**, 41 (1972).

[11] Rauscher T., Applegate J. H., Cowan J. J., Thielemann F. -K., and Wiescher M., Production of heavy elements in inhomogeneous cosmologies, Astrophys. J. **429**, 499 (1994).

[12] Herndl H., Hofinger R., Jank J., Oberhummer H., G'orres J., Wiescher M. Thielemann F. K., and Brown B. A., Reaction rates for neutron capture reactions to C, N, and O isotopes to the neutron rich side of stability, Phys. Rev. C **60**, 064614 (1999).

[13] Huang J. T., Bertulani C. A., Guimarães V., Radiative capture of nucleons at astrophysical energies with single-particle states, Atomic Data and Nuclear Data Tables **96**, 824 (2010).

[14] Bertulani C.A., RADCAP: A potential model tool for direct capture reactions, Comput. Phys. Commun. **156**, 123 (2003).

[15] Chatterjee R., Banerjee P., Shyam R., Projectile structure effects in the Coulomb breakup of one-neutron halo nuclei, Nucl. Phys. A **675**, 477 (2000).

[16] Banerjee P., Chatterjee R., Shyam R., Coulomb dissociation of ^{9}**Li** and the rate of the ^{8}**Li**$(n, \gamma)^9$**Li**, Phys. Rev. C **78**, 035804 (2008).

[17] Shubhchintak, Neelam and Chatterjee R., Capture cross-section and rate of the ^{14}C$(n, \gamma)^{15}$C reaction from the Coulomb dissociation of ^{15}C, Pramana J. Phys. **83**, 533 (2014).

[18] Bertulani C. A., Baur G., Electromagnetic processes in relativistic heavy ion collisions, Phys. Rep. **163**, 299 (1988).

[19] Bertulani C. A., Gade A., Nuclear astrophysics with radioactive beams, Phys. Rep. **485**, 195 (2010).

[20] Tribble R. E., Bertulani C. A., La Cognata M., Mukhamedzhanov A. M., and Spitaleri C., Indirect techniques in nuclear astrophysics: a review, Rep. Prog. Phys. **77**, 106901 (2014).

[21] Baur G., Bertulani C.A., and Rebel H., Coulomb dissociation as a source of information on radiative capture processes of astrophysical interest, Nucl. Phys. A **458**, 188 (1986).

[22] Aleixo A. and C. A. Bertulani, COULOMB EXCITATION IN INTERMEDIATE-ENERGY COLLISIONS, Nucl. Phys. A **505**, 448 (1989).

[23] Timofeyuk N. K., Baye D., Descouvemont P., Kamouni R., Thompson I. J., ^{15}C - ^{15}F Charge Symmetry and the ^{14}C$(n, \gamma)^{15}$C Reaction Puzzle, Phys. Rev. Lett. **96**, 162501 (2006).

[24] Huang J. T., Bertulani C. A., Guimarães V., Radiative capture of nucleons at astrophysical energies with single-particle states, Atomic Data and Nuclear Data Tables **96**, 824 (2010).

[25] Iliadis C., *Nuclear Physics of stars*, (Wiley-VCH Verlag GmbH & Co. KGaA, Weinheim, 2007).

[26] Rolfs C. E. and Rodney W. S., *Couldrons in the Cosmos* (University of Chicago Press, Chicago, 1988).

[27] Lee D. W., Peräjärvi K. , Powell J., O'Neil, J. P., Moltz D. M., Goldberg V. Z., and Cerny J., Low-lying resonant states in ^{16}F using a ^{15}O radioactive ion beam, Phys. Rev. C **76**, 024314 (2007).

[28] Stefan I.,*et at.*, Probing nuclear forces beyond the drip-line using the mirror nuclei ^{16}N and ^{16}F, Phys. Rev. C **90**, 014307 (2014).

[29] Xu Y., Takahashi K., Goriely S., Arnould M., Ohta M. and Utsunomiya H., NACRE II: an update of the NACRE compilation of charged-particle-induced thermonuclear reaction rates for nuclei with mass number $A < 16$, Nucl. Phys. A **918**, 61 (2013).

[30] Angulo C., Arnould M., Rayet M., and Descouvemont P.,*et al.*, A compilation of charged-particle induced thermonuclear reaction rates, Nucl. Phys. A **656**, 3 (1999).
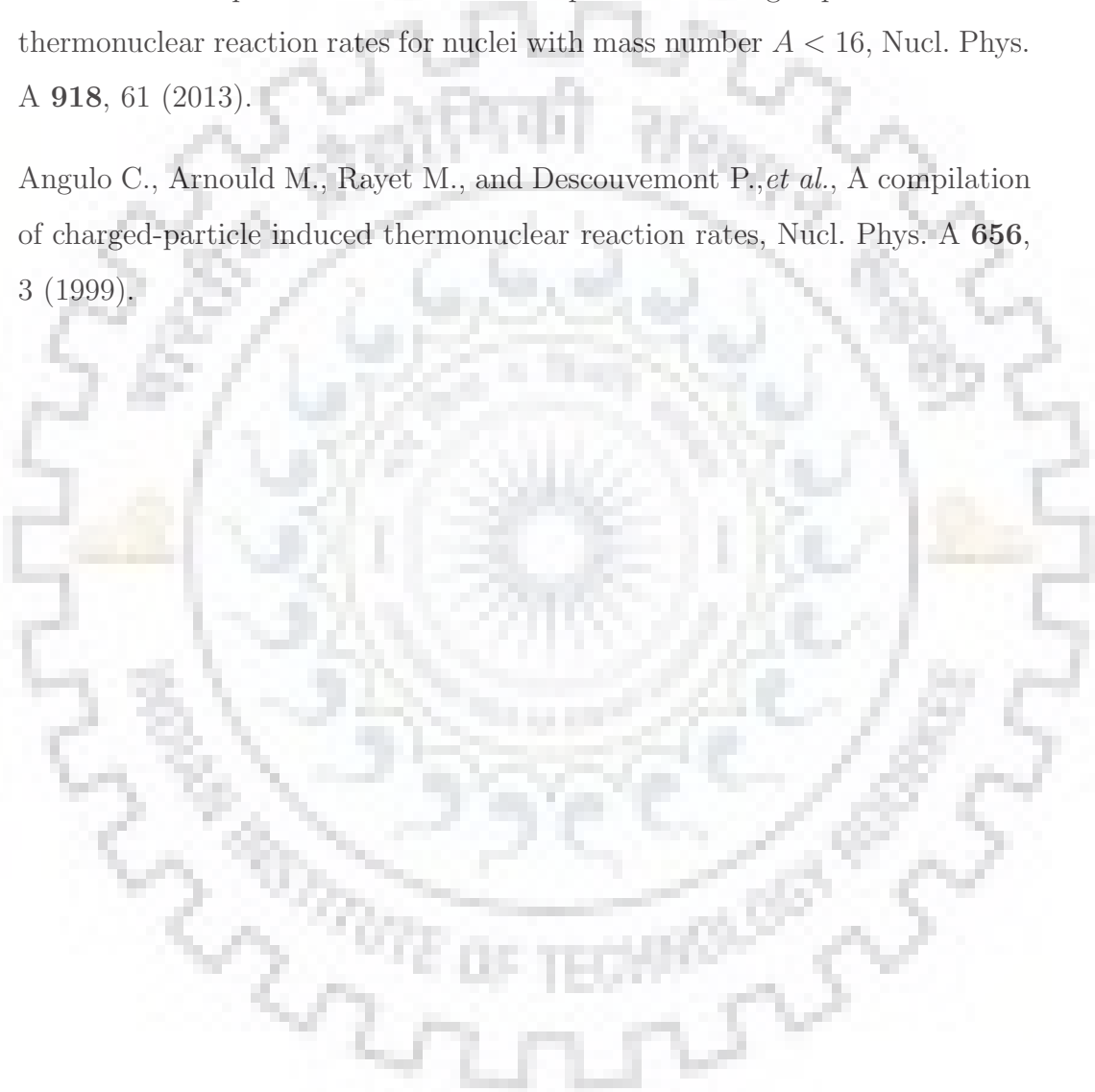
CHAPTER 5

SUMMARY AND FUTURE OUTLOOK

5.1   Summary

Break-up reactions offer many opportunities to study the structure and reactions of exotic nuclei. In this thesis we use the theoretical formalism of elastic Coulomb break-up reactions to study medium mass exotic nuclei and also applications in nuclear astrophysics.

This thesis is in two parts. In the part I of the thesis we gave an introduction and define the scope of the thesis. A discussion on the formal theory of break-up reaction makes up chapter 2 wherein we also introduce our Coulomb break-up theory under the distorted wave Born approximation. In this theory the electromagnetic interaction between the fragments and the target nucleus is included to all orders and the break-up contributions from the entire nonresonant continuum corresponding to all the multipoles and the relative orbital angular momenta between the fragments are accounted for. Because the only input to our theory is the ground-state wave func-

tion of the projectile, of any orbital angular momentum configuration, our method is free from the uncertainties associated with the multipole strength distributions of the projectile

This part also includes application of our theory, extended to incorporate projectile deformation, to a medium mass exotic nucleus ^{37}Mg. The part II of the thesis concerns application of our theory to nuclear astrophysics.

In chapter 3 we study the Coulomb break-up of the neutron rich nucleus ^{37}Mg on a Pb target at the beam energy of 244 MeV/nucleon within the framework of a finite range distorted wave Born approximation theory that is extended to include the effects of projectile deformation.

Calculations have been carried out for the total one-neutron removal cross-section (σ_{-1n}), the neutron-core relative energy spectrum, the parallel momentum distribution of the core fragment, the valence neutron angular, and energy-angular distributions. The calculated σ_{-1n} has been compared with the recently measured data to put constraints on the spin parity, and the one-neutron separation energy (S_n) of the ^{37}Mg ground state (^{37}Mg$_{gs}$). The dependence of σ_{-1n} on the deformation of this state has also been investigated. While a spin parity assignment of $7/2^-$ for the ^{37}Mg$_{gs}$ is ruled out by our study, neither of the $3/2^-$ and $1/2^+$ assignments can be clearly excluded. Using the spectroscopic factor of one for both the $3/2^-$ and $1/2^+$ configurations and ignoring the projectile deformation effects, the S_n values of 0.35 ± 0.06 MeV and 0.50 ± 0.07 MeV, respectively, are extracted for the two configurations. However, the extracted S_n is strongly dependent on the spectroscopic factor and the deformation effects of the respective configuration.

The narrow parallel momentum distribution of the core fragment and the strong forward peaking of the valence neutron angular distribution suggest a one-neutron halo configuration in either of the $2p_{3/2}$ and $2s_{1/2}$ configurations of the ^{37}Mg ground state.

In chapter 4 we study the ^{15}N$(n, \gamma)^{16}$N radiative capture cross-section and its subsequent reaction rate by an indirect method and in that process investigate the

effects of spectroscopic factors of different levels of ^{16}N to the cross-section.

The ^{15}N$(n, \gamma)^{16}$N reaction plays an important role in red giant stars and also in inhomogeneous big bang nucleosynthesis. However, there are controversies regarding spectroscopic factors of the four low-lying states of ^{16}N, which have direct bearing on the total direct capture cross section and also on the reaction rate. Direct measurements of the capture cross section at low energies are scarce and is available only at three energies below 500 keV.

The fully quantum mechanical Coulomb break-up theory under the aegis of post-form distorted wave Born approximation was used to calculate the Coulomb break-up of ^{16}N on Pb at 100 MeV/nucleon. This is then related to the photodisintegration cross-section of ^{16}N$(\gamma, n)^{15}$N and subsequently invoking the principle of detailed balance, the ^{15}N$(n, \gamma)^{16}$N capture cross-section was calculated.

The non-resonant capture cross-section is calculated with spectroscopic factors from the shell model and those extracted (including uncertainties) from two recent experiments. The data seemed to favor a more single particle nature for the low-lying states of ^{16}N. The total neutron capture rate was also calculated by summing up non-resonant and resonant (significant only at temperatures greater than 1 GK) contributions and comparison was made with other charged particle capture rates. In the typical temperature range of $0.1 - 1.2$ GK, almost all the contribution to the reaction rate comes from capture cross-sections below 0.25 MeV.

5.2 Future outlook

5.2.1 Radiative capture involving deformed nuclei

It is now known that in the production of seed nuclei in for r- process nucleosynthesis critical role is played by neutron rich nuclei especially in light and medium mass region [1]. In fact it has been suggested that depending on how the rates of ^{36}Mg$(\alpha, n)^{39}$Si compares with that of ^{36}Mg$(n, \gamma)^{37}$Mg, the r- process flow could be broken before reaching the neutron drip line. Therefore it will be interesting to calcu-

late the radiative neutron capture rates involving deformed nuclei and also compare them with (α, n) reactions. In fact using the Coulomb dissociation of ^{37}Mg on a heavy target could be used as an indirect method to calculate the ^{36}Mg$(n, \gamma)^{37}$Mg radiative capture reaction cross-section.
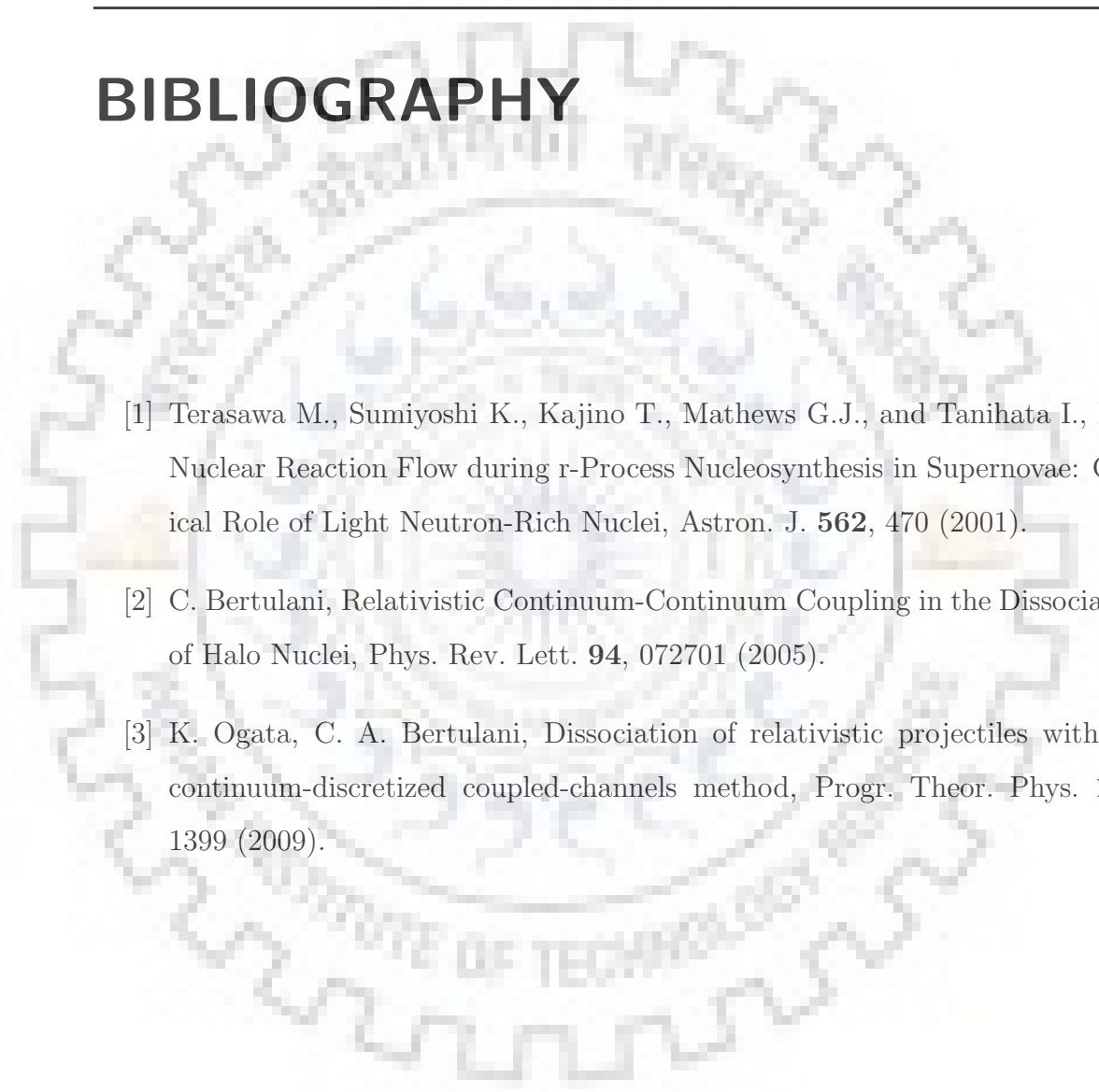
5.2.2 On the need for a relativistic break-up theory

It is worthwhile to note the *beam energy* at which many of the experiments involving exotic nuclei are performed. Many of the first generation experimental facilities (except at GSI) used to run with beam energies less than 100 MeV/nucleon. However with recent upgrades mostly to study medium mass exotic nuclei beam energies in the range of 300 - 400 MeV/nucleon are quite common.

Therefore, if one is not satisfied in simply plugging in relativistic kinematics into the non relativistic Schrödinger equation one could question the applicability of the Schrödinger equation itself for such beam energies. Some initial efforts in this direction have been proposed in Refs. [2, 3].

This calls for fully a relativistic description of the break-up process incorporating full Coulomb (and nuclear) interactions between the fragments and the target, with final state interaction between break-up fragments and target nucleus taken to all orders (three or four body final states). One has also to worry about the Lorentz invariance of the interactions involved in such a theory.

BIBLIOGRAPHY

[1] Terasawa M., Sumiyoshi K., Kajino T., Mathews G.J., and Tanihata I., New Nuclear Reaction Flow during r-Process Nucleosynthesis in Supernovae: Critical Role of Light Neutron-Rich Nuclei, Astron. J. **562**, 470 (2001).

[2] C. Bertulani, Relativistic Continuum-Continuum Coupling in the Dissociation of Halo Nuclei, Phys. Rev. Lett. **94**, 072701 (2005).

[3] K. Ogata, C. A. Bertulani, Dissociation of relativistic projectiles with the continuum-discretized coupled-channels method, Progr. Theor. Phys. **121**, 1399 (2009).

THE LOCAL MOMENTUM APPROXIMATION (LMA)

A.1   The validity conditions

With the local momentum approximation(LMA) the finite range effects are included in distorted wave Born approximation(DWBA) theory. It's use leads to the factorization of the six dimensional integral in break-up amplitudes [as in Eq. 2.24] into two 3-dimensional integral and thus analytical solution of break-up amplitude become simpler.

Consider a wavefunction $\chi(\mathbf{R})$, where $\mathbf{R} = \mathbf{r_1} + \mathbf{r}$, which satisfies the Schrödinger equation

$$\left[\nabla^2 + \frac{2\mu}{\hbar^2}(E - V(R))\right]\chi(\mathbf{R}) = 0. \tag{A.1}$$

The wavefunction $\chi(\mathbf{R})$ and the potential V(R) can be expanded using Taylor series

expansion around $\mathbf{r}$ as,

$$\chi(\mathbf{R}) = \chi(\mathbf{r}) + \mathbf{r}_1.\nabla_r\chi(\mathbf{r}) + \frac{1}{2!}(\mathbf{r}_1.\nabla_r)(\mathbf{r}_1.\nabla_r)\chi(\mathbf{r}) + ...$$
$$= e^{(\mathbf{r}_1.\nabla_r)}\chi(\mathbf{r}) \tag{A.2}$$

$$V(R) = V(r) + \mathbf{r}_1.\nabla_r V(r) + \frac{1}{2!}(\mathbf{r}_1.\nabla_r)(\mathbf{r}_1.\nabla_r)V(r) + ... \ . \tag{A.3}$$

Using Eqs. (A.2) and (A.3) in Eq.(A.1) we get

$$\left[\nabla^2 + \frac{2\mu}{\hbar^2}(E - V(r) - \mathbf{r}_1.\nabla_r V(r) + ...)\right]e^{(\mathbf{r}_1.\nabla_r)}\chi(\mathbf{r}) = 0. \tag{A.4}$$

In the local momentum approximation, the del operator in Eq. (A.2) is replaced by a momentum vector [say, $i\mathbf{K}(\mathbf{r})$] Considering only first two terms and neglecting higher terms of expansion in Eq. (A.3). Then Eq. (A.4) become equivalent to

$$\left[\nabla^2 + \frac{2\mu}{\hbar^2}(E - V(r))\{1 - \frac{\mathbf{r}_1.\nabla_r V(r)}{E - V(r)}\}\right]e^{(i\mathbf{K}(\mathbf{r}).\mathbf{r}_1)}\chi(\mathbf{r}) = 0. \tag{A.5}$$

Eq.(A.5) is further simplified, if the second term in curly bracket is very small as compared to unity, as

$$\left[\nabla^2 + \frac{2\mu}{\hbar^2}(E - V(r))\right]e^{(i\mathbf{K}(\mathbf{r}).\mathbf{r}_1)}\chi(\mathbf{r}) = 0. \tag{A.6}$$

This simplificaton is valid only if

$$r_1 << \frac{E - V(r)}{\nabla V}. \tag{A.7}$$

The magnitude of $\mathbf{K}(\mathbf{r})$ is taken to be

$$K(r) = \sqrt{\frac{2\mu}{\hbar^2}[E - V(r)]}. \tag{A.8}$$

Differentiating (A.8) w.r.t. r,

$$\frac{dK(r)}{dr} = \sqrt{\frac{2\mu}{\hbar^2}} \frac{(-\frac{dV(r)}{dr})}{\sqrt{[E - V(r)]}} \tag{A.9}$$

$$\eta(r) = \frac{[E - V(r)]}{-\frac{V(r)}{r}} = \frac{\frac{1}{2}K(r)}{\left|\frac{dK(r)}{dr}\right|}. \tag{A.10}$$

It is to note that, an upper bound exists on the value of r_1 due to the presence of potential $V(r_1)$ and this upper bound is given by range of interaction $V(r_1)$. For a short range potential, the maximum value of r_1 Therefore, a sufficient condition for the validity of local momentum approximation is,

$$r_a << \eta(r). \tag{A.11}$$

For all practical purposes, the value of $\mathbf{K}$ is calculated at a fixed distance, r beyond which $\mathbf{K}(\mathbf{r})$ is almost constant. In addition, the contribution of the nuclear interior for the peripheral collisions is almost negligible. We calculated local momentum at $r = 10$ fm, having direction which is same as that of the asymptotic momentum of the particle in question. We will show the choice of this direction is valid because there is a weak dependence of the cross-section on this direction of the local momentum. The vector $\mathbf{K}$ is evaluated at some fixed distance r; as is shown later on $K(r)$ is almost constant after a certain value of r. Moreover in peripheral collisions the nuclear interior contributes almost negligibly.

As an example to check the validity of the approximation, in Fig. A.1 we show the variation of $\eta(r)$ (upper half) and $K(r)$ (the magnitude of the local momentum) (lower half) as a function of r, for the Coulomb break-up reaction $^{16}\text{N} + \text{Pb} \rightarrow ^{15}\text{N} + n + \text{Pb}$ at the beam energy of 100 MeV/nucleon. At $r = 10$ fm, $\eta(r) >> r_a (= 3.11$ fm), the projectile root mean square radius. $K(r)$ is also seen to be constant
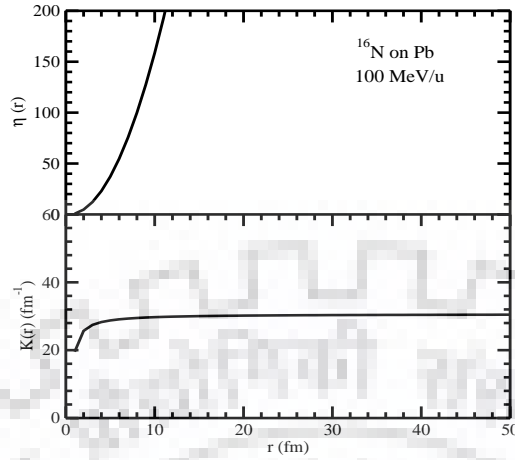
Figure A.1: Variation of $\eta(r)$ (upper half) and $K(r)$ (lower half) with r for the Coulomb break-up of ^{16}N on Pb in its ground state.

for $r > 8$ fm. These conditions have been checked to be true for the other three excited states of ^{16}N.

Table A.1: Total one-neutron removal cross-section (σ_{-n}) in the Coulomb break-up of ^{16}N on Pb at 100 MeV/nucleon, calculated at three different directions of local momentum for all the four low-lying states of ^{16}N.

J^π	Energy (MeV)	σ_{-n} (mb)		
		d_1	d_2	d_3
2^-	0	1.95	2.04	2.16
0^-	0.120	35.55	35.00	34.32
3^-	0.298	3.04	3.17	3.36
1^-	0.397	49.44	48.68	47.73

In order to check the dependence of our results on the direction of $\mathbf{K}$, we calculate the total Coulomb break-up cross-section at three different directions of the local momentum – (d_1): parallel to the beam direction (zero angles), (d_2): parallel to the direction corresponding to the half of the angles of $\mathbf{q}_b$ and (d_3): parallel to $\mathbf{q}_b$.

Table A.1, shows the variation of total cross-section in the Coulomb break-up of ^{16}N on Pb at 100 MeV/nucleon, calculated at three different directions of local momentum as mentioned above, for all the four low-lying states of ^{16}N. It is clear that the change in total cross-section is less than 10 % for ground and second excited

states and it is even less than 4 % for the first and third excited states, as one moves from direction (d_1) to (d_3).

APPENDIX B

THREE-BODY PHASE SPACE FACTOR

We work in the laboratory system and use the following notations: t = target, a = projectile, b = core, n = valence particle, neutron. Let us find out the phase space $\rho(E_b, \Omega_b, \Omega_n)$, corresponding to the differential cross-section $\frac{d\sigma}{dE_b d\Omega_b d\Omega_n}$, which is the purely statistical spectrum of particle b at angle Ω_b under the condition that particle n is detected at Ω_n. We start from [1]

$$d\sigma = h^{-6}\delta(E_{tot} - E)d\mathbf{p}_b d\mathbf{p}_n \qquad (B.1)$$

---

[1]H. Fuchs, On cross section transformations in reactions with three outgoing fragments, Nucl. Instrum. Methods **200**, 361 (1982).

which is the cross-section in phase space in which the total energy in the final state (E_{tot}) is fixed at the value E. This total energy is given by

$$E_{tot} = E_a + Q \tag{B.2}$$

$$= E_t + E_b + E_n \tag{B.3}$$

$$= \frac{[(\mathbf{p}_{tot} - \mathbf{p}_b) - \mathbf{p}_n]^2}{2m_t} + \frac{\mathbf{p}_b^2}{2m_b} + \frac{\mathbf{p}_n^2}{2m_n} \tag{B.4}$$

$$= \frac{[(\mathbf{p}_{tot} - \mathbf{p}_b)^2 + p_n^2 - 2\mathbf{p}_n \cdot (\mathbf{p}_{tot} - \mathbf{p}_b)]}{2m_t} + \frac{p_b^2}{2m_b} + \frac{p_n^2}{2m_n}, \tag{B.5}$$

where E_a is the projectile energy and Q is the Q-value of the reaction (< 0). $\mathbf{p}_i$ and m_i are the momentum and mass of particle i, respectively and $\mathbf{p}_{tot}$ is the total momentum of the projectile in the incident channel, which by momentum conservation, is given by

$$\mathbf{p}_{tot} = \mathbf{p}_t + \mathbf{p}_b + \mathbf{p}_n. \tag{B.6}$$

Using $d\mathbf{p} = p^2.dp.d\Omega = m.p.dE.d\Omega$ and Eq. (B.1), we have

$$\frac{d\sigma}{dE_b d\Omega_b dE_n d\Omega_n} = \frac{d\sigma}{d\mathbf{p}_b d\mathbf{p}_n} m_b p_b m_n p_n = h^{-6}\delta(E_{tot} - E)m_b p_b m_n p_n. \tag{B.7}$$

Therefore,

$$\rho(E_b, \Omega_b, \Omega_n) = \frac{d\sigma}{dE_b d\Omega_b d\Omega_n} = \int \frac{d\sigma}{dE_b d\Omega_b dE_n d\Omega_n} dE_n$$

$$= h^{-6}\int m_b p_b m_n p_n \delta(E_{tot} - E)dE_n$$

$$= h^{-6}\int m_b p_b m_n p_n \delta(E_{tot} - E)\frac{dE_{tot}}{\partial E_{tot}/\partial E_n}$$

$$= h^{-6}m_b m_n \left[\frac{p_b p_n}{\partial E_{tot}/\partial E_n}\right]_{E_{tot}=E}. \tag{B.8}$$

Furthermore, using Eq. (B.5) we have

$$\frac{\partial E_{tot}}{\partial E_n} = \frac{\partial E_{tot}}{\partial p_n}\frac{dp_n}{dE_n} = \left[\frac{p_n}{m_n} + \frac{p_n}{m_t} - \frac{\hat{\mathbf{p}}_n \cdot (\mathbf{p}_{tot} - \mathbf{p}_b)}{m_t}\right]\frac{m_n}{p_n}$$

$$= \left[1 + \frac{m_n}{m_t} - m_n\frac{\mathbf{p}_n \cdot (\mathbf{p}_{tot} - \mathbf{p}_b)}{m_t p_n^2}\right]$$

$$= \frac{1}{m_t}\left[m_t + m_n - m_n\frac{\mathbf{p}_n \cdot (\mathbf{p}_{tot} - \mathbf{p}_b)}{p_n^2}\right]. \tag{B.9}$$

Thus,

$$\rho(E_b, \Omega_b, \Omega_n) = \frac{h^{-6}m_b m_n m_t p_b p_n}{\left[m_t + m_n - m_n\frac{\mathbf{p}_n \cdot (\mathbf{p}_{tot} - \mathbf{p}_b)}{p_n^2}\right]}. \tag{B.10}$$